

IMMUNOLOGY

High-salt diet mediates interplay between NK cells and gut microbiota to induce potent tumor immunity

Zaigham Abbas Rizvi^{1,2}, Rajdeep Dalal^{1,2}, Srikanth Sadhu^{1,2}, Yashwant Kumar³, Shakti Kumar², Sonu Kumar Gupta³, Manas Ranjan Tripathy^{1,2}, Deepak Kumar Rathore², Amit Awasthi^{1,2*}

High-salt diet (HSD) modulates effector and regulatory T cell functions and promotes tissue inflammation in autoimmune diseases. However, effects of HSD and its association with gut microbiota in tumor immunity remain undefined. Here, we report that HSD induces natural killer (NK) cell-mediated tumor immunity by inhibiting PD-1 expression while enhancing IFN γ and serum hippurate. Salt enhanced tumor immunity when combined with a suboptimal dose of anti-PD1 antibody. While HSD-induced tumor immunity was blunted upon gut microbiota depletion, fecal microbiota transplantation (FMT) from HSD mice restored the tumor immunity associated with NK cell functions. HSD increased the abundance of *Bifidobacterium* and caused increased gut permeability leading to intratumor localization of *Bifidobacterium*, which enhanced NK cell functions and tumor regression. Intratumoral injections of *Bifidobacterium* activated NK cells, which inhibited tumor growth. These results indicate that HSD modulates gut microbiome that induces NK cell-dependent tumor immunity with a potential translational perspective.

INTRODUCTION

Dietary components influence human health by regulating immune homeostasis and gut microbiota composition (1–4). Salt when taken in a higher amount [4% NaCl: high-salt diet (HSD)] has been identified as a potent immunomodulator associated with a strong inflammatory response (5–7). Recent studies identified that HSD exacerbates tissue inflammation in ulcerative colitis and autoimmune encephalomyelitis and increases the risk of cardiovascular diseases associated with enhanced T helper 17 (T_H17) cell development and functions (5, 8, 9). Other studies reported that HSD polarizes macrophages to M1-like phenotype and its association with elevated interferon- γ (IFN γ) response (6, 7, 10). A longitudinal study on healthy human participants found a strong correlation between HSD and monocyte frequency (6). On the basis of these observations, HSD could act as an inflammatory trigger that may overcome immunosuppressive conditions associated with tumor microenvironment such as the expression of checkpoint inhibitors and down-regulation of major histocompatibility complex I (MHC-I) molecules. Recent studies have shown that HSD can inhibit tumor growth, which may be dependent on myeloid-derived suppressor cells (MDSCs) (11, 12).

Down-regulation of MHC-I is a strong activation signal for NK cell activation and mediates direct killing of tumor cells (13). Activation of NK cells is in turn controlled by a wide array of activation signals such as CD107a, natural cytotoxic trigger receptor 1 (NCR1), CD226, and inhibitory signals such as CD96, programmed cell death protein (PD) 1, T cell immunoglobulin and ITIM domain (TIGIT), T-cell immunoglobulin domain and mucin domain (Tim) 3,

and cytotoxic T-lymphocyte associated protein (CTLA) 4 molecules (14–17). Furthermore, the tumor microenvironment is often characterized by ionic imbalance as decreased sodium level (hyponatremia) has been linked to human cancers (18, 19). Altered Na⁺/H⁺ concentration across the gut epithelial barrier is linked with changes in gut permeability and dysbiosis, and previous reports have suggested that HSD induces changes in the gut microbiota composition and metabolic alterations in rodents (20). These shreds of evidence suggested that tumor immunity by HSD may involve factors from serum and gut microbiota and may influence other components of the immune system essential for antitumor functions.

In the current study, we report that tumor-bearing mice fed with HSD potently suppressed tumor growth by up-regulation of NK cell frequency and activation markers and down-regulation of NK cell inhibitory signals (especially PD1 molecule). NK cell depletion truncated the tumor immunity of HSD, which was found to be mediated by NK-dependent interferon- γ (IFN γ) response. We further establish that HSD, in mice, leads to marked up-regulation of serum hippurate, a microbial benzoate metabolism product that is also described as one of the metabolic markers of PD-1 immunotherapy in responding patients (21). In line with this, we report that the combination of a suboptimal dose of anti-PD1 antibody together with a low-salt diet provides a significant tumor regression. Antibiotic-induced gut microbiota depletion (AIMD) abrogated the HSD-mediated tumor inhibition and antitumor NK cell functions, indicating the involvement of gut microbiota. HSD-fed mice showed an increased abundance of *Bifidobacterium* in their stool, which upon transfer to AIMD mice, suppressed tumor progression associated with increased intratumor NK cell frequency and elevated serum hippurate levels. Last, we demonstrate that mice fed with HSD show an increased gut permeability resulted in intratumoral localization of *Bifidobacterium* leading to NK cell activation. While intratumoral administration of *Bifidobacterium* alone resulted in tumor regression, NK cell depletion blunted *Bifidobacterium*-mediated protection. Furthermore, increased hippurate levels were found in *Bifidobacterium* administered mice suggesting that hippurate might be a potential biomarker of HSD-mediated tumor immunity. Together,

Copyright © 2021
The Authors, some
rights reserved;
exclusive licensee
American Association
for the Advancement
of Science. No claim to
original U.S. Government
Works. Distributed
under a Creative
Commons Attribution
License 4.0 (CC BY).

¹Immunobiology Lab, Translational Health Science and Technology Institute, NCR-Biotech Science Cluster, 3rd Milestone, Faridabad-Gurgaon Expressway, Faridabad, Haryana 121001, India. ²Infection and Immunology, Translational Health Science and Technology Institute, NCR-Biotech Science Cluster, 3rd Milestone, Faridabad-Gurgaon Expressway, Faridabad, Haryana 121001, India. ³Noncommunicable Disease Center, Translational Health Science and Technology Institute, NCR-Biotech Science Cluster, 3rd Milestone, Faridabad-Gurgaon Expressway, Faridabad, Haryana 121001, India.

*Corresponding author. Email: aawasthi@thsti.res.in

we provide the mechanistic insight into the factors involved in HSD-mediated tumor immunity and show that *Bifidobacterium* and NK cross-talk is essential in mounting tumor immunity. Our preclinical data strongly suggest the therapeutic potential of HSD and points to its potential translational application.

RESULTS

HSD imparts robust tumor immunity in syngeneic mouse tumor models

As a proof of concept, we studied the effect of salt on B16F10 skin melanoma (abbreviated B16) in mice. For this, mice implanted with B16 cells subcutaneously were simultaneously fed with three different doses of dietary salt viz. normal diet (ND) containing naturally occurring 0.9% NaCl above ND, low-salt diet (LSD) containing 1.0% NaCl above ND, and HSD consisting of 4% NaCl above ND as shown in Fig. 1A. We found that as compared to ND, mice fed with HSD significantly reduced tumor progression measured by tumor volume and mass associated with an overall increased percent survival (Fig. 1, B and C). No significant tumor regression and percent survival were noticed in the mice fed with LSD (Fig. 1, B and C). We did not observe any significant changes in food and water intake in mice of tumor (T), T + LSD, and T + HSD groups (fig. S1A), indicating that the salt tumor immunity induced in HSD is not through calorie restrictions. Since low sodium (Na^+) serum levels and ionic imbalances have been reported in patients with certain cancers (19), we hypothesized that HSD intake may restore serum Na^+ levels and mitigate the effects of hyponatremia. In line with this, we found around 35% reduction in the serum Na^+ level at end point in the mice with melanoma as compared to healthy (H) control, which was restored to normal levels in mice fed with HSD (fig. S1B).

There were no changes observed in serum potassium (K^+), serum glutamic pyruvic transaminase, serum glutamic oxaloacetic transaminase, alkaline phosphatase, creatinine, urea, and uric acid levels in either T or T + HSD group (fig. S1B and S1C). Since increased salt uptake is often associated with an increased risk of cardiovascular complications and osmolarity-induced histological changes in healthy individuals, we evaluated the risk of physiological and organ-specific damages associated with HSD-fed tumor-bearing mice. Unexpectedly, our data suggest that HSD is well tolerated without any toxicological effects on major organs such as the brain, colon, heart, kidneys, liver, lungs, and spleen with no gross histological changes and no obvious signs of arrhythmia (evaluated through electrocardiogram) between H and T + HSD groups (fig. S1, D and E). It was previously reported that dietary intake of HSD could attenuate metastasis through hyperosmotic stress via p53 (22). On contrary, we found that mannitol, when used at equi-iso-osmolar to 4.0% NaCl, failed to regress B16 melanoma and improve survival (fig. S1, F and G). Next, we investigated the protective efficacy of HSD on tumors of different origins and found that HSD-fed mice imparts robust tumor immunity against B16 lung metastasis that showed ~35% decrease in lung foci count; Lewis lung carcinoma (LLC), giving twofold inhibition of tumor growth and mass; LLC lung metastasis showing around 1.75-fold decrease in lung foci count; HSD-treated mice after surgical removal of B16 melanoma imparted around threefold reduction in tumor growth and mass; and reduced tumor progression in mice given pretreatment of HSD for 15 days and then kept on ND after B16 injections [HSD pretreatment (pHSD)], with overall improved percent survival rate across all tumor models

(Fig. 1, D to M, respectively). By using 4T1 (breast cancer cell line) luciferase cell line to study lung metastasis, it was found that HSD limits seeding of 4T1 not only in lungs but also in other organs with around sixfold reduction in total flux emission (Fig. 1N). Our histological data revealed that HSD-induced regression in B16 melanoma was characterized by reduced “pus” zones, tumor cell proliferation (Ki67 expression), and melanin pigmentation in HSD group (Fig. 1O). The control Ki67 samples without anti-Ki67 antibody showed no immunohistochemistry staining (fig. S1H). Together, these data demonstrate that HSD imparts robust tumor immunity without noticeable side effects on normal physiology.

NK cell-driven $\text{IFN}\gamma$ is essential for HSD-mediated tumor immunity

To understand the changes in the immunological response of ND and LSD versus HSD-fed melanoma-bearing C57BL/6 mice, we carried out extensive immune cell profiling of tumor-infiltrating immune cells, draining lymph nodes, and splenocytes. Our data identified ~50% up-regulation of NK cell frequency and its activation marker, CD107a, along with inhibition of PD1 expression in mice fed with HSD, while no significant changes were observed in mice fed with either LSD or ND (fig. S2, A and B). Moreover, mice fed with HSD, as compared to ND or LSD, showed less prominent changes in the frequencies of other major immune cell populations viz. CD4^+ and CD8^+ T cells, $\gamma\delta$ T cells, macrophages, and MDSCs of tumor-infiltrating immune cells (Fig. 2A and fig. S2, C and D). In addition, the expression of other inhibitory markers, Tim3 and TIGIT, remain unchanged, though significant down-regulation of CTLA4 was observed on NK cells (fig. S2E). Expression of $\text{IFN}\gamma$ in NK cells was found to be significantly up-regulated, while tumor necrosis factor- α (TNF α) and interleukin-17A (IL-17A) levels remained the same in the melanoma-bearing mice fed with HSD as compared to ND (fig. S2F). Next, to validate that HSD-mediated tumor immunity is independent of adaptive immunity (B cell, CD4, and CD8 cells), we implanted B16 melanoma cells in recombination activating gene 1 knockout ($\text{RAG1}^{-/-}$) mice, as these mice lack mature T and B cells without affecting the populations of innate cells including NK cells.

As compared to ND, B16-bearing $\text{RAG1}^{-/-}$ mice fed with HSD showed ~4-fold reduction in tumor volume and ~7-fold reduction in tumor mass associated with improved survival (Fig. 2, B and C), indicating that HSD-mediated tumor immunity is independent of mature T and B cells and potentially rely upon innate immune cells. Further, flow cytometry analysis reveals that, as compared to ND, B16-bearing HSD-fed $\text{RAG1}^{-/-}$ mice show a higher frequency of NK cells in tumor-infiltrating immune cells, which was accompanied by increased CD107a expression and lowered PD1 expression on NK cells (Fig. 2, D and E). Consistently, tumor-infiltrating immune cells of B16-bearing HSD-fed $\text{RAG1}^{-/-}$ mice showed a significant up-regulation in $\text{IFN}\gamma$ and a marginal increase in TNF α levels in NK cells (Fig. 2F). In addition, the mRNA expression of PDL1 in melanoma cells was significantly decreased in B16-bearing mice kept on HSD as compared to mice kept on ND (fig. S2G). Moreover, mRNA expression of effector molecules of NK cells from tumor-infiltrating immune cells from B16-bearing HSD-fed $\text{RAG1}^{-/-}$ mice, as compared to B16-bearing ND-fed $\text{RAG1}^{-/-}$ mice, showed a robust increase in cytokines ($\text{IFN}\gamma$ and TNF α), cytotoxic factors (perforin and granzyme B), and receptors (CD226 and NCR1) (Fig. 2G). To further ascertain the role of NK cells in tumor immunity induced by

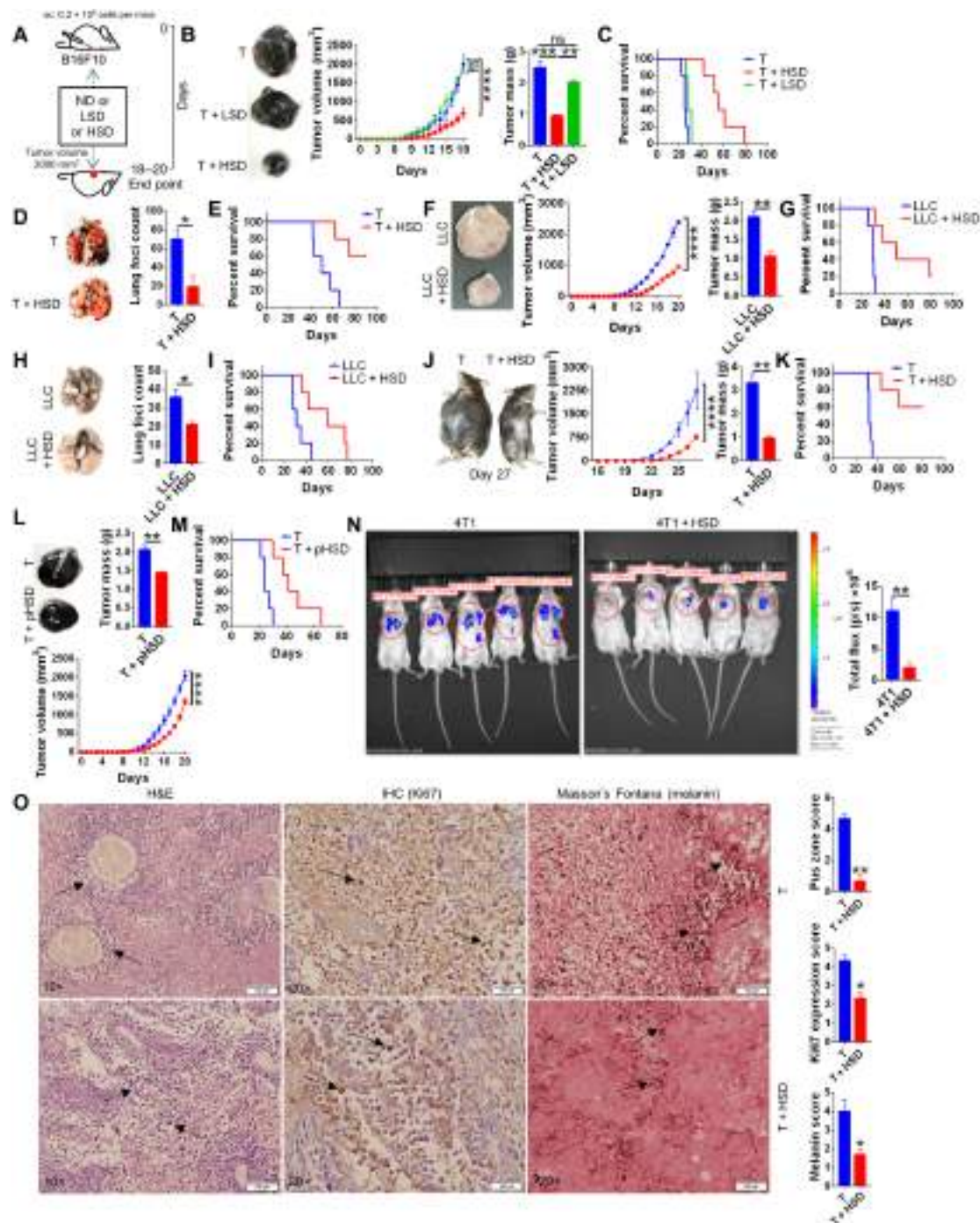


Fig. 1. HSD provides potent immunity against murine syngenic tumor. Syngenic mouse tumor models by using subcutaneous (melanoma) or intravenous (metastasis) injections of cell lines was used to study the effect of normal salt diet (T + 0.9% NaCl), low-salt diet [T + LSD (1% NaCl above ND)], or high-salt diet [T + HSD (4% NaCl above ND)] until tumor volume reached 2000 mm³ or until animal mortality for survival curve. At the end point (when tumor volume reached ~2000 mm³), the animals were euthanized; their tumor was excised, cleaned, and imaged; and their tumor mass was recorded. For metastasis model, animals were euthanized 20 days after intravenous injections, and their lung was excised to count the number of lung foci. (A) Schematic representation of the method for (B) progression of B16 skin melanoma with different doses of salt diet and (C) survival curve of B16 melanoma animals. ns, not significant; sc, subcutaneous. B16 lung metastasis model (D) showing foci in lungs and (E) survival curve. (F and G) Carcinoma and (H and I) lung metastasis with their (G and I) survival curve, respectively, by LLC cells and (J) surgical model in which tumor from mice was surgically removed at 1000 mm³, and then the animals were put either on HSD or ND and its (K) survival curve. (L) Pretreatment model in which one group of animal was pretreated for 15 days with HSD, and then B16 melanoma was allowed to grow with ND and its (M) survival curve. (N) Lung metastasis of 4T1 luciferase cells on day 16 by in vivo imaging of luminescence. (O) Histological images of B16 melanoma on day 15: hematoxylin and eosin (H&E) stain at 10× (left), immunohistochemistry (IHC) for Ki67 at 20× (middle), and Masson's Fontana stain at 20× (right). **P* < 0.05, ***P* < 0.01, ****P* < 0.001, and *****P* < 0.0001 (Student's *t* test or one-way ANOVA). Photo credit: Z. Abbas Rizvi, Translational Health Science and Technology Institute.

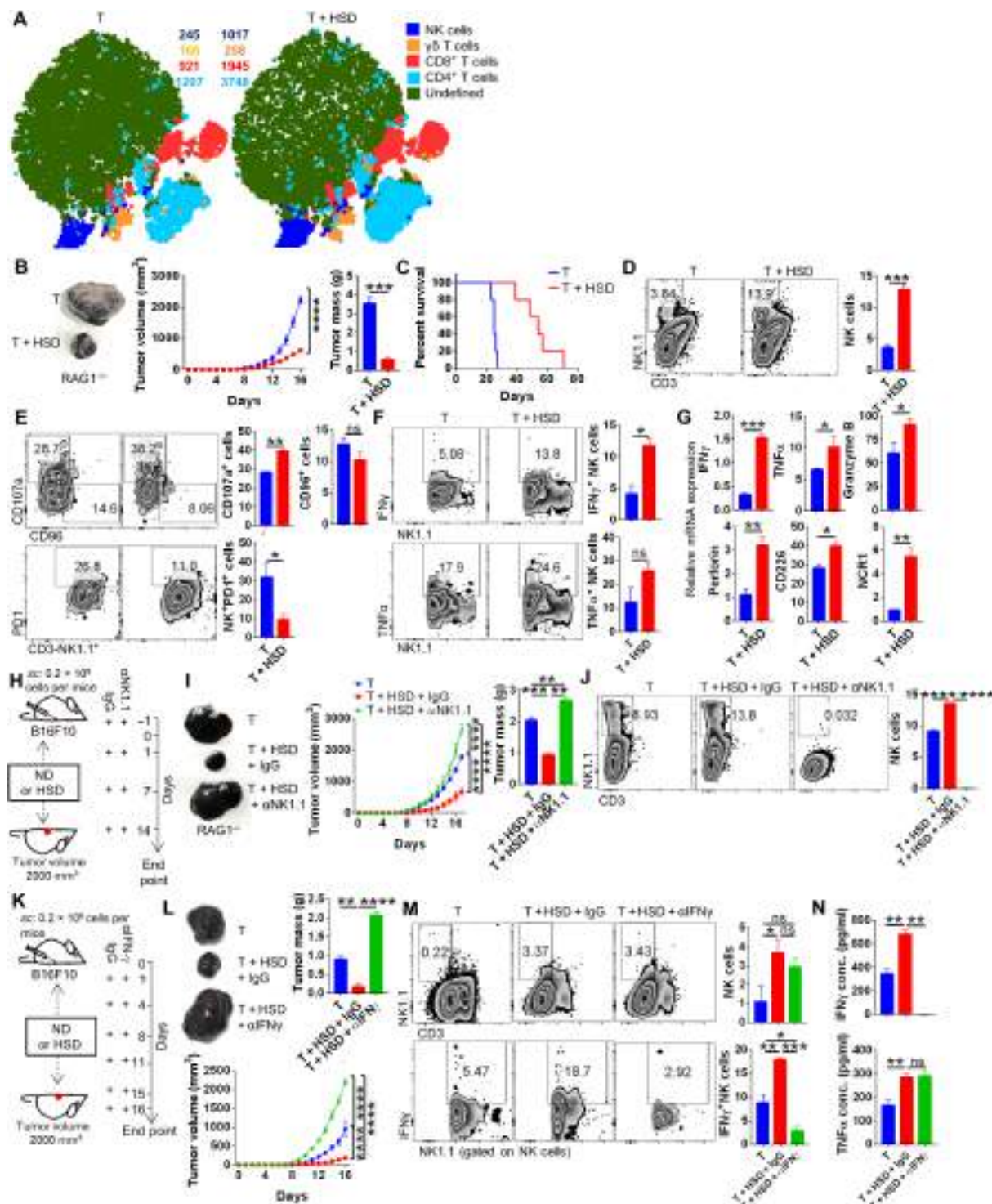


Fig. 2. HSD tumor immunity is mediated by elevated NK cell frequency and activation. Tumor-infiltrating immune cells isolated from B16 melanoma were profiled for immune cell population through flow cytometry after excising the tumor at the end point. The results from immunophenotyping was then analyzed by using graph pad and was plotted as bar graphs representing mean % positive cells \pm SEM along with representative FACS zebra plot and (A) representative t-distributed stochastic neighbor embedding (tSNE) plot depicting clusters and counts of NK, $\gamma\delta$ T, CD4, and CD8 cells. (B) B16 melanoma progression in RAG1^{-/-} mice and its (C) survival cure. (D to F) Immunophenotyping for NK cells; expression of CD107a, CD96, and PD1 molecule on NK cells; and expression of IFN γ and TNF α by NK cells. (G) Relative mRNA expression of NK cell-associated genes from tumor-infiltrating immune cells samples. (H) Schematic representation for (I) progression of B16 melanoma in the presence of HSD with or without NK cell depletion and (J) its profiling for NK cells. (K) Schematic representation for the effect of neutralization of IFN γ on (L) B16 melanoma progression and (M) changes in NK cells and IFN γ expressed by NK cells. (N) Levels of serum cytokines evaluated through ELISA. * $P < 0.05$, ** $P < 0.01$, *** $P < 0.001$, and **** $P < 0.0001$ (Student's *t* test or one-way ANOVA).

HSD, we depleted NK cells using anti-mouse NK1.1 antibody in HSD-fed B16-bearing RAG1^{-/-} mice (Fig. 2H). The depletion of NK cells blunted the protective effect of HSD on B16 growth in RAG1^{-/-} mice as measured by tumor volume and mass (Fig. 2I). Anti-NK1.1 antibody efficiently depleted NK cell population (Fig. 2J). Furthermore, since IFN γ secreted from NK cells plays an important role in tumor immunity (23) and was found to be produced by NK cells in HSD-fed mice, we next investigated whether NK cell-driven IFN γ is critical in tumor immunity induced by HSD. Our data show that HSD suppressed B16 tumor growth in mice and is associated with a higher frequency of NK cells and NK cell-driven IFN γ production from tumor-infiltrating immune cells, while IFN γ neutralization abrogated the protective effect of HSD on tumor growth (Fig. 2, K and L) with effective neutralization of serum IFN γ but not TNF α (Fig. 2, M and N). Further, the mRNA expression of cytotoxic markers on sorted NK cell population from tumor-infiltrating immune cells showed significant up-regulation in the presence of HSD (fig. S2H). Together, these data demonstrated that HSD-induced tumor immunity is mediated by NK cell and IFN γ production.

Salt induces metabolomics changes in serum with elevated serum hippurate levels

Anti-PD1 antibody-mediated therapy for various tumors has shown great success in patients with cancer and has been recently found to be associated with the up-regulation of certain metabolites in responder (R) groups as compared to nonresponder (NR) groups (21, 24). On the similar line, we set out to understand what metabolomic changes occur in the serum of tumor-bearing mice fed with HSD. To understand this, we compared metabolomics changes associated with H, T, and T + HSD groups in mice. Our liquid chromatography–tandem mass spectrometry (LC-MS/MS) data identified that 87 of 157 total metabolites were significantly modulated (Fig. 3, A and B). The principal components analysis (PCA) plot of H, T, and T + HSD showed a distinct distribution pattern of identified metabolites, indicating that the three groups have unique metabolomics profiles (Fig. 3C). There were changes in 87 modulated metabolites, and the heatmap indicated that HSD metabolomics profile was similar to H group (fig. S3A). Our metabolomics results indicate prominent changes in hippurate, 5-hydroxyindole acetic acid, cholic acid, α -ketoglutarate, L-glutathione oxidized, urocanate, etc. in B16-bearing mice fed with HSD (Fig. 3, D and E, and fig. S3B), which showed good correlation with each other (Fig. 3F and fig. S3C). Further analysis revealed that pathways related to amino acid metabolism, mevalonate-aspartate pathway, and Warburg effect were perturbed (fig. S3D). We compared serum metabolites profile of T + HSD group with previously published reports on HSD serum metabolites, metabolic markers of published cancer therapeutics. In addition, a recent study by Honjo group had identified serum metabolites of patients that responded well to anti-PD1 cancer immunotherapy (21). To investigate a correlation between the above mentioned groups serum metabolite perturbed by HSD and serum profile of anti-PD1 therapy of the R group, we generated an interactive Venn diagram by literature survey of previously published reports. Of the 87 significantly modulated metabolites in our study, 30 metabolites were found to be common between our study and previously reported HSD serum metabolites profile, 18 metabolites were found to be common in our study and previously published literature on markers for cancer therapeutics, 7 metabolites were found to be common between our study and recently published

study of responders of anti-PD1 cancer-therapy in human with the R metabolite profile, and 1 metabolite, hippurate, was uniquely common in all the groups as indicated (Fig. 3G). Taken together, these results indicated changes in serum metabolites associated with T + HSD in which hippurate was found to be increased by HSD.

Salt enhanced anti-PD1 therapy and tumor regression

Since hippurate had already been identified as potent biomarker of R group of anti-PD1 therapy from the clinical patients, we hypothesized that HSD intake-induced elevated serum hippurate levels might be helpful in anti-PD1 therapy. To test our hypothesis, we subjected B16 melanoma-bearing mice to suboptimal (so) dose of anti-PD1 in combination with LSD, which have no protective effect on tumor growth. We found strong suppression (approximately 10-fold) of B16 melanoma when LSD was combined with anti-PD1 (so) that was associated with improved survival rate (Fig. 4, A to C). This suppression was accompanied with an inhibition of surface PD1 expression on NK cells in tumor-infiltrating immune cells, while no changes in LSD alone or anti-PD1 (so) alone group were observed (Fig. 4D). Furthermore, there was no significant changes in NK cell expression in combinatorial group, suggesting that LSD may act as an adjuvant whereby even slight increase in extracellular Na⁺ ion may enhance the efficacy of anti-PD1 immunotherapy (fig. S3E). Together, these data demonstrate that salt could act as an adjuvant to promote anti-PD1 immunotherapy for tumor regression.

Gut microbiota is essential for HSD-mediated tumor immunity

As indicated earlier, pHSD for 15 days was capable of a significant reduction in tumor progression. Immunophenotyping data of pHSD group showed elevated NK cell frequency in circulation and tumor-infiltrating immune cells as compared to the untreated group (fig. S4, A and B, respectively). Further, there was an up-regulation of CD107a expression and a down-regulation of CD96, PD1, and TIGIT expression on NK cells, suggesting that HSD imparts memory through factors that may be responsible for NK cell enrichment (Fig. S4B). Modulation in the gut microbiome is associated with tumor progression especially in patients receiving anti-PD1 therapy (25–29). Since HSD has been shown to modulate the gut microbiome in autoimmune settings (5, 30), we investigated the role of gut microbiota in HSD-mediated tumor immunity. To do this, we generated mice in which their microbiome is depleted using antibiotics and hence referred as antibiotic-induced microbiome-depleted (AIMD) mice. Using AIMD mice, the effect of HSD on the progression of B16 melanoma was studied (Fig. 5A). Our data show that mice fed with HSD suppressed the tumor growth in microbiota competent wild type (WT) but not in AMID mice as measured by tumor volume and mass (Fig. 5B). We further studied the survival of B16-bearing WT and AMID mice and found that B16-bearing HSD-fed WT mice survived better than B16-bearing HSD-fed AMID mice (Fig. 5C). Further, flow cytometry analysis of tumor-infiltrating immune cells revealed an increased frequency of NK cells in HSD-fed WT mice; however, this pattern was abrogated in HSD-fed AMID mice [Fig. 5, D (top) and E]. Moreover, activation (CD107a) and inhibitory (CD96) markers of NK cells were found to be up- and down-regulated respectively in HSD-fed WT but not in HSD-fed AMID mice (Fig. 5D lower panel and 5E). The mRNA expression of NK cell-associated genes in AIMD mice was found to be down regulated or showed little or no change in HSD fed mice as

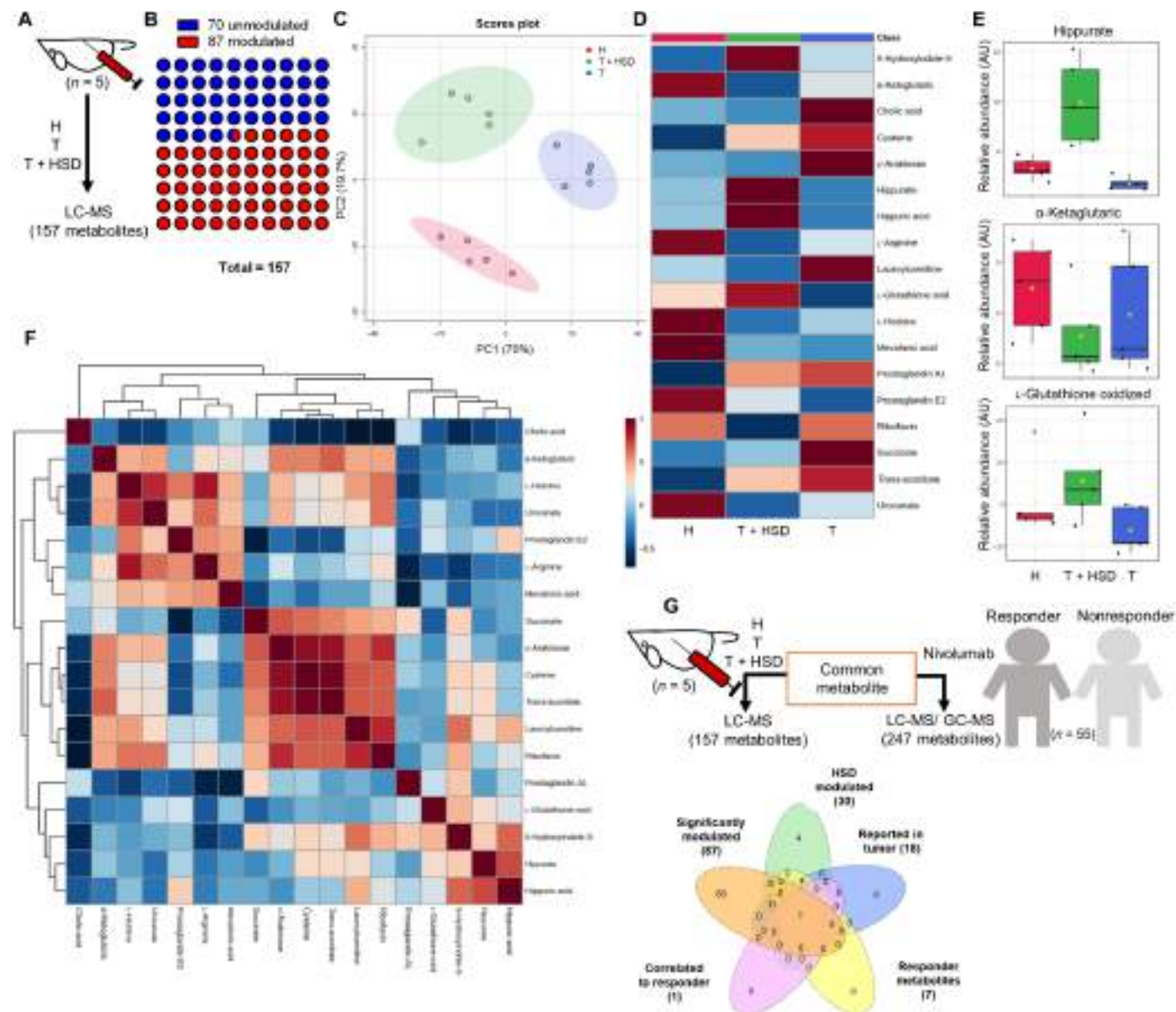


Fig. 3. Serum metabolite profiling of HSD-fed B16 melanoma-bearing mice. Serum of the salt-fed mice were profiled through LC-MS to understand the metabolomics changes associated with HSD fed B16 melanoma-bearing mice. (A) Schematic representation for the methodology and number of identified metabolites. (B) Number of significantly modified metabolites identified through ANOVA. (C) PCA distribution of the metabolomics profile from different groups. (D) Average heatmap for top 17 metabolites. (E) Normalized abundance levels of three metabolites was plotted. AU, arbitrary unit. (F) Correlation of identified metabolites with each other and (G) with the metabolomics profile of responder patients for anti-PD1 therapy was overlaid to identify common metabolite.

compared to the AIMD mice fed with ND (Fig. 5F). Our data indicate that HSD might be modulating gut microbiota to induce tumor immunity, as ablation of gut microbiota results in loss of HSD-induced tumor immunity. It was reasoned that HSD-associated changes in gut microbiota diversity might be playing a role in NK cells activation and functions in tumor immunity. To identify the changes in gut microbiota, we carried out 16S ribosomal RNA (rRNA) metagenome analysis of stool samples from H, T, and T + HSD groups. The Simson and Shannon diversity plot indicated that there was an increase in both microbiota diversity richness and evenness in T + HSD group as compared to H and T groups (Fig. 5G). We prepared a

detailed Shankey plot for T + HSD microbiome through operational taxonomic unit (OTU) quantitation that showed *Bifidobacterium* as one of the prominent bacterial population detected at species level (fig. S5). Moreover, OTU diversity plot showed prominent up-regulation of *Bifidobacterium* in T + HSD as compared to H group (Fig. 5H). Together, these data indicates a possibility of *Bifidobacterium* as a factor contributing toward HSD-mediated tumor immunity.

FMT from HSD-fed mice results in tumor regression

Our data suggested that HSD-induced tumor immunity requires gut microbiota; therefore, we hypothesized that HSD-mediated tumor

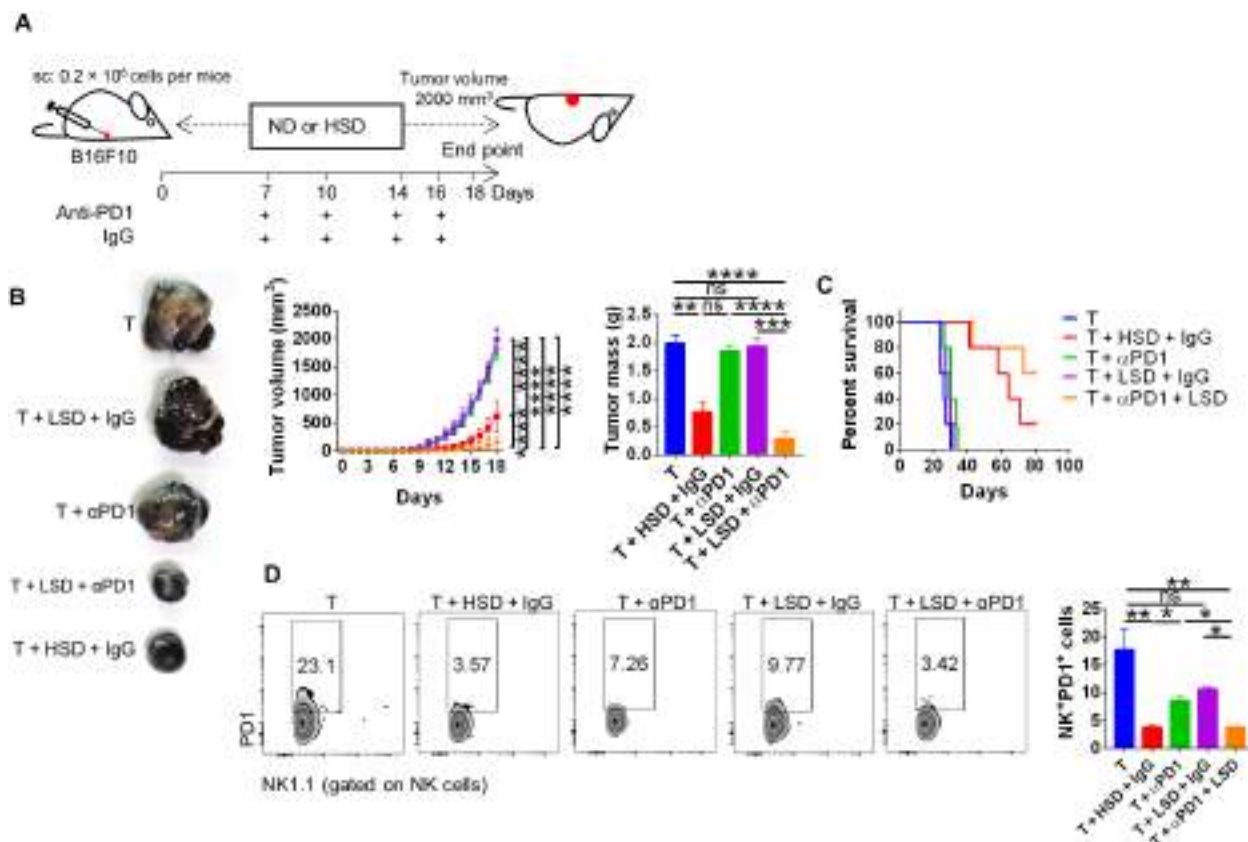


Fig. 4. Use of salt as an adjuvant in combination with suboptimal dose of anti-PD1-neutralizing antibody. (A) Schematic methodology and (B) tumor progression for combinatorial therapy involving salt and suboptimal dose of anti-PD1-neutralizing antibody and (C) its survival curve and (D) the subsequent profiling for PD1 expression on NK cells. * $P < 0.05$, ** $P < 0.01$, *** $P < 0.001$, and **** $P < 0.0001$ (Student's t test or one-way ANOVA).

immunity could be transferred through FMT from donor HSD-fed mice to the AIMD mice fed on ND. To do this, fecal material from mice fed with HSD were transferred through oral gavaging to AIMD mice. These mice were then implanted with B16 cells and were maintained on ND to monitor tumor growth (Fig. 6A). FMT from HSD mice (R) showed significant (~42%) regression of tumor volume and mass with improved survival as compared to AIMD mice receiving FMT from ND-fed mice (NR) (Fig. 6, B and C). The frequency of NK cells increased markedly in the R group as compared to the NR group in the tumor-infiltrating immune cells (Fig. 6, D and E). There was also an increase in NK cell function in R group as observed by increased CD107a expression and increased levels of IFN γ and TNF α (Fig. 6, F and G). Next, to understand the effect of FMT on the gut microbiome of R and NR mice, we carried out quantitative polymerase chain reaction (qPCR)-based profiling of stool samples for the enrichment of bacterial genus. Our qPCR data distinctly showed a 2.5-fold up-regulation of *Bifidobacterium* in the stool samples of R as compared to NR, while there were no significant changes observed in other prominent bacterial genera (Fig. 6H). This comprehensively pointed out that *Bifidobacterium* transfer through FMT to AIMD mice was able to restore NK cell frequency and tumor immunity. Since increased *Bifidobacterium* abundance in the gut was important for elevation in NK cell frequency, we reasoned that soluble factors secreted by *Bifidobacterium* into the circulation might be acting as mediators of this cross-talk. It has been previously reported that one of the by-products of the

benzoate-mevalonate pathway is hippurate. Moreover, this benzoate-mevalonate pathway is an important metabolic pathway of *Bifidobacterium*. Therefore, it was reasoned that increased *Bifidobacterium* in the gut might be influencing the NK cell level and tumor immunity by secreted serum hippurate. Serum metabolites profile of R showed a significant increase in hippurate levels as compared to NR with distinct PCA distribution pattern (Fig. 6, I to K). Together, these data demonstrate that the modulation of gut microbiota by HSD enriches *Bifidobacterium*, which could be transferred to AIMD mice to provide tumor immunity through FMT.

HSD results in increased gut permeability and intratumoral localization of *Bifidobacterium*

Several factors such as epigenetic, dietary, and disease status have been shown to regulate the permeability of the gut, which is important for the gut microbiota composition and integrity (31). It was, therefore, intriguing to understand the effect of HSD on gut permeability. To do this, mice were injected subcutaneously with B16 melanoma and fed with ND, LSD, or HSD, and gut permeability assay was performed using the Evan's blue exclusion and fluorescein isothiocyanate (FITC)-dextran gut permeability assay. We found that there was ~2-fold increase in gut permeability in B16-bearing mice fed with HSD as compared to B16-bearing mice fed with LSD or tumor alone or healthy group (fig. S6A and Fig. 7A). We further tested the gut permeability in tumor bearing WT and RAG1^{-/-} mice and observed

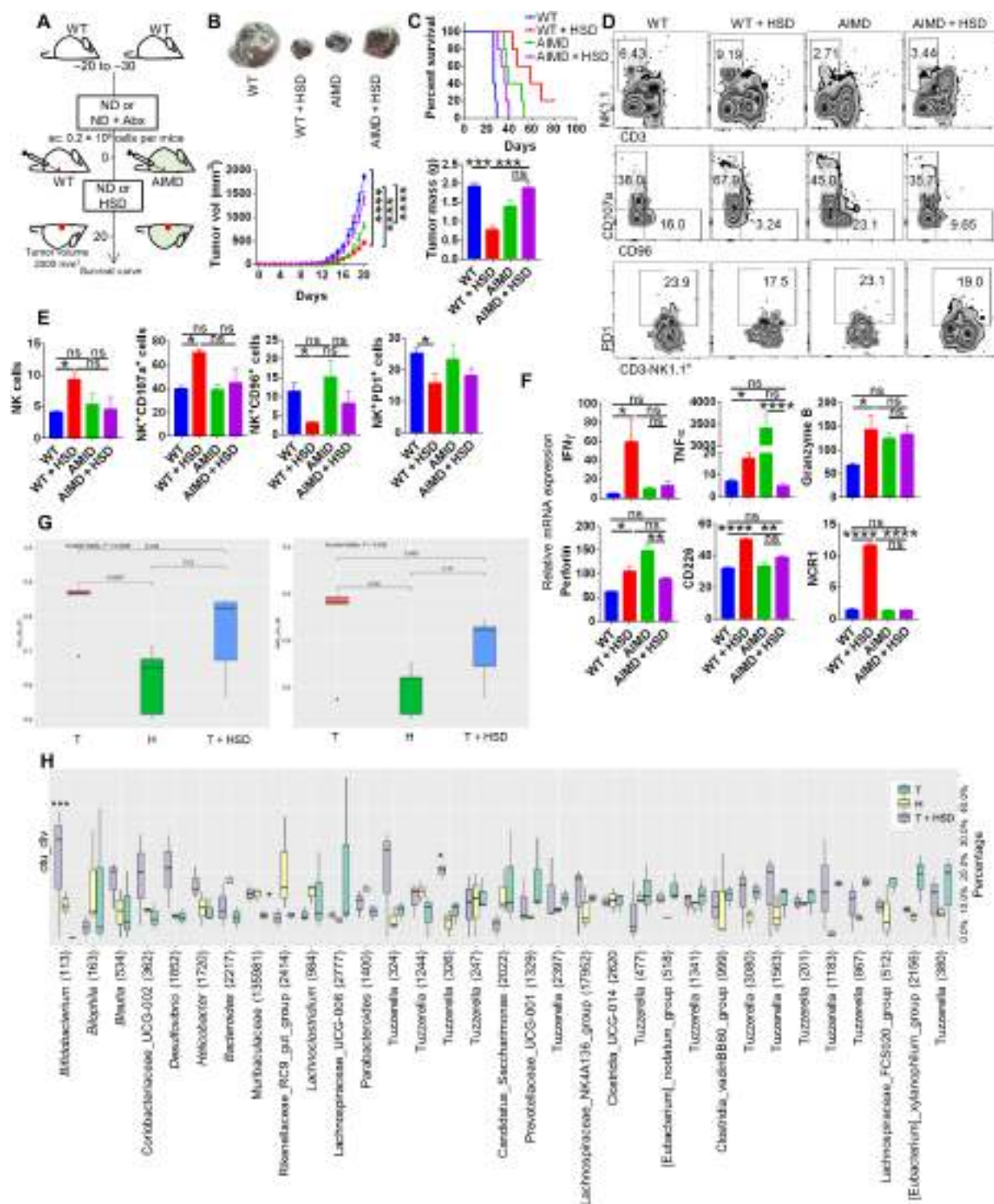


Fig. 5. Changes in gut microbiota associated with HSD in B16 melanoma-bearing mice. The gut microbiota of the mouse was depleted by antibiotic regime, and then the effect of tumor progression was studied. (A) Schematic methodology for AIMD mice generation and comparison of (B) the progression of B16 melanoma in WT and AIMD mice in the presence or absence of HSD and (C) its survival. (D and E) Immunophenotyping results showing NK cells and associated markers along with (F) qPCR relative mRNA expression. The stool samples from the salt-fed mice were used for DNA isolation, and its 16S rRNA metagenomics analysis was carried out. (G) Simson and Shannon diversity plot indicating richness and evenness of the gut microbiota composition. (H) Plot showing OTU % age abundance of bacterial species in different salt groups. * $P < 0.05$, ** $P < 0.01$, *** $P < 0.001$, and **** $P < 0.0001$ (Student's t test or one-way ANOVA).

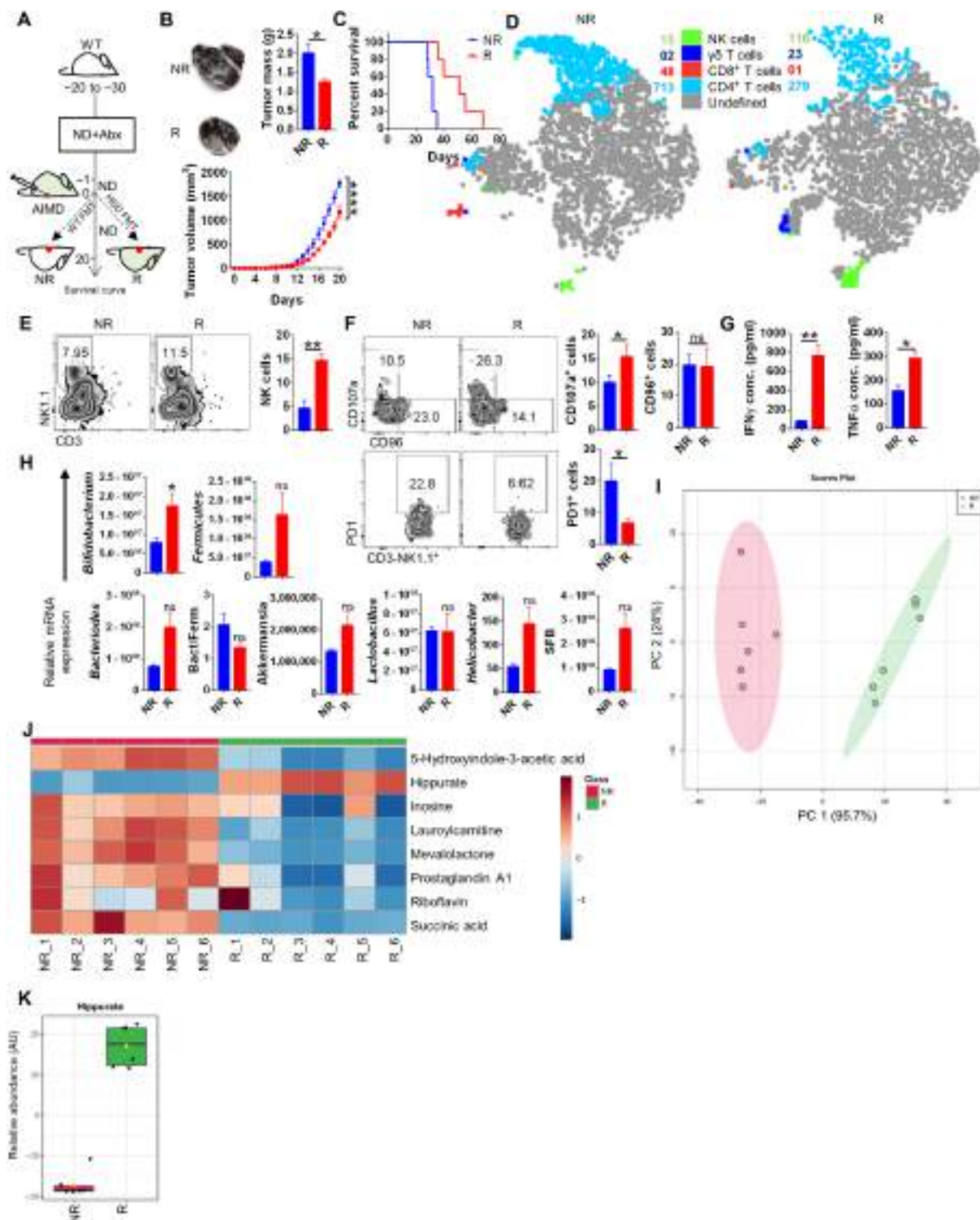


Fig. 6. FMT from HSD donor to AIMD mice restores the gut levels of *Bifidobacterium*. Responder AIMD mice receiving FMT from HSD donor and NR AIMD mice receiving FMT from ND donor were injected with B16. (A) Schematic representation of (B) changes in melanoma progression and (C) survival curve; representative (D) tSNE plot depicting clusters of NK, γδ T, CD4, and CD8 cells. (E and F) Immunophenotyping by FACS and (G) secreted cytokines expression. (H) Microbiota composition through qPCR. (I) PCA plot and (J) heatmap for serum metabolite profile through LC-MS and (K) levels of serum hippurate. * $P < 0.05$, ** $P < 0.01$, and **** $P < 0.0001$ (Student's t test or one-way ANOVA).

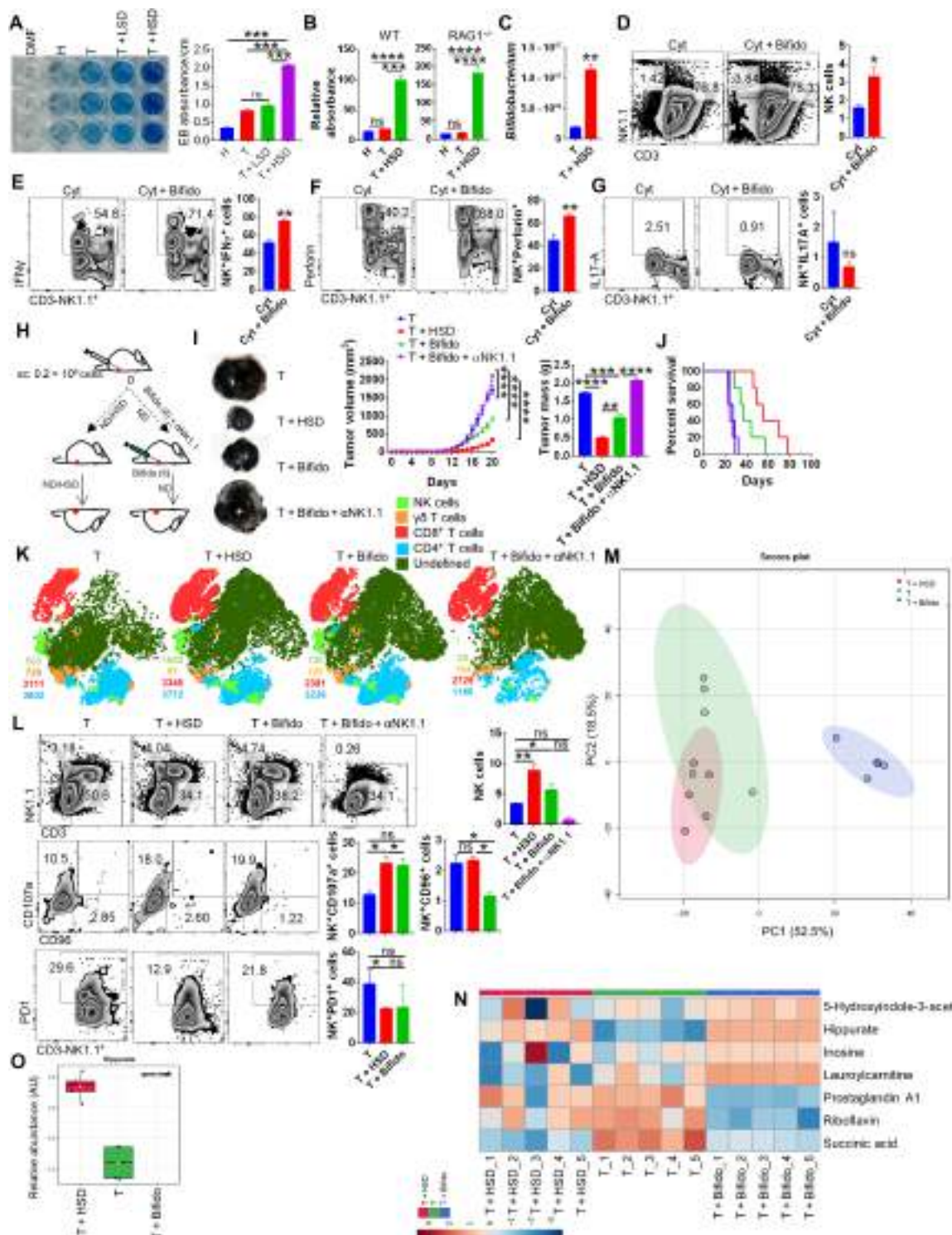


Fig. 7. HSD increases the gut permeability causing *Bifidobacterium* intratumoral localization that boosts NK cells activation. (A) Elution of Evan's blue dye from the colon of H, T, T + LSD, or T + HSD mice and its respective absorbance. (B) Relative absorbance from in situ FITC-dextran gut permeability assay for WT and RAG1^{-/-} mice. (C) qPCR relative quantitation for presence of *Bifidobacterium* in the tumor excised from T or T + HSD mice. Splenocytes from healthy mice were cocultured in the presence or absence of increasing dose of *Bifidobacterium* and stimulated by NK cell-specific cytokines (IL-2 + IL-12). (D) Frequency of NK cells (E to G) and IFN γ , perforin, and IL-17A on NK cells was evaluated through flow cytometry. (H) Schematic representation for (I) tumor progression in mice with HSD or intratumoral *Bifidobacterium* administration with or without anti-NK1.1-neutralizing antibody and (J) its survival curve. it, intratumoral. (K) Representative t-distributed stochastic neighbor embedding (t-SNE) plot depicting clusters of NK, $\gamma\delta$ T, CD4, and CD8 cells. (L) % age frequency of NK cells and associated surface molecules. (M) PCA plot for serum metabolomics profile of T, HSD, and T + *Bifidobacterium*. (N) Heatmap showing normalized levels of selected metabolites. (O) Relative abundance of serum hippurate levels in T, T + HSD, and T + Bifido condition. * $P < 0.05$, ** $P < 0.01$, *** $P < 0.001$, and **** $P < 0.0001$ (Student's t test or one-way ANOVA).

that HSD increases gut permeability of both B16-bearing RAG1^{-/-} and WT mice as compared to healthy control or B16-bearing mice fed with ND (Fig. 7B). These data, together, indicate a possibility of leaking out of gut bacteria due to increased gut permeability in T + HSD group. It was recently shown that there is an existence and colonization of bacteria in human cancers (32, 33). On similar lines, it has been reported that there is intratumoral presence of *Bifidobacterium* (33). Our data suggest that HSD increases the abundance of *Bifidobacterium* and enhances gut permeability. This raises the possibility that gut *Bifidobacterium* may escape and colonize in the melanoma in the B16-bearing mice fed with HSD. To test this hypothesis, we carried out qPCR analysis for *Bifidobacterium* from tumor tissue in B16-bearing mice and B16-bearing mice fed with HSD. Strikingly, we found a ~6-fold increase in *Bifidobacterium* abundance within the melanoma of HSD-fed mice as compared to melanoma of ND-fed mice, suggesting the presence of *Bifidobacterium* in the melanoma tumor mass (Fig. 7C). These data further raise the possibility of direct cross-talk between NK cells and *Bifidobacterium*. To understand the effect of *Bifidobacterium* on NK cells, we cocultured the splenocytes in the presence or absence of NK-stimulating cytokine milieu (IL-2 + IL-12) with an increasing dose of *Bifidobacterium*, we found that in vitro coculture of *Bifidobacterium* with splenocytes was able to up-regulate the zone of the proliferation of NK cells and their frequency by two folds (Fig. 7D and fig. S6B). Further analysis revealed that *Bifidobacterium* increases the NK cell expression of IFN γ and perforin, but not IL-17A (Fig. 7, E to G). Quite interestingly, when *Bifidobacterium* was cocultured with splenocytes in presence of α CD3 (T cell stimulation), we also observed significant changes in IFN γ , IL-17A, and perforin-expressing CD4⁺ and CD8⁺ T cells, without changes in their frequency, indicating that *Bifidobacterium* may also modulate T cell effector response (fig. S6C). These observations led us to hypothesize that introduction of *Bifidobacterium* in the tumor microenvironment may replicate in vitro effects of *Bifidobacterium* and may lead to NK cell up-regulation and tumor immunity even in the absence of HSD. We found that mice fed with ND receiving intratumoral injection of *Bifidobacterium* showed remarkable similarity in regression of tumor and overall survival along with increase NK cell response as compared to HSD-fed mice with no significant changes in other immune cell populations in tumor-infiltrating immune cells (Fig. 7, H to L). Moreover, when NK cells were depleted by anti-mouse NK1.1 antibody, the effect of *Bifidobacterium* administration was blunted (Fig. 7, H to L). We next analysed the serum metabolites profile of *Bifidobacterium*-injected mice and found that hippurate levels are significantly up-regulated upon colonization of *Bifidobacterium* within the tumor as compared to the B16-bearing tumor mice receiving no intratumoral *Bifidobacterium* (Fig. 7, M to O), thus providing evidence that cross-talk between *Bifidobacterium* and NK cells through hippurate is critical to tumor immunity mediated by HSD.

DISCUSSION

Dietary components are identified as important environmental cues that influence human health and immunity (1–3, 34). Excess dietary salt intake is linked to hypertension, cardiovascular complications, and more recently with tissue inflammation in inflammatory bowel disease (IBD), multiple sclerosis associated with enhanced T_H17 cell response and inflammatory macrophages. Despite their effect in exacerbation of inflammatory diseases, the effects of salt,

particularly Na⁺, on cancer immunotherapy has been a topic of great interest for research. In 1933, Shear (35) published the first comprehensive review summarizing the earlier findings and suggested that Na⁺ and K⁺ have modulatory potential on cancer cell growth in vitro. Recently, the protective effect of HSD on the tumor was provided in mouse model where salt was shown to inhibit tumor growth (11, 12, 22). It was shown that HSD modulated MDSC functions that overcome suppressive tumor microenvironment (11). However, cellular and molecular mechanisms that mediated tumor immunity induced by salt are poorly understood.

Hyponatremia is recognized as a common ionic imbalance in patients with cancers and was found to be associated with primary diagnosis (18, 19). HSD intake may remove the hyponatremia condition and result in Na⁺ ion restoration that contribute to the tumor immunity. Our data in tumor-bearing mice show hyponatremia that was resolved with HSD and associated with enhanced tumor immunity. These findings were important in understanding potential factors which contribute to tumor immunity induced by HSD. Na⁺ is known to regulate diverse physiological functions; for example, it influences biological processes that can be sensed by immune cells and affect their differentiation and/or function in tissue inflammation. Since salt removes the immune-suppressive environment within tumor, we hypothesized that HSD-mediated tumor immunity may effectively work in various experimental tumor models. In line with this, our data showed that HSD-fed mice mount a robust regression of tumors of skin, lungs and breast. Our data further demonstrated that HSD effectively controls tumor growth post surgery.

Immune-profiling of TILs, draining lymph nodes (dLN), and spleen for six major immune cell populations viz. CD4⁺ T, CD8⁺ T, $\gamma\delta$ T, macrophages, MDSCs, and NK cells showed a distinct and significant enrichment of the NK cell population in B16-bearing HSD-fed mice. This increase in the frequency of NK cells was accompanied by up-regulation of activation markers and down-regulation of inhibitory markers on NK cells. The dominant role of NK cells in HSD-mediated tumor immunity was abrogated by depletion of NK cells in RAG1^{-/-} mice. Schlichter and MacCoubrey (36) in 1989 showed that low external Na⁺ ion concentration is inhibitory for NK cells cytotoxic activity and could be attenuated by increasing extracellular Na⁺ ion that results in Na⁺ influx inside NK cells. It could be reasoned that hyponatremia condition in cancer patients could be restored by HSD, which may enhance anti-tumor functions of NK cells.

Several shreds of evidence have now shown that the electrolytes balance and acid-base homeostasis controls multiple metabolic pathways, and therefore, any changes associated with ionic imbalance could perturb the metabolic pathways and lead to changes in the serum metabolites level (37). In line with this, our metabolomics profiling data show that metabolites associated with amino acid metabolism, Krebs's cycle, and Warburg effect are significantly perturbed in HSD condition. Hippurate, a benzoic acid and mevalonic acid pathway derivative produced by the host and gut microbiota, showed a prominent increase in the serum of tumor-bearing mice kept on HSD. The elevated hippurate levels in the serum of HSD-fed tumor-bearing mice corroborated with the previously published report on Hippurate as a metabolic biomarker for the cancer patients that responded well to anti-PD1 immunotherapy (21). It is now known that although immunotherapy with antibodies against PD1, CTLA4, or PDL1 demonstrates significant efficacy, a significant number of cancer patients do not respond to immune-checkpoint

therapy. Therefore, efforts have been made to identify factors (such as genetic, gut microbiota, and metabolic) that may predict the immune-responsiveness for checkpoint inhibitor therapy. In the above study, Hatae *et al.* (21) have shown that microbiome-derived hippuric acid is one of the seven identified clinical biomarker of a successful PD1 blockade immunotherapy in patients with cancer (R). In other words, this study provides the link between hippuric acid, anti-PD1 therapy and tumor regression. We found hippurate to be one of the metabolites, common between R and T + HSD serum metabolites profile. Since patients with higher hippurate responded well with anti-PD1 therapy, it was a possibility that increased hippurate levels by salt could help in reducing the dose of anti-PD1 antibody. Strikingly, suboptimal dose of anti-PD1 when combined with salt showed 10-fold decrease in tumor growth. It is also possible that salt, when combined with anti-PD1 therapy, may act as an adjuvant thereby directly enhancing the efficacy of the antibody therapy since hypotonic saline solution had been previously reported as an adjuvant in the treatment of acute haemorrhage condition (38). Another possibility is the involvement of serum hippurate, which is increased upon HSD diet. Spustovo *et al.* (39) in 1989 had shown a direct antitumor activity of hippurate in both in vitro and in vivo models. It is possible that low salt may also modulate serum hippurate levels, which could potentially induce antitumor immunity when combined with anti-PD1 therapy. In summary, we would like to emphasize that we are not sure what may be deriving this effect, and this remains one of the open-ended questions of our study.

In addition, elevated serum hippurate in HSD-fed B16 melanoma-bearing mice opened up the possibility of the involvement of gut microbiota in HSD-mediated tumor immunity, as hippurate is a secretory by-product of gut bacteria (40). Our data show that the effect of HSD was completely abrogated in AIMD mice, indicating the involvement of gut microbiota in HSD-mediated tumor immunity. HSD has been shown to modulate gut microbiota composition in the case of T_H17 cell-mediated autoimmune disorders and is linked with decreased abundance of *Lactobacillus*, *Oscillibacter*, *Pseudoflaonifractor*, *Clostridium*, etc. (5, 30). Our 16S rRNA metagenomics study revealed that HSD-fed mice showed an increase in both richness and evenness of microbiota composition as compared to the healthy control. This was an exciting finding as an increase in the composition of gut microbiota would mean significant changes in the abundance of the bacterial population. Our T + HSD metagenomics data showed a prominent increase in *Bifidobacterium* abundance. Whether an increase in Na⁺ levels in the circulation provides a suitable niche for colonization of *Bifidobacterium* or it inhibits the growth of other commensal bacteria, thereby promoting *Bifidobacterium* abundance, would be interesting to identify. Nonetheless, an increase in gut *Bifidobacterium* abundance by HSD strongly pointed at the crucial role of gut microbiota in HSD mediated-tumor immunity. An increased gut abundance of *Bifidobacterium* upon FMT was expected since we already showed that T + HSD feces has elevated *Bifidobacterium* levels; however, the findings that *Bifidobacterium* abundance was able to protect against melanoma and could lead to elevated NK cells frequency, and serum hippurate levels were interesting.

The influence of gut microbiota on immunological changes is well established (1, 4). The resident commensal bacteria of the gut regulates immune homeostasis and are strongly correlated with IBD (41). *Bifidobacteria longum* and *Lactobacillus* species in the gut,

for example, are involved in regulating the T_{reg} response through IL-10 production (42). It was shown that dietary probiotic supplementation of *Bifidobacterium* could directly enhance NK cell function in elderly subjects in a randomized control meta-analysis study (43). In line with the above trial, it could be asserted that there may be a cross-talk between *Bifidobacterium* and NK cells, which forms the basis of tumor immunity by HSD. Since elevated hippurate levels were observed in R group, we hypothesized that HSD causes an increase in gut *Bifidobacterium* that boosts the serum hippurate levels and promotes NK cell activation and enhances tumor immunity. Moreover, our data provide the first evidence that HSD increases gut permeability and thus facilitates dysbiosis of *Bifidobacterium*, which escapes the gut and colonizes the skin melanoma of the mice. Intratumoral localization of gut microbes has been described as a prominent feature of multiple human cancers, especially since several shreds of evidence now suggest that *Bifidobacterium* accumulation within the tumor may have beneficiary effects (33). Similarly, several studies on anti-PD1 immunotherapy in patients with cancers have now described *Bifidobacterium* as one of the prominent bacterial species of the gut responsible for successful anti-PD1 immunotherapy (44). Together, here, we provide the first evidence of a comprehensive cross-talk mechanism between *Bifidobacterium* and NK cells, which is mediated by hippurate to be the basis of HSD mediated tumor immunity. Our finding also opens up exciting therapeutic avenues for targeting cancer, one of which involves combining anti-PD1 immunotherapy with salt as an adjuvant. The other exciting finding of translational potential is the identification of *Bifidobacterium* as a crucial mediator of NK cell activity and tumor immunity. Through our findings, we propose that a consortium of microbiota mimicking HSD gut microbiota could have exciting translational values against cancer.

MATERIALS AND METHODS

Mice

C57BL/6, BALB/c, and RAG1^{-/-} mice were obtained from the Jackson Laboratory, housed, and maintained in a conventional pathogen-free environment at the small animal facility (SAF) at the Translational Health Science and Technology Institute (THSTI). Prior approval of the animal procedures was obtained from the institutional animal ethics committee (IAEC) (animal ethics approval number IAEC/THSTI/81), and all the experimental procedures involving animals were done in accordance with the guidelines laid by institutional animal ethics committee of THSTI.

Cell lines

B16F10 melanoma cell line was obtained from American Type Culture Collection. LLC and luciferase-expressing 4T1 mammary carcinoma cell lines were gifts from A. Bajaj (Regional Centre Biotechnology, India). LLC and 4T1 cell lines were maintained in RPMI 1640 medium (Invitrogen) complete media containing 10% (v/v) fetal bovine serum (FBS) (Gibco), penicillin (100 U/ml; Sigma-Aldrich), streptomycin (100 µg/ml; Sigma-Aldrich), and 2 mM L-glutamine (Sigma-Aldrich). B16F10 cells were maintained in R10 complete media having RPMI 1640 complete media with 20 mM Hepes (Sigma-Aldrich). None of the cell lines used in this study were found in the Register of Misidentified Cell Lines maintained by the International Cell Line Authentication Committee (<http://iclac.org/databases/cross-contaminations/>).

Syngeneic tumor models

Six- to 8-week-old C57BL/6 male mice were used for B16F10 and LLC injections, while 6- to 8-week-old BALB/c mice were used for 4T1 luciferase injections (11). Cells (0.2 million) were injected either subcutaneously (for melanoma) on the left flank region or were injected intravenously, and the animals were kept on ND, LSD, and HSD as specified in each experiment. Tumor volume was recorded each day until the end point according to the formula: volume (mm^3) = $L \times W \times W/2$, where L is the length and W is the width of the tumor (in millimeters) along with changes in body weight, food, and water intake of the animals. Once tumors reached a volume of 1800 to 2000 mm^3 (end point), animals were euthanized, and their samples were used for various study. In other set of experiment, the tumor animals were left for survival study, and the day of mortality of individual animal was recorded for percent survival curve for 80 days.

Antibodies

Anti-mouse: α -CD45.2 (1:700; 104, BioLegend), α -CD3 (1:700; 145-2C11, BioLegend), α -CD4 (1:1000; GK1.5, BioLegend), α -CD8 (1:1000; 53-6.7, BioLegend), α -NK1.1 (1:700; PK136, BioLegend), α - $\gamma\delta$ TCR (1:700; GL3, BioLegend), α -PD1 (1:500; 29F.1A12, BioLegend), α -CTLA-4 (1:500; UC10-4B9, BioLegend; 1:500), α -TIM3 (1:600; B8.2C12, BioLegend), α -CD107a (1:700; 1D4B, BioLegend), α -CD96 (1:700; 3.3, BioLegend), α -TIGIT (1:700; 1G9, BioLegend), α -Gr1 (1:1500; RB6-8C5, BioLegend), α -CD11b (1:1500; M1/70, BioLegend), α -F4/80 (1:700; BM8, BioLegend), α -CD206 (1:700; C068C2, BioLegend), α -IFN γ (1:500; XMGI.2, BioLegend), α -TNF α (1:500; MP6-XT22, BioLegend), α -IL-17A (1:500; TC11-18H10, BioLegend), α -perforin (1:500; S16009A, BioLegend), and α -Ki67 (1:1000; SolA15, Thermo Fisher Scientific).

Flow cytometry and intracellular cytokine staining

Processed cells from the spleen, lymph nodes, or tumor-infiltrating immune cells were stained for surface markers by fluorescence-tagged antibodies in fluorescence-activated cell sorting (FACS) buffer [phosphate-buffered saline (PBS) with 1% FBS] as previously described (45, 46). For intracellular staining, cells were stained for surface molecules first followed by fixation and permeabilization (BD). For cytokine staining, cells were stimulated for 4 hours with phorbol 12-myristate 13-acetate (PMA; 50 ng/ml; Sigma-Aldrich) and ionomycin (1 $\mu\text{g}/\text{ml}$; Sigma-Aldrich) in the presence of monensin (#554724 GolgiStop, BD Biosciences). Surface markers were stained first for 15 to 20 min at room temperature (RT), and then the cells were fixed in Cytofix and permeabilized with Perm/Wash Buffer using the Fixation Permeabilization Solution Kit (#554714, BD Biosciences). The Fc receptor were blocked with antimouse CD16/32 antibody incubation at RT for 20 min followed by staining with the fluoresceinated antibodies for 20 min at RT in dark. The cells were then washed and analyzed by flow cytometry (Canto II, BD Bioscience). Data analysis was performed using FlowJo software (TreeStar).

Quantitative polymerase chain reaction

RNA extraction from the samples were carried out by using an RNeasy kit (#74104, Qiagen), and complementary DNA (cDNA) were synthesized using an iScript cDNA Synthesis kit (#1708891, Bio-Rad). SYBR Green Gene Expression Assay using the Fast 7500 Dx qPCR System (Applied Biosystems) was then used for performing qPCR. Ct values for the individual samples (genes) was then

normalized to the endogenous control [β -actin/glyceraldehyde-3-phosphate dehydrogenase (GAPDH)] gene expression. All the primer sets were purchased from Sigma-Aldrich. The following primer sets were used (from Applied Biosystems; identifier in parentheses): Ifn γ (Mm01168134_m1), m_tnf_2 (NM_013693), and Gapdh (Mm99999915_g1). The qPCR results were analyzed using SDS 2.1 software. The Ct value of the endogenous control gene was subtracted from the Ct value of each target gene to determine the Ct value change (ΔCt). The relative expression of each gene was then expressed as fold change calculated according to the previously used formula [$\text{POWER}(2, -\Delta\text{Ct}) \times 10,000$] (45).

Enzyme-linked immunosorbent assay

Cells isolated from different tissue samples (stimulated by using PMA and ionomycin as described above) or serum samples were used to perform sandwich enzyme-linked immunosorbent assay (ELISA) for mouse IFN γ or TNF α according to the previously described protocol (45). Briefly, ELISA plates were coated with α -IFN γ (1:250; R4-6A2, BioLegend) or α -TNF α (1:250; MP6-XT22, BioLegend) capture antibody in carbonate coating buffer (100 μl per well) overnight at 4°C. The plate was then blocked with 3% milk powder in PBS. Thereafter, wells were washed with PBS + 0.05% Tween 20 (PBST) twice and incubated with samples (culture soup or serum samples) of 1:1 diluted in assay diluent (PBS + 1% milk powder) for 4 hours at RT. The wells were then washed thrice with PBST and incubated with biotinylated detection antibody α -IFN γ (1:1000; XMGI.2, BioLegend) and α -TNF α (1:1000; MP6-XT22, BioLegend) diluted in assay diluent at RT for 1 hour. The wells were then washed thrice with PBST and incubated with Avidin-HRP (Sigma-Aldrich) 1:10,000 dilution for 30 min at RT. Last, after washing it thrice with PBST, the plate was developed with trimethylboron substrate (50 μl) added in dark for 20 min at RT. The reaction was stopped with 3 M hydrochloric acid, and the absorbance of each well was measured at 550-nm wavelength in spectrophotometer. The corrected absorbance value was obtained by subtracting the absorbance of control samples.

In vivo bioluminescence imaging for lung metastasis

In vivo bioluminescence (BLI) was performed as previously described for 4T1-injected BALB/c mice on day 16 (47). Briefly, animals were injected with D-luciferin (300 mg/kg) intraperitoneally and anesthetized after 20 min with isoflurane 2 to 3% that was reduced to 2% after the animals were transferred to the imaging chamber. BLI in terms of photon emission per second was recorded from each mice by using intelligent visualization software (IVIS) imaging system (PerkinElmer Inc., Waltham, MA) at the optimal imaging time. The BLI data were quantitated by using IVIS software.

Histology

Ten percent (v/v) formalin-fixed tissues were processed, stained with hematoxylin and eosin or Masson's Fontana stain for melanin determination, or processed for immunohistochemistry by using α -Ki67 antibody (48). A certified histologist through blind sampling carried out the assessment of stained slides for the histological score on the scale of 0 to 5 (where 0 meant no staining).

Isolation of tumor-infiltrating immune cells

At the end point of each study, the tumor were excised, and tumor-infiltrating immune cells were isolated by using Percoll density

gradient as previously described with minor modifications (17). Briefly, tumor was dissociated by using a magnetic cell sorting dissociator (Miltenyi Biotec) in the presence of complete media in C-tube. The cells were pelleted at 400g for 6 min and then subjected to enzymatic dissociation in the presence of collagenase type IV (100 U/ml) and deoxyribonuclease I (100 µg/ml) in 2 ml of Hepes buffer containing CaCl₂ (2.5 mg/ml) at 37°C for 1 hour. Dissociated tissues were then strained through 40-µm cell strainer and centrifuged at 400g for 10 min at RT. The supernatant was then slowly layered by 5 ml of 63% Percoll and then 3 ml of 47% Percoll mix followed by 2 ml of 33% Percoll. We centrifuged the gradient at 400g for 25 min without deacceleration. Last, tumor-infiltrating immune cells are collected as faint layer just above 63%, suspended in complete media, and used further.

Depletion of NK cells

NK1.1⁺ cells in mice was depleted by giving intraperitoneal injection of 200 µg of monoclonal antibody (mAb) against NK1.1 (PK136; BioXcell) 24 hours before challenge, and after challenge, the antibodies were injected once weekly as previously described (49). Control group received intraperitoneal injection of isotype control antibody.

IFN γ -neutralizing antibody

For neutralization of IFN γ cytokine, intraperitoneal injection of 200 µg of mAb against IFN γ (XMGI.2, BioXcell) was given twice weekly as previously described. Control group received intraperitoneal injection of isotype control antibody.

Checkpoint immunotherapy by anti-PD1 inhibition

For the suboptimal in vivo inhibition of PD1 in mice, mAb (5 mg/kg) against PD-1 (RMP1-14, BioXcell) was injected intraperitoneally twice weekly starting from day 7 after B16 cell injection as previously described (49, 50). Mice receiving suboptimal dose of PD1 were kept on either ND or LSD. Isotype control antibody was given to control groups.

NK cell sorting from tumor-infiltrating immune cells

Sorting of NK cells from isolated tumor-infiltrating immune cells was carried out on FACSria III (BD Biosciences) based on the surface markers CD3-NK1.1⁺ gating strategy. The purity of the sorted cells were ~95% in postsort analysis. Sorted NK cells were then used for in vitro qPCR assay.

AIMD mice

AIMD was carried out in C57BL/6 mice according to the earlier published protocol (51). Amphotericin-B (0.1 mg/ml; Sigma-Aldrich) was administered orally for 3 days twice daily. From day 3 onward, mice were kept on ampicillin water (1 g/liter; Sigma-Aldrich) along with a cocktail of vancomycin (5 mg/ml; Sigma-Aldrich), metronidazole (10 mg/ml; Sigma-Aldrich), and neomycin (10 mg/ml; Sigma-Aldrich) given through oral gavage twice daily. Animals kept on antibiotics were housed in separate cages due to their coprophagy behavior. Depletion of microbiota was confirmed by absence of colony formation from stool samples upon culture.

Fecal microbiota transplantation

Freshly excreted stool from the mice kept on ND or HSD were collected in 500 µl of sterile PBS directly from the anal orifice opening.

The stool was then vortexed to achieve a homogenous suspension and snap-frozen at -80°C or used immediately for FMT in AIMD mice. One group of AIMD mice received 500 µl of FMT from mice kept on ND (NR), and the other group of mice received 500 µl of FMT from mice kept on HSD (R) through oral gavage for 3 days before the B16 injection. Mice receiving FMT were kept on ND throughout the experiment. The FMT protocol was adapted from previously published study with slight modification (52).

16S rRNA gene qPCR

Bacterial genomic DNA was isolated from mice fecal pellets using a PureLink microbiome DNA purification kit (#A29789, Thermo Fisher Scientific). qPCR was performed with universal 16S primer abundance and normalized to the endogenous control (rpoB/recA) for detecting bacterial. The primer sets used were as follows: Bacteroidetes (5'-GGARCATGTGGTTTAATTCGATGAT-3' and 5'-AGCTGACGACAACCATGCAG-3') Firmicutes (5'-GGAG-YATGTGGTTTAATTCGAAGCA-3' and 5'-AGCTGACGACAACCAT-GCAC-3'), *Bifidobacterium* [5'-TCGCGTC(C/T)GGTGTGAAAG-3' and 5'-CCACATCCAGC(A/G)TCCAC-3'], *Lactobacillus* (5'-AGCAGTAGGG AATCTTCCA-3' and 5'-CACCGCTACACATGGAG-3'), segmented filamentous bacteria (5'-GACGCTGAGGCATGAGAGCAT-3' and 5'-GACGGCACGGATTGTTATTCA-3'), *Helicobacter* (5'-CTTA-ACCATAGAACTGCATTTGAAACTAC-3' and 5'-GGTCGCCTTCG-CAATGAGTA-3'), and *Akkermansia* (5'-CAGCACGTGAAGGTGGGGAC-3' and 5'-CCTTGCGGTTGGCTTCAGAT-3'). The relative abundance of bacteria was calculated according to the “fold change” formula described above.

16S rRNA sequencing and metagenomics analysis

Extraction of genomic DNA was carried out by using a PureLink microbiome DNA purification kit (#A29789, Thermo Fisher Scientific) according to the manufacturer's protocol. The samples were processed and analyzed by CoTeRi (NIBMG, India) for 16S rRNA sequencing using barcoded PCR primers targeting the V3-V4 region followed by libraries for its amplicon using a NEBNext Ultra DNA library preparation kit. These V3-V4 amplicon libraries were quantified and then loaded on the cBot for cluster generation and sequencing. PCR reactions were carried out in quadruplicate and pooled for sequencing on the Illumina HiSeq 2500 instrument, yielding 250-base pair paired-end sequence reads. 16S rRNA raw reads were quality-controlled with Trimmomatic version 0.39 (53). It removes adaptors and trims low-quality bases from the 3' and 5' end of reads to generate decontaminant raw reads and also discards less than 36 nucleotide-trimmed reads. A custom pipeline quantitative insights into microbial ecology (QIIME2, version 2018.11) was used to process and analyze decontaminant raw reads (54). DADA2 program was used to demux and join to generate long sequences. It processes the demultiplexed fastq files and produces sequence abundances. This was followed by grouping of all sequences as OTUs by pretrained Naive Bayes classifier (55), and their taxonomy were assigned by searching with Silva rRNA database release-138 at 97% sequence similarity.

Alpha diversity indices

Shannon and Simpson diversity indices were computed and plotted through R scripts using the vegan, ape, ggplot2, phyloseq, and RAM packages. Differential taxon abundance analysis was also performed by RAM package of R script.

Metabolomics analysis by LC-MS/MS

One hundred microliters of serum samples isolated from animals were mixed with LC-MS grade methanol at 1:3 ratio (serum:methanol), and the clear supernatant was transferred to a sterile LC vials (60 μ l per tube). These samples were kept for drying (mi Vac Duo concentrator, Gene vac Ltd., UK). The dried pellet was then dissolved in 8:2 (v/v) acetonitrile:water for analysis on a chromatography system 5000 (Thermo Fisher Scientific). The separation was performed using an ultra performance liquid chromatography (UPLC) ultimate 3000 using the high strength silica (HSS) T3 column (2.1 \times 100 mm, 1.7 μ m; Waters Corporation) at 40°C. The mobile phase was delivered at 300 μ l/min and consisted of eluent A (water with 0.1% formic acid) and eluent B (acetonitrile with 0.1% formic acid), delivered in a gradient profile: 0 min, 1% B; 1 min, 15% B; 4 min, 35% B; 7 min, 95% B; 9 min, 95% B; 10 min, 1% B; 14 min, 1% B. The electrospray ionization source was operated for both positive mode (+) and negative (–) ionization at 120,000 resolution in MS1 mode and 30,000 resolution in data-dependent MS2 scan mode. The spray voltage used for these positive and negative modes is 4000 and 35,000 volts, respectively. Sheath gas and auxiliary gas were set to 42 and 11, respectively. The mass scan range was 50 to 1000 mass/charge ratio, AGC (automatic gain control) target was at 200,000 ions, maximum injection time was 80 ms for MS, AGC target was 20,000 ions, and maximum injection time 60 ms for MSMS was used.

LC-MS/MS data processing and analysis

All acquired LCMS data were processed using the Progenesis QI for metabolomics (Water Corporation) software using the default setting. The untargeted workflow of Progenesis QI was used to perform retentiontime alignment, feature detection, deconvolution, and elemental composition prediction. Metascope plug of Progenesis QI was then used for the in-house library with accurate mass, fragmentation pattern, and retention time for database search. For further validation, online available spectral library was used. Peaks that had a coefficient of variation of less than 30% in pooled Quality control (QC) sample was kept for the further analysis of data. In addition, manual verification of each detected feature was done for the selection of right peaks. Analysis of data was done by using Metaboanalyst.ca online tool (56), which involves normalization, multivariate statistical analysis, and data annotation. The outlier samples were identified and removed by a combination of PCA and random forest followed by univariant analysis of variance (ANOVA).

Evans blue in vitro permeability assay

The luminal content of the colon was washed using ice-cold PBS followed by injection of 200 μ l of Evans blue solution [1.5% (w/v) in PBS] into the colon. Colon samples were then incubated in Krebs buffer (20 ml) at 5% CO₂ incubator at 37°C for 30 min, washed with acetylcystine solution, then dried at 37°C for 1 day. The dry weight of colon was taken, and it was further incubated with 1 ml of dimethyl fumarate solvent at 55°C for another 24 hours. The absorbance was measured at 610 nm (57).

FITC-dextran permeability assay

FITC-dextran (400 mg/kg; Sigma Aldrich; 4 kD) was orally administered to mice kept without food and water for 4 hours. Serum samples were obtained by retro-orbital bleeding after 4 hours after FITC-dextran administration. The serum fluorescence intensity

was measured at an excitation wavelength of 490 nm and an emission wavelength of 530 nm using a spectrophotometer (58).

Intratumoral quantitation of *Bifidobacterium*

For *Bifidobacterium* quantitation, tumor samples were sterilely collected and sprayed with 70% ethanol and homogenized immediately in 5 ml of sterile PBS containing 0.05% cysteine-HCl. Isolation of genomic DNA was done by a QIAamp PowerFecal DNA kit (QIAGEN, 12830–50) (33). Primer sets against *Bifidobacterium* (as mentioned above) was then used to determine the relative abundance of *Bifidobacterium* in the tumor samples through SYBR Green qPCR method as described above.

In vitro stimulation

For in vitro activation of NK cell freshly isolated splenocytes were processed for single-cell suspension after red blood cell lysis and then seeded 0.1 million cells per well in 96-well plate followed by stimulation with IL-2 (1000 U) and IL-12 (10 ng/ml) for 48 to 72 hours (59, 60). For the activation of T cells, wells of the 96-well plate was precoated with α -CD3 (2 μ g/ml) for overnight at 4°C and then aspirated and seeded with splenocytes for 48 to 72 hours in 5% CO₂ incubator (45). For studying the effect of salt on NK activation, 40 mM NaCl was added to the cytokine mixture (Cyt) containing IL-2 and IL-12 (5). For in vitro assay involving *Bifidobacterium*, the stimulated cells were grown in the presence or absence of *Bifidobacterium* at three different doses viz. 0.025×10^6 , 0.25×10^6 , or 2.5×10^6 colony-forming units (CFU) per well (33). The proliferation of cells was observed under microscope, and the proliferated cells were then further used.

In vivo supplementation of *Bifidobacterium*

For intratumoral inoculation, 2.5×10^6 CFU *Bifidobacterium* (ProBiota Bifido, Seeking Health, WA, USA) was injection within tumor on days 7, 9, 11, and 13 after B16F10 injections in C57BL/6 mice according to the previously described protocol (33).

Statistics

All the results were analyzed and plotted by using GraphPad prism 7.0 software. FACS, qPCR, ELISA, and metabolites studies were compared and analyzed by using one-way ANOVA or Student's *t* test for *n* = 5 mice per group. Graphs are depicted as means with SEM. *P* value of less than 0.05 was considered as statistically significant.

SUPPLEMENTARY MATERIALS

Supplementary material for this article is available at <https://science.org/doi/10.1126/sciadv.abg5016>

[View/request a protocol for this paper from Bio-protocol.](#)

REFERENCES AND NOTES

1. A. L. Kau, P. P. Ahern, N. W. Griffin, A. L. Goodman, J. I. Gordon, Human nutrition, the gut microbiome, and immune system: Envisioning the future. *Nature* **474**, 327–336 (2011).
2. K. M. Maslowski, C. R. Mackay, Diet, gut microbiota and immune responses. *Nat. Immunol.* **12**, 5–9 (2011).
3. S. P. Nobs, N. Zmora, E. Elinav, Nutrition regulates innate immunity in health and disease. *Annu. Rev. Nutr.* **40**, 189–219 (2020).
4. L. Soldati, L. Di Renzo, E. Jirillo, P. A. Ascierio, F. M. Marincola, A. De Lorenzo, The influence of diet on anti-cancer immune responsiveness. *J. Transl. Med.* **16**, 75 (2018).
5. N. Wilck, M. G. Matus, S. M. Kearney, S. W. Olesen, K. Forslund, H. Bartolomaeus, S. Haase, A. Mähler, A. Balogh, L. Markó, O. Vvedenskaya, F. H. Kleiner, D. Tsvetkov, L. Klug, P. I. Costea, S. Sunagawa, L. Maier, N. Rakova, V. Schatz, P. Neubert, C. Frätzer, A. Krannich,

- M. Gollasch, D. A. Grohme, B. F. C rte-Real, R. G. Gerlach, M. Basic, A. Typas, C. Wu, J. M. Titze, J. Jantsch, M. Boschmann, R. Dechend, M. Klei ewietfeld, S. Kempa, P. Bork, R. A. Linker, E. J. Alm, D. N. M ller, Salt-responsive gut commensal modulates T_H17 axis and disease. *Nature* **551**, 585–589 (2017).
6. B. Yi, J. Titze, M. Rykova, M. Feuerrecker, G. Vassilieva, I. Nichiporuk, G. Schelling, B. Morukov, A. Chouk r, Effects of dietary salt levels on monocytic cells and immune responses in healthy human subjects: A longitudinal study. *Transl. Res.* **166**, 103–110 (2015).
 7. W.-C. Zhang, X.-J. Zheng, L.-J. Du, J.-Y. Sun, Z.-X. Shen, C. Shi, S. Sun, Z. Zhang, X. Chen, M. Qin, X. Liu, J. Tao, L. Jia, H. Fan, B. Zhou, Y. Yu, H. Ying, L. Hui, X. Liu, X. Yi, X. Liu, L. Zhang, S.-Z. Duan, High salt primes a specific activation state of macrophages, M(Na). *Cell Res.* **25**, 893–910 (2015).
 8. M. Klei ewietfeld, A. Manzel, J. Titze, H. Kvakan, N. Yosef, R. A. Linker, D. N. Muller, D. A. Hafler, Sodium chloride drives autoimmune disease by the induction of pathogenic T_H17 cells. *Nature* **496**, 518–522 (2013).
 9. T. Morgan, J.-F. Aubert, H. Brunner, Interaction between sodium intake, angiotensin II, and blood pressure as a cause of cardiac hypertrophy. *Am. J. Hypertens.* **14**, 914–920 (2001).
 10. W.-C. Zhang, L.-J. Du, X.-J. Zheng, X.-Q. Chen, C. Shi, B.-Y. Chen, X.-N. Sun, C. Li, Y.-Y. Zhang, Y. Liu, H. Xiao, Q. Leng, X. Jiang, Z. Zhang, S. Sun, S.-Z. Duan, Elevated sodium chloride drives type I interferon signaling in macrophages and increases antiviral resistance. *J. Biol. Chem.* **293**, 1030–1039 (2018).
 11. W. He, J. Xu, R. Mu, Q. Li, D. Lv, Z. Huang, J. Zhang, C. Wang, L. Dong, High-salt diet inhibits tumour growth in mice via regulating myeloid-derived suppressor cell differentiation. *Nat. Commun.* **11**, 1732 (2020).
 12. R. Willebrand, I. Hamad, L. Van Zeebroeck, M. Kiss, K. Bruderek, A. Geuzens, D. Swinnen, B. F. C rte-Real, L. Mark , E. Lebegue, D. Laoui, J. Kemna, T. Kammertoens, S. Brandau, J. A. Van Ginderachter, M. Klei ewietfeld, High salt inhibits tumor growth by enhancing anti-tumor immunity. *Front. Immunol.* **10**, 1141 (2019).
 13. M. T. Orr, L. L. Lanier, Natural killer cell education and tolerance. *Cell* **142**, 847–856 (2010).
 14. G. Alter, J. M. Malenfant, M. Altfeld, CD107a as a functional marker for the identification of natural killer cell activity. *J. Immunol. Methods* **294**, 15–22 (2004).
 15. C. J. Chan, L. Martinet, S. Gilfillan, F. Souza-Fonseca-Guimaraes, M. T. Chow, L. Town, D. S. Ritchie, M. Colonna, D. M. Andrews, M. J. Smyth, The receptors CD96 and CD226 oppose each other in the regulation of natural killer cell functions. *Nat. Immunol.* **15**, 431–438 (2014).
 16. S. Pesce, M. Greppi, F. Grossi, G. Del Zotto, L. Moretta, S. Sivori, C. Genova, E. Marcenaro, PD1/1-PD-Ls checkpoint: Insight on the potential role of NK cells. *Front. Immunol.* **10**, 1242 (2019).
 17. Q. Zhang, J. Bi, X. Zheng, Y. Chen, H. Wang, W. Wu, Z. Wang, Q. Wu, H. Peng, H. Wei, R. Sun, Z. Tian, Blockade of the checkpoint receptor TIGIT prevents NK cell exhaustion and elicits potent anti-tumor immunity. *Nat. Immunol.* **19**, 723–732 (2018).
 18. J. Jaal, T. J gi, A. Altraja, Small cell lung cancer patient with profound hyponatremia and acute neurological symptoms: An effective treatment with fludrocortisone. *Case Rep. Oncol. Med.* **2015**, 286029 (2015).
 19. A. A. Onitilo, E. Kio, S. A. R. Doi, Tumor-related hyponatremia. *Clin. Med. Res.* **5**, 228–237 (2007).
 20. C. A. Harrison, D. Laubitz, C. L. Ohland, M. T. Midura-Kiela, K. Patil, D. G. Besselsen, D. R. Jamwal, C. Jobin, F. K. Ghishan, P. R. Kiela, Microbial dysbiosis associated with impaired intestinal Na⁺/H⁺ exchange accelerates and exacerbates colitis in ex-germ free mice. *Mucosal Immunol.* **11**, 1329–1341 (2018).
 21. R. Hatae, K. Chamoto, Y. H. Kim, K. Sonomura, K. Taneishi, S. Kawaguchi, H. Yoshida, H. Ozasa, Y. Sakamori, M. Akrami, S. Fagarasan, I. Masuda, Y. Okuno, F. Matsuda, T. Hirai, T. Honjo, Combination of host immune metabolic biomarkers for the PD-1 blockade cancer immunotherapy. *JCI Insight* **5**, e133501 (2020).
 22. Y. Xu, W. Wang, M. Wang, X. Liu, M.-H. Lee, M. Wang, H. Zhang, H. Li, W. Chen, High salt intake attenuates breast cancer metastasis to lung. *J. Agric. Food Chem.* **66**, 3386–3392 (2018).
 23. J. Lorenzen, C. E. Lewis, D. McCracken, E. Horak, M. Greenall, J. O. McGee, Human tumour-associated NK cells secrete increased amounts of interferon-gamma and interleukin-4. *Br. J. Cancer* **64**, 457–462 (1991).
 24. M. A. Curran, W. Montalvo, H. Yagita, J. P. Allison, PD-1 and CTLA-4 combination blockade expands infiltrating T cells and reduces regulatory T and myeloid cells within B16 melanoma tumors. *Proc. Natl. Acad. Sci. U.S.A.* **107**, 4275–4280 (2010).
 25. V. Gopalakrishnan, C. N. Spencer, L. Nezi, A. Reuben, M. C. Andrews, T. V. Karpinets, P. A. Prieto, D. Vicente, K. Hoffman, S. C. Wei, A. P. Cogdill, L. Zhao, C. W. Hudgens, D. S. Hutchinson, T. Manzo, M. P. de Macedo, T. Cotechini, T. Kumar, W. S. Chen, S. M. Reddy, R. S. Sloane, J. Galloway-Pena, H. Jiang, P. L. Chen, E. J. Shpall, K. Rezvani, A. M. Alousi, R. F. Chemaly, S. Shelburne, L. M. Vence, P. C. Okhuysen, V. B. Jensen, A. G. Swennes, F. McAllister, E. M. R. Sanchez, Y. Zhang, E. Le Chatelier, L. Zitvogel, N. Pons, J. L. Austin-Breneman, L. E. Haydu, E. M. Burton, J. M. Gardner, E. Sirmans, J. Hu, A. J. Lazar, T. Tsujikawa, A. Diab, H. Tawbi, I. C. Glitza, W. J. Hwu, S. P. Patel, S. E. Woodman, R. N. Amaria, M. A. Davies, J. E. Gershenwald, P. Hwu, J. E. Lee, J. Zhang, L. M. Coussens, Z. A. Cooper, P. A. Futreal, C. R. Daniel, N. A. Ajami, J. F. Petrosino, M. T. Tetzlaff, P. Sharma, J. P. Allison, R. R. Jenq, J. A. Wargo, Gut microbiome modulates response to anti-PD-1 immunotherapy in melanoma patients. *Science* **359**, 97–103 (2018).
 26. W. Li, Y. Deng, Q. Chu, P. Zhang, Gut microbiome and cancer immunotherapy. *Cancer Lett.* **447**, 41–47 (2019).
 27. Y. Li, R. Tinoco, L. El  n, I. Segota, Y. Xian, Y. Fujita, A. Sahu, R. Zarecki, K. Marie, Y. Feng, A. Khateb, D. T. Frederick, S. K. Ashkenazi, H. Kim, E. G. Perez, C.-P. Day, R. S. S. Mu  oz, R. Schmaltz, S. Yooseph, M. A. Tam, T. Zhang, E. Avitan-Hersh, L. Tzur, S. Roizman, I. Boyango, G. Bar-Sela, A. Orian, R. J. Kaufman, M. Bosenberg, C. R. Goding, B. Baaten, M. P. Levesque, R. Dummer, K. Brown, G. Merlino, E. Ruppig, K. Flaherty, A. Ramer-Tait, T. Long, S. N. Peterson, L. M. Bradley, Z. A. Ronai, Gut microbiota dependent anti-tumor immunity restricts melanoma growth in *Rnf5*^{-/-} mice. *Nat. Commun.* **10**, 1492 (2019).
 28. B. Routy, E. Le Chatelier, L. Derosa, C. P. M. Duong, M. T. Alou, R. Daill  re, A. Fluckiger, M. Messaoudene, C. Rauber, M. P. Roberti, M. Fidelle, C. Flament, V. Poirier-Colame, P. Opolon, C. Klein, K. Iribarren, L. Mondrag  n, N. Jacqu  lot, B. Qu, G. Ferrere, C. Cl  menson, L. Mezquita, J. R. Masip, C. Naltet, S. Brosseau, C. Kaderbhai, C. Richard, H. Rizvi, F. Levenez, N. Galleron, B. Quinqu  s, N. Pons, B. Ryffel, V. Minard-Colin, P. Gonin, J.-C. Soria, E. Deutsch, Y. Loriot, F. Ghiringhelli, G. Zalcman, F. Goldwasser, B. Escudier, M. D. Hellmann, A. Eggermont, D. Raoult, L. Albiges, G. Kroemer, L. Zitvogel, Gut microbiome influences efficacy of PD-1-based immunotherapy against epithelial tumors. *Science* **359**, 91–97 (2018).
 29. S. Viald, F. Saccheri, G. Mignot, T. Yamazaki, R. Daill  re, D. Hannani, D. P. Enot, C. Pfirschke, C. Engblom, M. J. Pittet, A. Schlitzer, F. Ginhoux, L. Apetoh, E. Chachaty, P.-L. Woerther, G. Eberl, M. B  ard, C. Ecobichon, D. Clermont, C. Bizet, V. Gaboriau-Routhiau, N. Cerf-Bussan  s, P. Opolon, N. Yessa  d, E. Vivier, B. Ryffel, C. O. Elson, J. Dor  , G. Kroemer, P. Lepage, I. G. Boneca, F. Ghiringhelli, L. Zitvogel, The intestinal microbiota modulates the anticancer immune effects of cyclophosphamide. *Science* **342**, 971–976 (2013).
 30. A. Bier, T. Braun, R. Khasbab, A. Di Segni, E. Grossman, Y. Haberman, A. Leibowitz, A high salt diet modulates the gut microbiota and short chain fatty acids production in a salt-sensitive hypertension rat model. *Nutrients* **10**, 1154 (2018).
 31. C. Chelakkot, J. Ghim, S. H. Ryu, Mechanisms regulating intestinal barrier integrity and its pathological implications. *Exp. Mol. Med.* **50**, 1–9 (2018).
 32. D. Nejman, I. Liviyatan, G. Fuks, N. Gavert, Y. Zwang, L. T. Geller, A. Rotter-Maskowitz, R. Weiser, G. Mallel, E. Gigi, A. Meltser, G. M. Douglas, I. Kamer, V. Gopalakrishnan, T. Dadoosh, S. Levin-Zaidman, S. Avnet, T. Atlan, Z. A. Cooper, R. Arora, A. P. Cogdill, M. A. W. Khan, G. Ologun, Y. Bussi, A. Weinberger, M. Lotan-Pompan, O. Golani, G. Perry, M. Rokah, K. Bahar-Shany, E. A. Rozeman, C. U. Blank, A. Ronai, R. Shaoul, A. Amit, T. Dorfman, R. Kremer, Z. R. Cohen, S. Harnof, T. Siegal, E. Yehuda-Shnaidman, E. N. Gal-Yam, H. Shapira, N. Baldini, M. G. I. Langille, A. Ben-Nun, B. Kaufman, A. Nissan, T. Golan, M. Dadiani, K. Levanon, J. Bar, S. Yust-Katz, I. Barshack, D. S. Peeper, D. J. Raz, E. Segal, J. A. Wargo, J. Sandbank, N. Shental, R. Straussman, The human tumor microbiome is composed of tumor type-specific intracellular bacteria. *Science* **368**, 973–980 (2020).
 33. Y. Shi, W. Zheng, K. Yang, K. G. Harris, K. Ni, L. Xue, W. Lin, E. B. Chang, R. R. Weichselbaum, Y.-X. Fu, Intratumoral accumulation of gut microbiota facilitates CD47-based immunotherapy via STING signaling. *J. Exp. Med.* **217**, e20192282 (2020).
 34. D. C. Nieman, M. A. Lila, N. D. Gillitt, Immunometabolism: A multi-omics approach to interpreting the influence of exercise and diet on the immune system. *Annu. Rev. Food Sci. Technol.* **10**, 341–363 (2019).
 35. M. J. Shear, The r  le of sodium, potassium, calcium, and magnesium in cancer: A review. *Am. J. Can.* **18**, 924–1024 (1933).
 36. L. C. Schlichter, I. C. MacCoubrey, Interactive effects of Na and K in killing by human natural killer cells. *Exp. Cell Res.* **184**, 99–108 (1989).
 37. C. Menni, L. McCallum, M. Pietzner, J. Zierer, A. Aman, K. Suhre, R. P. Mohney, M. Mangino, N. Friedrich, T. D. Spector, S. Padmanabhan, Metabolomic profiling identifies novel associations with electrolyte and acid-base homeostatic patterns. *Sci. Rep.* **9**, 15088 (2019).
 38. J. Schavelzon, Hypotonic saline serum as an adjuvant in the treatment of acute hemorrhage. *Prensa Med. Argent.* **38**, 2735–2737 (1951).
 39. V. Spustov  , C. Oravec, Antitumor effect of hippurate. An experimental study using various mouse tumor strains. *Neoplasma* **36**, 317–320 (1989).
 40. H. J. Lees, J. R. Swann, I. D. Wilson, J. K. Nicholson, E. Holmes, Hippurate: The natural history of a mammalian-microbial cometabolite. *J. Proteome Res.* **12**, 1527–1546 (2013).
 41. M. F. Neurath, Host-microbiota interactions in inflammatory bowel disease. *Nat. Rev. Gastroenterol. Hepatol.* **17**, 76–77 (2020).
 42. S. Sun, L. Luo, W. Liang, Q. Yin, J. Guo, A. M. Rush, Z. Lv, Q. Liang, M. A. Fischbach, J. L. Sonnenburg, D. Dodd, M. M. Davis, F. Wang, *Bifidobacterium* alters the gut microbiota and modulates the functional metabolism of T regulatory cells in the context of immune checkpoint blockade. *Proc. Natl. Acad. Sci. U.S.A.* **117**, 27509–27515 (2020).

43. H. S. Gill, K. J. Rutherford, M. L. Cross, Dietary probiotic supplementation enhances natural killer cell activity in the elderly: An investigation of age-related immunological changes. *J. Clin. Immunol.* **21**, 264–271 (2001).
44. A. Sivan, L. Corrales, N. Hubert, J. B. Williams, K. Aquino-Michaels, Z. M. Earley, F. W. Benyamin, Y. M. Lei, B. Jabri, M.-L. Alegre, E. B. Chang, T. F. Gajewski, Commensal *Bifidobacterium* promotes antitumor immunity and facilitates anti-PD-L1 efficacy. *Science* **350**, 1084–1089 (2015).
45. S. Malik, S. Sadhu, S. Elesela, R. P. Pandey, A. S. Chawla, D. Sharma, L. Panda, D. Rathore, B. Ghosh, V. Ahuja, A. Awasthi, Transcription factor Foxo1 is essential for IL-9 induction in T helper cells. *Nat. Commun.* **8**, 815 (2017).
46. S. Roy, A. Awasthi, ATP triggers human Th9 cell differentiation via nitric oxide-mediated mTOR-HIF1 α pathway. *Front. Immunol.* **10**, 1120 (2019).
47. J.-B. Kim, K. Urban, E. Cochran, S. Lee, A. Ang, B. Rice, A. Bata, K. Campbell, R. Coffee, A. Gorodinsky, Z. Lu, H. Zhou, T. K. Kishimoto, P. Lassota, non-invasive detection of a small number of bioluminescent cancer cells *in vivo*. *PLOS ONE* **5**, e9364 (2010).
48. Z. A. Rizvi, N. Puri, R. K. Saxena, Evidence of CD1d pathway of lipid antigen presentation in mouse primary lung epithelial cells and its up-regulation upon *Mycobacterium bovis* BCG infection. *PLOS ONE* **13**, e0210116 (2018).
49. T. A. Triplett, K. C. Garrison, N. Marshall, M. Donkor, J. Blazeck, C. Lamb, A. Qerqez, J. D. Dekker, Y. Tanno, W.-C. Lu, C. S. Karamitros, K. Ford, B. Tan, X. M. Zhang, K. McGovern, S. Coma, Y. Kumada, M. S. Yamany, E. Sentandreu, G. Fromm, S. Tiziani, T. H. Schreiber, M. Manfredi, L. I. R. Ehrlich, E. Stone, G. Georgiou, Reversal of indoleamine 2,3-dioxygenase-mediated cancer immune suppression by systemic kynurenine depletion with a therapeutic enzyme. *Nat. Biotech.* **36**, 758–764 (2018).
50. M. T. Wolf, S. Ganguly, T. L. Wang, C. W. Anderson, K. Sadtler, R. Narain, C. Cherry, A. J. Parrillo, B. V. Park, G. Wang, F. Pan, S. Sukumar, D. M. Pardoll, J. H. Elisseeff, A biologic scaffold-associated type 2 immune microenvironment inhibits tumor formation and synergizes with checkpoint immunotherapy. *Sci. Transl. Med.* **11**, eaat7973 (2019).
51. A. Zarrinpar, A. Chaix, Z. Z. Xu, M. W. Chang, C. A. Marotz, A. Saghatelian, R. Knight, S. Panda, Antibiotic-induced microbiome depletion alters metabolic homeostasis by affecting gut signaling and colonic metabolism. *Nat. Commun.* **9**, 2872 (2018).
52. S. M. Kim, J. R. DeFazio, S. K. Hyoju, K. Sangani, R. Keskey, M. A. Krezalek, N. N. Khodarev, N. Sangwan, S. Christley, K. G. Harris, A. Malik, A. Zaborin, R. Bouziat, D. R. Ranoa, M. Wiegner, J. D. Ernest, B. A. Shakhshere, I. D. Fleming, R. R. Weichselbaum, D. A. Antonopoulos, J. A. Gilbert, L. B. Barreiro, O. Zaborina, B. Jabri, J. C. Alverdy, Fecal microbiota transplant rescues mice from human pathogen mediated sepsis by restoring systemic immunity. *Nat. Commun.* **11**, 2354 (2020).
53. A. M. Bolger, M. Lohse, B. Usadel, Trimmomatic: A flexible trimmer for Illumina sequence data. *Bioinformatics* **30**, 2114–2120 (2014).
54. E. Bolyen, J. R. Rideout, M. R. Dillon, N. A. Bokulich, C. C. Abnet, G. A. Al-Ghalith, H. Alexander, E. J. Alm, M. Arumugam, F. Asnicar, Y. Bai, J. E. Bisanz, K. Bittinger, A. Brejnrod, C. J. Brislawn, C. T. Brown, B. J. Callahan, A. M. Carballo-Rodriguez, J. Chase, E. K. Cope, R. Da Silva, C. Diener, P. C. Dorrestein, G. M. Douglas, D. M. Durall, C. Duvallet, C. F. Edwards, M. Ernst, M. Estaki, J. Fouquier, J. M. Gauglitz, S. M. Gibbons, D. L. Gibson, A. Gonzalez, K. Gorlick, J. Guo, B. Hillmann, S. Holmes, H. Holste, C. Huttenhower, G. A. Huttley, S. Janssen, A. K. Jarmusch, L. Jiang, B. D. Kaehler, K. B. Kang, C. R. Keefe, P. Keim, S. T. Kelley, D. Knights, I. Koester, T. Kosciorek, J. Kreps, M. G. I. Langille, J. Lee, R. Ley, Y.-X. Liu, E. Loftfield, C. Lozupone, M. Maher, C. Marotz, B. D. Martin, D. McDonald, L. J. McIver, A. V. Melnik, J. L. Metcalf, S. C. Morgan, J. T. Morton, A. T. Naimey, J. A. Navas-Molina, L. F. Nothias, S. B. Orchanian, T. Pearson, S. L. Peoples, D. Petras, M. L. Preuss, E. Priesse, L. B. Rasmussen, A. Rivers, M. S. Robeson, P. Rosenthal, N. Segata, M. Shaffer, A. Shiffer, R. Sinha, S. J. Song, J. R. Spear, A. D. Swafford, L. R. Thompson, P. J. Torres, P. Trinh, A. Tripathi, P. J. Turnbaugh, S. Ul-Hasan, J. J. J. van der Hoof, F. Vargas, Y. Vázquez-Baeza, E. Vogtmann, M. von Hippel, W. Walters, Y. Wan, M. Wang, J. Warren, K. C. Weber, C. H. D. Williamson, A. D. Willis, Z. Z. Xu, J. R. Zaneveld, Y. Zhang, Q. Zhu, R. Knight, J. G. Caporaso, Reproducible, interactive, scalable and extensible microbiome data science using QIIME 2. *Nat. Biotech.* **37**, 852–857 (2019).
55. N. A. Bokulich, B. D. Kaehler, J. R. Rideout, M. Dillon, E. Bolyen, R. Knight, G. A. Huttley, J. Gregory Caporaso, Optimizing taxonomic classification of marker-gene amplicon sequences with QIIME 2's q2-feature-classifier plugin. *Microbiome* **6**, 90 (2018).
56. J. Chong, D. S. Wishart, J. Xia, Using MetaboAnalyst 4.0 for Comprehensive and Integrative Metabolomics Data Analysis. *Curr. Protoc. Bioinformatics* **68**, e86 (2019).
57. Q. Mei, L. Diao, J. Xu, X. Liu, J. Jin, A protective effect of melatonin on intestinal permeability is induced by diclofenac via regulation of mitochondrial function in mice. *Acta Pharmacol. Sin.* **32**, 495–502 (2011).
58. J. Yang, I. Elbaz-Younes, C. Primo, D. Murungi, K. D. Hirschi, Intestinal permeability, digestive stability and oral bioavailability of dietary small RNAs. *Sci. Rep.* **8**, 10253 (2018).
59. J. F. Clinthorne, E. Bel, D. M. Duriancik, E. M. Gardner, NK cell maturation and function in C57BL/6 mice are altered by caloric restriction. *J. Immunol.* **190**, 712–722 (2013).
60. S. Kim, K. Iizuka, H.-S. P. Kang, A. Dokun, A. R. French, S. Greco, W. M. Yokoyama, *In vivo* developmental stages in murine natural killer cell maturation. *Nat. Immunol.* **3**, 523–528 (2002).

Acknowledgments: We are thankful to A. Bajaj for providing us LLC and 4T1 luciferase cell lines. We acknowledge the histological studies performed by Amit and his team at Biobank, ILBS. We express gratitude to CoTeRi, NIBMG for performing 16S rRNA metagenome analysis for our samples. We also acknowledge SAF-THSTI and “Immunology Core” of THSTI for providing the resources and support in conducting experiments and data analysis. **Funding:** We acknowledge the grant support provided by DBT and DST for this work. Z.A.R. acknowledges the fellowship support by SERB. **Author contributions:** Conceived, designed, and supervised the study: A.A. Designed and performed the experiments: Z.A.R. and R.D. Animal experiments: Z.A.R. and R.D. FACS: Z.A.R., R.D., and D.K.R. Metabolomics: Z.A.R., Y.K., and S.K.G. qPCR: Z.A.R. and M.R.T. ELISA: Z.A.R. Metagenomics analysis: S.K. Analyzed the data: Z.A.R., R.D., S.S., and D.R. Contributed reagents/materials/analysis tools: A.A. Wrote the manuscript: Z.A.R. and A.A. **Competing interests:** The authors declare that they have no competing interests. **Data and materials availability:** All data needed to evaluate the conclusions in the paper are present in the paper and/or the Supplementary Materials.

Submitted 9 January 2021

Accepted 21 July 2021

Published 10 September 2021

10.1126/sciadv.abg5016


Citation: Z. A. Rizvi, R. Dalal, S. Sadhu, Y. Kumar, S. Kumar, S. K. Gupta, M. R. Tripathy, D. K. Rathore, A. Awasthi, High-salt diet mediates interplay between NK cells and gut microbiota to induce potent tumor immunity. *Sci. Adv.* **7**, eabg5016 (2021).


IL-9 aggravates SARS-CoV-2 infection and exacerbates associated airway inflammation

Received: 13 July 2022

Accepted: 30 June 2023

Peer-reviewed online: 10 July 2023

 Check for updates

Srikanth Sadhu^{1,2}, Rajdeep Dalal¹, Jyotsna Dandotiya¹, Akshay Binayke¹, Virendra Singh¹, Manas Ranjan Tripathy^{1,2}, Vinayaka Das¹, Sandeep Goswami², Shakti Kumar³, Zaigham Abbas Rizvi^{1,2} & Amit Awasthi^{1,2} 

SARS-CoV-2 infection is known for causing broncho-alveolar inflammation. Interleukin 9 (IL-9) induces airway inflammation and bronchial hyper responsiveness in respiratory viral illnesses and allergic inflammation, however, IL-9 has not been assigned a pathologic role in COVID-19. Here we show, in a K18-hACE2 transgenic (ACE2.Tg) mouse model, that IL-9 contributes to and exacerbates viral spread and airway inflammation caused by SARS-CoV-2 infection. *ACE2.Tg* mice with CD4⁺ T cell-specific deficiency of the transcription factor Forkhead Box Protein O1 (Foxo1) produce significantly less IL-9 upon SARS-CoV-2 infection than the wild type controls and they are resistant to the severe inflammatory disease that characterises the control mice. Exogenous IL-9 increases airway inflammation in Foxo1-deficient mice, while IL-9 blockade reduces and suppresses airway inflammation in SARS-CoV-2 infection, providing further evidence for a *Foxo1*-IL-9 mediated Th cell-specific pathway playing a role in COVID-19. Collectively, our study provides mechanistic insight into an important inflammatory pathway in SARS-CoV-2 infection, and thus represents proof of principle for the development of host-directed therapeutics to mitigate disease severity.

Severe acute respiratory syndrome coronavirus 2 (SARS-CoV-2) causes coronavirus disease 2019 (COVID-19). COVID-19 symptoms range from mild to severe pneumonia and acute respiratory distress syndrome¹. SARS-CoV-2 infection leads to hyperactivation of immune cells, which further induces inflammatory cascade, broncho-alveolar inflammation and immunopathology². Use of dexamethasone, an anti-inflammatory drug, resulted in lower mortality and severity in patients hospitalized with COVID-19³, indicating that immune suppression is effective in controlling the severity and mortality. In addition, we identified that SARS-CoV-2 infection, in animal model, contributes to the extra-pulmonary pathologies which include cardiovascular complications and thymic atrophy⁴.

Although the precise mechanism of disease pathogenesis and lung pathology that lead to hyper-inflammatory response is not fully

understood, autopsy histopathology of pulmonary samples revealed increased accumulation of eosinophils, basophils, neutrophils and perivascular and septal mast cells in COVID-19^{5–7}. Single-cell landscape of bronchoalveolar immune cells in patients with COVID-19 shows that one of the prominent cell types is Mast cells^{7,8}. In line with this, mast cells-derived proteases, chymase and eosinophil-associated mediators are found to be elevated in sera of COVID-19 patient and lung autopsies^{5,8}. Interleukin 9 (IL-9), a common γ chain family cytokine primarily produced by Th9 cells⁹, promotes mast cell growth and function in allergic inflammation¹⁰. Although IL-9 plays an essential role in severe airway inflammation and bronchial hyper responsiveness in asthma and Respiratory Syncytial Virus (RSV) infection^{11,12}, the role of IL-9 is not yet identified in SARS-CoV-2 infection, and its associated immunopathology.

¹Centre for Immunobiology and Immunotherapy, Translational Health Science and Technology Institute, NCR-Biotech Science Cluster, 3rd Milestone, Faridabad 121 001 Haryana, India. ²Immunology-Core Laboratory, Translational Health Science and Technology Institute, NCR-Biotech Science Cluster, 3rd Milestone, Faridabad 121 001 Haryana, India. ³Centre for Human Microbiome and Anti-Microbial Resistance, Translational Health Science and Technology Institute, NCR-Biotech Science Cluster, 3rd Milestone, Faridabad-Gurgaon Expressway, Faridabad 121001 Haryana, India. ✉e-mail: aawasthi@thsti.res.in

IL-9 induction in Th9 cells requires a distinct set of transcription factors. *Pu.1* is one of the key transcription factors essential for IL-9 induction and Th9 cell differentiation⁹. Other transcription factors, Interferon (IFN) regulatory factor 1 (*Irf-1*)¹³, *Irf-4*¹⁴, Basic leucine zipper transcription factor, ATF-like (*Batf*)¹⁵ and Hypoxia-inducible factor 1- α (*Hif-1 α*)^{16,17}, were found to be associated with the Th9 cells differentiation and functions. We have identified that *Foxo1*, a forkhead family transcription factor, is essential for IL-9 induction not only in Th9 cells but other Th subsets¹⁸. In addition, the role of *Foxo1* is well documented in T cell homeostasis and tolerance through interplay between effector and regulatory T cell¹⁹. While *Foxo1* regulates Th17^{20–22} cell functions, it is essential for the generation and functions of Foxp3⁺ Tregs and Th9 cells²³.

This study aims to investigate the role of interleukin-9 (IL-9) in COVID-19 pathogenesis. We show that hACE2.Tg mice with CD4⁺ T cell-specific deficiency of the transcription factor *Foxo1* are resistant to severe inflammation. Further, we also observe that exogenous IL-9 increases airway inflammation in *Foxo1*-deficient mice, while IL-9 blockade reduces and suppresses airway inflammation in SARS-CoV-2 infection. Here we unravel the role of *Foxo1*-IL-9 axis in SARS-CoV-2 infection, and its associated airway inflammation and immunopathology. These findings provide important mechanistic insights in understanding role of *Foxo1*-IL-9 axis in COVID-19 and could pave the way for the development of host-directed therapeutics to mitigate respiratory viral illness and disease severity.

Results

IL-9 promotes the severity of SARS-CoV-2 infection and associated lung inflammation

We show that IL-9 levels were elevated in active COVID-19 patients infected with ancestral strain during the first wave of pandemic in mid-2020 (Fig. 1a; Supplementary Table 1). First we tested the acquisition of mutations in the ancestral strain of SARS-CoV2, we used in this study by performing sequencing followed by minor variant analysis. Minor variant analysis indicated the presence of five single nucleotide variants (SNVs) in ancestral strains of SARS-CoV-2 (Supplementary Table 2). None of these SNVs were found to be in the cleavage site of virus. Therefore it is highly unlikely to affect infectivity, lethality of the virus or weaken the virus's pathogenicity. This is supported by the experimental evidences we provided subsequently in which we found that infection of hACE2.Tg mice with ancestral strain of SARS-CoV2 causes lethality and mice become moribund post infection as reported earlier^{24,25}.

To test the role of IL-9, we infected hamster and ACE2.Tg mice with ancestral strain of SARS-CoV2. Similar to active COVID-19 patients, IL-9 was found to be upregulated in the lungs of SARS-CoV-2-infected hamster and ACE2.Tg mice (Supplementary Fig. 1b; Fig. 1b, c; Supplementary Fig. 2a, b). IL-9 is primarily produced by Th9 cells but Th2, Th17 and Foxp3⁺ Tregs also produce IL-9^{18,26}. We tested the mRNA expression of genes, *Pu.1*, *Irf-1*, signal transducer and activator of transcription-5 (*Stat-5*), *Stat-6*, *Bat-f* that are associated with Th9 cells^{9,10,13,15}. We found that genes that are associated with Th9 cells are upregulated in the lungs of SARS-CoV-2-infected hamster and ACE2.Tg mice (Supplementary Fig. 2c–e), indicating the association of Th9 cells in SARS-CoV-2 infection.

To determine the role of IL-9 in SARS-CoV-2 infection, anti-IL-9 neutralizing antibody was given to ACE2.Tg mice during SARS-CoV-2 infection at indicated time points (Fig. 1d, e). As compared to SARS-CoV-2-infection and Remdesivir (RDV) treatment, ACE2.Tg mice treated with anti-IL-9 antibody treatment resulted in rescuing weight loss and lung haemorrhage with the reduction of lung viral load (Fig. 1f, g; Supplementary Fig. 2f, g). Similar to RDV, anti-IL-9 antibody treatment decreased immune cells infiltration, mucus production, thickening of blood vessels and mild hypertrophy and mast cell accumulation in the SARS-CoV-2-infected lungs of ACE2.Tg mice (Supplementary Fig. 2h).

Anti-IL-9 antibody treatment decreased inflammatory cytokines, IL-9, IL-4, IL-17 and IFN- γ and replenish the CD4, CD8 and $\gamma\delta$ T cells in the BAL (Supplementary Fig. 3a–e) and expression of *Il9*, *Il4*, *Il5*, *Il6*, and Th9 cell-associated transcription factors, *Foxo1*, *Stat5*, *Stat6*, *Irf4*, *Bat-f*, *Gata3*, and *Irf1* (Supplementary Fig. 3f, g) together with allergic markers, chemokine (C-C motif) ligand 2 (*Ccl2*), CXC chemokine ligand 5 (*Cxcl5*), *Cxcl10*, (Tryptophan hydroxylase 1) *Tph1*, (high-affinity IgE receptor) *Fcer1* in the lung tissue samples of ACE2.Tg mice (Supplementary Fig. 3h). Contrary to IL-9 neutralization, intranasal administration of exogenous IL-9 enhanced severity of SARS-CoV-2 infection in ACE2.Tg mice as indicated by weight loss, lung lesions and viral load associated with an increased frequency of mast cells, and eosinophils in the Bronchoalveolar lavage (BAL) (Fig. 1h–l; Supplementary Fig. 1a; Supplementary Fig. 4a, b). In line with this, lung histology indicated an overall increased in immune cell infiltration, and mucus production upon IL-9 treatment in SARS-CoV-2-infected ACE2.Tg mice (Supplementary Fig. 4c). Interestingly, we found that IL-9 enhanced infection of Omicron variant of SARS-CoV-2 in ACE2.Tg mice, as indicated by loss of body weight, increased lung lesions and viral load (Fig. 1m, n; Supplementary Fig. 4d) with increased infiltration of immune cells and lung tissue damage (Supplementary Fig. 4e). We performed the minor variant analysis of Omicron stock we used in this study and identified that there are 24 SNVs. However, none of these SNVs are found in the cleavage site of the Omicron (Supplementary Table 2), indicating unlikely possibility to affect infectivity and pathogenicity of the Omicron variant is known to cause a milder infection with a reduced mortality²⁷.

Anti-viral pathways include IFN-stimulated genes (ISGs) and anti-viral genes, are critical for anti-viral immunity^{28,29}. We found that anti-IL-9 antibody, as compared to control, treatment increased the expression of ISGs, *Irf3*, *Irf7*, *Irf9*, *Ifnb*, *Ifnar1*, *Ifnar2* and Interferon-induced transmembrane proteins (*Ifitm*), and anti-viral genes, adenosine deaminase acting on RNA (*Adar*), Ribonuclease L (*Rnase L*), oligoadenylate synthase2 (*Oas2*), *Oas3*, *Oas1g*, *Irf3*, *Irf7*, and *Irf9* (Fig. 1p–r). In Contrary, exogenous IL-9 inhibited the expression of anti-viral genes (*Oas2*, *Oas1g*, and *Oas3*) and ISGs (*Irf3*, *Irf7*, *Irf9*, *Ifn- α* and *Ifn- β*) in the lungs of SARS-CoV-2-infected ACE2.Tg mice (Supplementary Fig. 4f–h). In addition, we found that IL-9 treatment increased viral load in human alveolar adenocarcinoma-derived epithelial cells (Supplementary Fig. 4i). Moreover, compared to untreated ACE2.Tg mice, IL-9 treatment enhanced IL-9, IL-4, IFN- γ , and IL-13 in the BAL and IL-9R expression in the lung tissues of SARS-CoV-2 infected ACE2.Tg mice and adenocarcinomic human alveolar basal epithelial cells (A459) cell in vitro (Supplementary Fig. 5a–f).

To address the role of IL-9 in regulating the activity of the transgenic K18 promoter, which might regulate the expression of the transgenic hACE2, we performed Western Blot experiment in which we tested the expression of hACE2 at protein level in the presence or absence of IL-9 treatment. Briefly, K18hAce2 mice were administered rIL-9 (500 ng/mice) or vehicle intranasally for 24 h before euthanising the mice. Lungs from these were homogenised in protein lysis buffer for Western Blot analysis using anti-human Ace2 antibody. Our data indicated that IL-9 treatment did not increase, as compared to control treatment, hACE2 expression in K18hACE2.Tg mice (Supplementary Fig. 5g).

To further substantiate this finding, we used the intestinal epithelial cell line, Caco2, which is known to express Ace2^{30,31}. Briefly, Caco2 cell line was treated with recombinant human IL-9 (10 ng/ml) for 24 h. Post IL-9 treatment, these treated cells were lysed with protein lysis buffer for further Western Blot analysis. Our results indicate that IL-9 treatment did not enhance Ace2 expression in Caco2 cells (Supplementary Fig. 5g), suggesting that IL-9 is not able to increase expression of hACE2, and thus may not influence the expression of the transgenic hACE2 in a non-physiological manner.

Fig. 1 | IL-9 promotes the severity of SARS-CoV-2 Infection and associated lung inflammation. Role of IL-9 was studied in COVID-19 patients and in hACE2 transgenic mice by using neutralizing monoclonal IL-9 antibody. We isolated the PBMCs from Healthy (9 individuals) and COVID-19 RT-PCR positive ($n = 9$) individuals and isolated the cDNA from these PBMCs. **a** Relative mRNA expression ($2^{-\Delta\Delta C_t}$) of *IL9* in active COVID-19 patients ($n = 9$) and healthy individuals ($n = 9$), $^{**}p < 0.01$, using student's t test; bar graph represents as a mean \pm SEM. **b** Percentage frequency of CD4⁺ IL-9⁺ cells in BALF samples of hACE2 mice ($^{*}p < 0.05$; students t test) bar graph represents as a mean \pm SEM. **c** Relative mRNA expression of *IL9* in lung samples ($^{*}p = 0.0428$; students t test); bar graph represents as a mean \pm SEM. **d** Pictorial diagram showing therapeutic regime of α IL-9 and RDV (created with BioRender.com). **e** Quantitation of secretory IL-9 in BALF samples by ELISA ($^{****}p < 0.0001$; one-way ANOVA followed by Tukey's Multiple comparison test); bar graph represents as a mean \pm SEM. **f** Percentage change in body weight ($n = 5$; two-way ANOVA followed by Tukey's multiple comparison test. $^{**}p = 0.0185$, $^{***}p = 0.0006$). **g** Relative viral load in lungs measured by qRT-PCR, $^{****}p < 0.0001$ (one-way ANOVA followed by Tukey's multiple comparison test). **h** Percentage change in body weight ($n = 5$). Two-way ANOVA followed by Tukey's multiple

comparison test. $^{*}p = 0.0369$. **i** Gross morphological changes of lungs ($n = 5$); black arrows represent dark red lung lesions. **j** Relative viral load was measured by qRT-PCR; $^{****}p < 0.0001$ (one-way ANOVA followed by Tukey's multiple comparison test); bar represents as a mean \pm SEM. **k** Representative images show the Toluidine blue staining and bar graph represents histological score ($\times 60$ magnifications; 50 μ m scale bar) arrow represents mast cells. **l** Mast cell percentages were determined in BALF; $^{***}p = 0.0003$, one-way ANOVA followed by Tukey's multiple comparison test. **m** Representative image shows gross morphological changes in Omicron (B.1.1.529) infected lungs. **n** Viral load in infected (B.1.1.529) mice ($n = 5$) or mice treated with rIL-9 (500 ng/mice) measured in the lungs by qPCR ($^{*}p = 0.0360$). **o** Representative FACS zebra plot and its corresponding bar graph showing percentage frequency of IL-9⁺, IL-4⁺. $^{*}p = 0.0501$, $n = 4$. **p–r** Relative mRNA expression of transcription factors genes *Irf3*, *Irf7*, and *Irf9*; ISG's genes (*Irfn- β* , *Irfn- α* , *Irfn- γ* , *Irfn- δ*); and anti-viral genes (*Adar*, *Oas1g*, *Oas2*, *Oas3*, *RnaseL*) were measured in lung tissues ($n = 4$ mice per group). Bars show mean of \pm SEM. $^{*}p = 0.0201$, $^{**}p = 0.0061$, $^{***}p = 0.0002$, $^{****}p < 0.0001$, ns = non-significant (two-way ANOVA followed by Tukey's multiple comparison test). Source data are provided as a Source data file.

frequency of eosinophils, mast cells, basophils and IL-9⁺, IL-17⁺ and IFN- γ ⁺ CD4⁺ T cells in BAL and mediastinal and bronchial lymph node of SARS-CoV-2-infected ACE2.Tg mice (Supplementary Fig. 1b; Fig. 2f–h). Lung histology indicated that combinatorial treatment of SO dose of anti-IL-9 and RDV reduced immune cells infiltration, mucus production and mast cell accumulation (Supplementary Fig. 6a, b), indicating that anti-IL-9 antibody and RDV treatment synergistically controlled SARS-CoV-2 infection. Altogether, we demonstrated that IL-9 regulating anti-viral response while promoting airway inflammation contributes to SARS-CoV-2 infection.

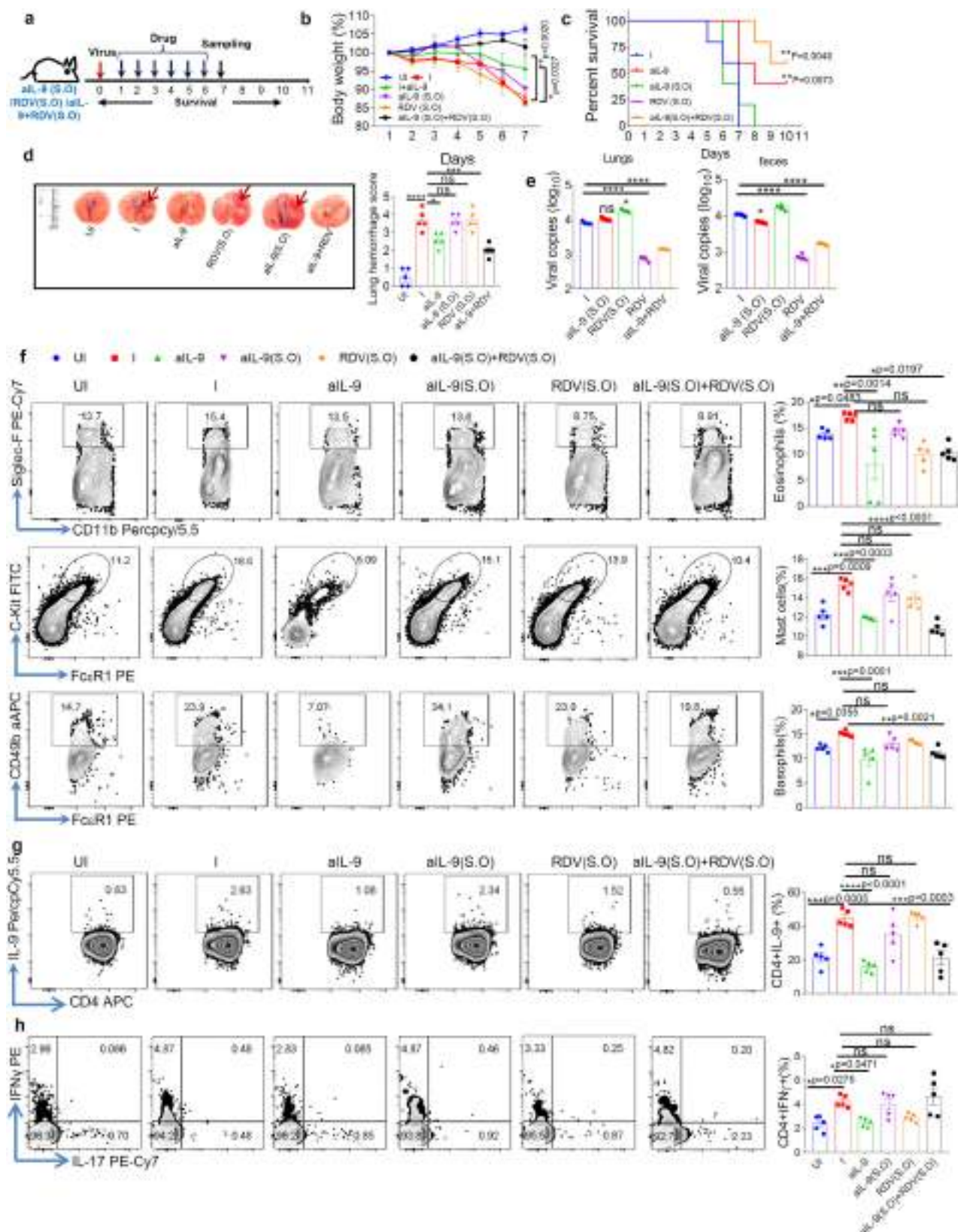
Foxo1-inhibition attenuates lung inflammation and SARS-CoV-2 infection

We previously showed that *Foxo1* is essential for IL-9 induction and Th9 cell differentiation¹⁸. We observed that *Foxo1* and IL-9 expression is increased in active human Covid19 patients, and in the lungs of SARS-CoV-2-infected hamster and ACE2.Tg mice (Fig. 3a–d; Supplementary Fig. 7a), suggesting that *Foxo1*-IL-9 axis might be critical for SARS-CoV-2 infection and lung inflammation. To test the effect of *Foxo1* in SARS-CoV-2 infection, we blocked *Foxo1* using pharmacological inhibitor (Foxo1i), AS184285, as indicated (Fig. 3e). Foxo1i inhibited *Foxo1*, *Pu.1* expression (Supplementary Fig. 7b) and restored weight loss with increased survival, decreased lung lesions and haemorrhage score, and decreased lung viral load of SARS-CoV-2-infected ACE2.Tg mice (Fig. 3f–h; Supplementary Fig. 7c, d). Foxo1i treatment found to be as good as RDV treatment in controlling SARS-CoV-2 infection (Fig. 3f–h). Lung histology indicated that Foxo1i as effective as RDV treatment in suppressing immune cell infiltration, collagen accumulation, mucus overproduction, and mast cell accumulation (Supplementary Fig. 7e). In line with this, Foxo1i, as compared to control, treatment reduced the frequency of eosinophils, mast cells, basophils and CD4⁺IL-9⁺, CD4⁺IL-4⁺ T cells, and IL-9 levels in BAL (Fig. 3i–n; Supplementary Fig. 7f), and suppressed Th9 cells-associated transcription factors, *IRF4*, *Batf*, *Smad3* (Fig. 3o), in SARS-CoV-2-infected ACE2.Tg mice. Similar to IL-9 neutralization, Foxo1i suppressed the expression *Cxcl10*, *Ccl2*, *Fcer1* in the lungs of SARS-CoV-2-infected ACE2.Tg mice (Supplementary Fig. 7g).

We further tested type 1 IFNs and ISGs expression to understand enhanced anti-viral activity upon *Foxo1* inhibition. We found that *Foxo1* inhibition, as compared to control, enhanced the expression of IRFs (*Irf3*, *Irf7*, *Irf9*), ISGs (*Iftm*, *Irfn- α* , *Irfn- β* , *Irfn- γ* , *Irfn- δ*), anti-viral genes (*Oas1g*, *Oas2*, *Oas3*, *Rnase-L*, *Adar*, *cgas* and *Sting*) (Fig. 3p–r; Supplementary Fig. 7h, i). These results suggest that *Foxo1* inhibition suppressed SARS-CoV-2 infection and airway inflammation via anti-viral pathways and IL-9, respectively. *Foxo1* exacerbates SARS-CoV-2 infection by *Foxo1*-dependent gene expression in SARS-CoV-2 infection.

To further confirm our findings that *Foxo1*-dependent IL-9 promotes SARS-CoV-2 infection and airway inflammation, we conditionally deleted *Foxo1* in CD4⁺ T cells in ACE2.Tg mice, and hereafter we refer these mice as *Foxo1*^{fl/fl}.CD4^{Cre+} while *Foxo1*^{fl/fl}.CD4^{Cre-} x ACE2.Tg mice referred as *Foxo1*^{fl/fl}.CD4^{Cre-} mice. We demonstrated that *Foxo1*^{fl/fl}.CD4^{Cre+}, as compared to *Foxo1*^{fl/fl}.CD4^{Cre-} mice were found to be less sensitive to SARS-CoV-2 infection, remained healthy with no sign of weight loss, and survived infection better than RDV treatment without substantial lung lesions and lung viral load (Supplementary video 1a, b; Fig. 4a–d; Supplementary Fig. 8a). Lung histology and immunophenotyping of BAL indicated that *Foxo1*^{fl/fl}.CD4^{Cre+}, as compared to *Foxo1*^{fl/fl}.CD4^{Cre-} mice infected with SARS-CoV-2 showed reduced frequency of eosinophils, basophils, mast cells and IL-9⁺, IL-4⁺ CD4⁺ T cells in the BAL and lower immune cell infiltration, mucus production, and mast cell accumulation in lung tissues (Fig. 4e, f; Supplementary Fig. 8b–e). Similarly, the expression of *IL4*, *IL5*, *IL13*, and *Irfn- γ* Th9 cell-associated genes *IL9*, *Gata3*, *Batf* and *Pu.1* was found to be decreased in *Foxo1*^{fl/fl}.CD4^{Cre+} mice, as compared to *Foxo1*^{fl/fl}.CD4^{Cre-} mice (Supplementary Fig. 9a–c).

To understand the resistant phenotype of *Foxo1*^{fl/fl}.CD4^{Cre+} mice to SARS-CoV-2 infection, RNA sequencing (RNAseq) was performed. Principal component analysis (PCA) indicated a distinct gene profile between uninfected, SARS-CoV-2-infected *Foxo1*^{fl/fl}.CD4^{Cre-} and *Foxo1*^{fl/fl}.CD4^{Cre+} mice (Supplementary Fig. 9d). Volcano plot represents differentially expressed genes between SARS-CoV-2-infected lungs of *Foxo1*^{fl/fl}.CD4^{Cre+} and *Foxo1*^{fl/fl}.CD4^{Cre-} mice (Supplementary Fig. 9e). Differential gene analysis indicated that, 1517, 1511 genes were upregulated and 1377, 1657 genes were downregulated in *Foxo1*^{fl/fl}.CD4^{Cre-}, *Foxo1*^{fl/fl}.CD4^{Cre+} infected mice, respectively with respect to uninfected hACE2.Tg mice (Supplementary Fig. 9f). We selected top 100 differentially expressed genes between *Foxo1*^{fl/fl}.CD4^{Cre-} and *Foxo1*^{fl/fl}.CD4^{Cre+} mice, and identified the top 10 pathways, which were differentially regulated between SARS-CoV-2-infected lungs of *Foxo1*^{fl/fl}.CD4^{Cre+} and *Foxo1*^{fl/fl}.CD4^{Cre-} mice (Supplementary Fig. 9g). Pathways that are critical for anti-viral function including type 1 IFN, downregulation of chemokine receptor and mitogen-activated protein kinase (MAPK) activity, were differentially induced in SARS-CoV-2 infected lungs of *Foxo1*^{fl/fl}.CD4^{Cre+} and *Foxo1*^{fl/fl}.CD4^{Cre-} mice (Supplementary Fig. 9f), indicating that *Foxo1* controls anti-viral pathways in SARS-CoV-2 infection. Among top 100 differentially modulated genes, we found that *Daxx* (Death domain associated protein), NOD-like receptor family CARD domain containing 5 (*Nlr5*), Serine/threonine-protein kinase PAK 2 (*Pak2*), Chemokine (C motif) ligand (*Xcl1*), *Oas2*, *Oas1g*, which were known to suppress SARS-CoV-2 infection^{32–34}, were upregulated in SARS-CoV-2-infected lungs of *Foxo1*^{fl/fl}.CD4^{Cre+} mice, as compared to *Foxo1*^{fl/fl}.CD4^{Cre-} mice (Fig. 4g).



RNAseq Data identified the downregulation of *Plaa* (Phospholipase A2-Activating protein)³⁵, Neural precursor cell-expressed developmentally downregulated 9 (*Nedd9*)³⁶, Protein Phosphatase 6 Regulatory Subunit 2 (*ppp6r2*)³⁷, *Slc35a3* (Human protein atlas; www.proteinatlas.org), *Serpina3m*³⁸ which are known to be associated with lung injury, lung cancer, allergic inflammation, fibroblast formation

genes, and asthma in the lungs of SARS-CoV-2-infected lungs of *Foxo1^{fl/fl}.CD4^{Cre+}* mice as compared to *Foxo1^{fl/fl}.CD4^{Cre-}* (Fig. 4h–j). String analysis was performed on the differentially expressed genes between *Foxo1^{fl/fl}.CD4^{Cre-}* and *Foxo1^{fl/fl}.CD4^{Cre+}* mice to identify the network of genes that are either upregulated or downregulated in *Foxo1^{fl/fl}.CD4^{Cre+}* mice. String analysis indicated *Nlr3c1*, *Irf2*, Runt-related transcription

Fig. 2 | Synergistic effect of anti-IL-9 antibody treatment with RDV in SARS-CoV-2 infection. **a** Experimental design where anti-IL-9 and RDV treatment was given as indicated (Created with BioRender.com). **b, c** Change in body weight (two-way ANOVA followed by Tukey's test) and percent survival determined by Mantel–Cox test post SARS-CoV-2 infection and treatment ($n = 5$); * $p < 0.05$, ** $p < 0.005$; bar graph represents as a mean \pm SEM. **d** Lung haemorrhage score at 7 dpi on a scale of 0–5, 0 is a normal pink healthy lung, and 5 is a diffusely discoloured dark red lung; bar graph represents as a mean \pm SEM ($n = 5$ mice per group) (one-way ANOVA followed by Tukey's multiple comparison test) *** $p < 0.0005$, **** $p < 0.0001$, ns = non-significant; arrow represents dark red lung lesions. **e** Viral load in SARS-CoV-2-infected ACE2.Tg mice lung tissue after therapeutic treatment

($n = 5$ mice), and freshly collected faeces qPCR assays ($n = 5$ mice per group). * $p = 0.0021$, *** $p = 0.0367$, **** $p < 0.0001$; one-way ANOVA followed by Tukey's multiple comparison test; bar graph represents as a mean \pm SEM. **f** Representative FACS dot plots show frequency of eosinophils, mast cells, and basophils. Bar graph represents as a mean \pm SEM ($n = 5$ mice per group) (one-way ANOVA followed by Tukey's multiple comparison test). **g, h** Intracellular cytokine staining of IL-9, IFN- γ and IL-17 on CD4 $^{+}$ T cells ($n = 5$); bar graph represents as a mean \pm SEM; one-way ANOVA followed by Tukey's multiple comparison test. **g** *** $p < 0.0005$, **** $p < 0.0001$, **h** * $p < 0.05$, ns = non-significant Source data are provided as a Source data file.

factor 3 (*Runx3*), among other transcription factors were upregulated while *Smad3*, *Smad7*, peroxisome proliferator-activated receptor (*Ppara*) were downregulated in Foxo1 $^{fl/fl}$.CD4 $^{Cre+}$, as compared to Foxo1 $^{fl/fl}$.CD4 $^{Cre-}$ mice, and have a direct interaction with *Foxo1* (Supplementary Fig. 9i, j). While *Nlr3c1* and *Irf2* negatively regulate anti-viral functions^{39,40}, *Runx3* positively regulated Th1 cells and suppresses Th9 cells development^{10,41} may contribute to anti-SARS-CoV-2 activity. Collectively, RNAseq Data show a distinct gene expression associated with anti-viral, immune regulation, IL-9 induction, asthma and lung injury, may make Foxo1 $^{fl/fl}$.CD4 $^{Cre+}$ mice resistant to SARS-CoV-2 infection. Moreover, Foxo1 $^{fl/fl}$.CD4 $^{Cre+}$, as compared to Foxo1 $^{fl/fl}$.CD4 $^{Cre-}$ mice show an increased expression of ISGs (*Iflna*, *Ifnb*, *Irf1*, *Irf3*, *Iftm*, *Sting*) and anti-viral genes (*Oas1g*, *Oas2*, *Oas3*, *Rnase l*) in SARS-CoV-2 infected lungs (Supplementary Fig 10a, b). These Data indicate that Foxo1 promotes viral infection and associated pathology through IL-9 and suppressing anti-viral functions.

Foxo1-IL-9 axis is essential for SARS-CoV2 transmission

Our data indicated Foxo1 linked to SARS-CoV-2 infection and regulate viral replication and shedding, raising a possibility that Foxo1 may control viral transmission. To understand this, SARS-CoV-2-infected ACE2.Tg and Foxo1 $^{fl/fl}$.CD4 $^{Cre+}$ mice were cohoused at 1:1 ratio with uninfected ACE2.Tg mice for 10–12 days followed by measuring various parameters of infections (Fig. 5a). As compared to uninfected ACE2.Tg mice, uninfected ACE2.Tg mice cohoused with SARS-CoV-2-infected ACE2.Tg mice develop infection while uninfected ACE2.Tg mice cohoused with SARS-CoV-2-infected Foxo1 $^{fl/fl}$.CD4 $^{Cre+}$ mice develop low level of infection as indicated by weight loss, lung lesions, viral load and histological score (Fig. 5b–f). In addition, we tested whether ACE2.Tg and Foxo1 $^{fl/fl}$.CD4 $^{Cre+}$ mice can transmit SARS-CoV-2 infection to healthy cohoused ACE2.Tg mice. Our previous data, indicate that Foxo1 $^{fl/fl}$.CD4 $^{Cre+}$, as compared to Foxo1 $^{fl/fl}$.CD4 $^{Cre-}$ mice are less sensitive to SARS-CoV-2 infection (Fig. 4a, b). This could be due to lesser viral replication in Foxo1 $^{fl/fl}$.CD4 $^{Cre+}$ mice. Keeping this in mind, we cohoused SARS-CoV2-Foxo1 $^{fl/fl}$.CD4 $^{Cre+}$ mice with healthy ACE2.Tg mice for a longer period (12-day post infection) to see whether additional period allows an efficient transmission of SARS-CoV-2 to healthy cohoused ACE2.Tg mice as it does in case of infected ACE2.Tg mice cohoused with healthy ACE2.Tg mice. Even though, longer period of cohousing of SARS-CoV-2 infected Foxo1 $^{fl/fl}$.CD4 $^{Cre+}$ mice were unable to transmit SARS-CoV-2 infection, indicating the inability Foxo1 $^{fl/fl}$.CD4 $^{Cre+}$ to transmit the infection (Supplementary Fig. 12). As compared Foxo1 $^{fl/fl}$.CD4 $^{Cre+}$ cohoused with ACE2.Tg, ACE2.Tg cohoused ACE2.Tg mice, showed higher frequency of eosinophils and mast cells in their BAL (Fig. 5g, h). These Data together indicated *Foxo1* limits viral transmission.

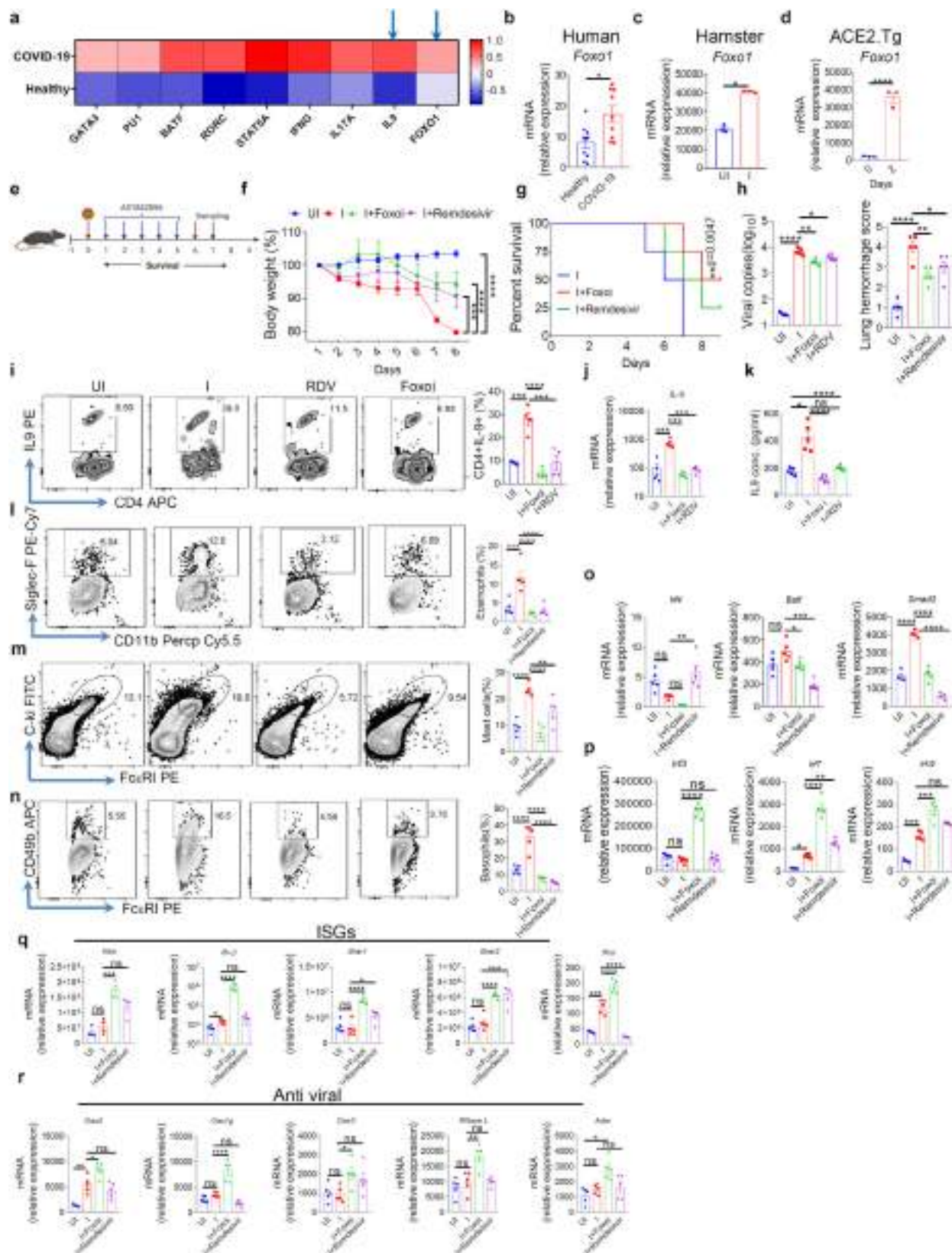
Foxo1 $^{fl/fl}$.CD4 $^{Cre+}$ mice were resistant to SARS-CoV-2 infection and associated mortality. Foxo1-mediated IL-9 causes severity of SARS-CoV-2 infection. We tested whether exogenous IL-9 makes Foxo1 $^{fl/fl}$.CD4 $^{Cre+}$ mice susceptible to SARS-CoV-2 infection. Intranasal administration of exogenous IL-9 makes Foxo1 $^{fl/fl}$.CD4 $^{Cre+}$ mice susceptible to SARS-CoV-2 infection as their overall physical activity declined (Supplementary video 2a, b). In line with this, exogenous IL-9 treatment of

Foxo1 $^{fl/fl}$.CD4 $^{Cre+}$, as compared to Foxo1 $^{fl/fl}$.CD4 $^{Cre+}$ mice without IL-9 treatment, mice show weight loss, increased lung lesions, viral load with and increased frequency of eosinophils, mast cells and IL-4 $^{+}$, IL-9 $^{+}$ and IL-17 $^{+}$ -producing CD4 $^{+}$ T cells (Fig. 5i–n; Supplementary Fig. 11a). In line with this, IL-9 treatment to Foxo1 $^{fl/fl}$.CD4 $^{Cre+}$ mice increased histological score as determined by various indicated changes (Fig. 5o, p). These data indicated that replenishing IL-9 in Foxo1 $^{fl/fl}$.CD4 $^{Cre+}$ mice makes these mice susceptible to SARS-CoV-2 infection. However, endogenous (cellular) source of IL-9 in this case was remained unclear. Since it was shown that IL-9 is primarily produced by CD4 $^{+}$ cells and innate lymphoid cells (ILCs)⁴², we tested the cellular source of IL-9 in SARS-CoV2 infection in ACE2.Tg mice. We tested IL-9 cytokine staining in CD4 $^{+}$ T cell, NK cells and ILCs from uninfected and SARS-CoV-2 infected ACE2.Tg mice. Our data suggest the IL-9 is primarily produced by CD4 $^{+}$ T cells; we did not find IL-9 production from NK cells and ILCs (Supplementary Fig. 13a–d).

We further tested whether CD4 $^{+}$ T cell-driven IL-9 is sufficient in making Foxo1 $^{fl/fl}$.CD4 $^{Cre+}$ mice susceptible to SARS-CoV-2 infection. To do this, we transferred the wt CD4 $^{+}$ T cells from ROSA mTmG mice into the Foxo1 $^{fl/fl}$.CD4 $^{Cre+}$ mice; we referred these mice as wt-CD4T-Foxo1 $^{fl/fl}$.CD4 $^{Cre+}$ mice. The advantage of using CD4 $^{+}$ T cells from ROSA mTmG mice, as these CD4 $^{+}$ T cells can be tracked in vivo based on their expression of RFP (Red fluorescence protein). Post transferring of CD4 $^{+}$ T cells from ROSA mTmG mice, we infected wt-CD4T-Foxo1 $^{fl/fl}$.CD4 $^{Cre+}$ and Foxo1 $^{fl/fl}$.CD4 $^{Cre+}$ mice with SARS-CoV-2 ancestral strain of SARS-CoV-2. We found that wt-CD4T-Foxo1 $^{fl/fl}$.CD4 $^{Cre+}$ mice become as susceptible as wt ACE2.Tg mice while Foxo1 $^{fl/fl}$.CD4 $^{Cre+}$ mice were found to be remain resistant to SARS-CoV-2 infection (Supplementary Fig. 13e). BALF analysis suggests that IL-9 is produced from wt mTmG, but not from Foxo1-deficient, CD4 $^{+}$ T cells, further confirming our findings that CD4 $^{+}$ T cell-derived IL-9 contributes to the susceptibility of SARS-CoV-2 infection (Supplementary Fig. 13f–h). Taken together, our Data demonstrate that IL-9 promote SARS-CoV-2 infection, and make in Foxo1 $^{fl/fl}$.CD4 $^{Cre+}$ mice susceptible to infection. Altogether, we identified one of the key mechanisms of T cell-mediated immunopathology in Covid19 by showing that *Foxo1* and IL-9 controls two distinctive pathological features that critically contribute to the progression and severity of COVID-19—namely anti-viral pathway and airway inflammation. The role of T cells was identified in mounting anti-SARS-CoV-2 response⁴³. However, an Involvement of CD4 $^{+}$ T cells was not identified in promoting airway inflammation in promoting primary SARS-COV-2 infection.

Discussion

In this study, we identified one of the key mechanisms of T cell-mediated immunopathology in Covid19. We show that *Foxo1*-IL-9 axis controls two distinctive pathological features that critically contribute to the progression and severity of COVID-19 - namely anti-viral pathway and airway inflammation. Although the involvement of adaptive immune cells, particularly CD4 $^{+}$ and CD8 $^{+}$ T cells, was identified in mounting protection in primary SARS-CoV-2 infection⁴³, the role of CD4 $^{+}$ T cells and its cytokines were not known in regulation of anti-viral response and airway inflammation in SARS-COV-2 infection.



We identified an association of IL-9, a cytokine primarily produced by Th⁺ cells, in enhancing the severity of SARS-CoV-2 infection. Naïve CD4⁺ cells differentiate into IL-9-producing Th9 cell in the presence of TGF- β and IL-4. Although the role of IL-9 and IL-9R was well documented in allergic inflammation and atopy, their functions in respiratory viral illness were not clearly understood. IL-9 was found to be

present in bronchial secretion of respiratory syncytial virus (RSV) infected infants⁴⁴. Moreover, IL-9 was found to regulate RSV-induced immunopathology and enhance RSV infection, as depletion of IL-9 promoted RSV clearances from the lungs⁴⁵. In line with this, we show that IL-9 was found to be increased in active COVID-19 patients. Similarly, IL-9 was found to be upregulated in SARS-CoV2-infected hamster

Fig. 3 | Foxo1 inhibition attenuates lung inflammation and SARS-CoV-2 infection. **a** Heat map of gene expression of COVID-19 active patients or healthy control ($n = 9$). Gene expression levels in the heat map are z score-normalized values determined from log2 transformed relative gene expression. *Foxo1* (Human; $n = 9$) (**b**), Hamster ($n = 3$ hamster per group) (**c**), and mice ($n = 3$ mice per group) at day 2 (**d**) is represented in the form of a bar graph ($*p < 0.05$, $****p < 0.0001$; student's t-test); bar graph represents as a mean \pm SEM. **e** Pictorial diagram shows the experimental design of the study (Created with BioRender.com). **f** Percentage change in the body weight ($n = 5$ mice per group) ($***p < 0.002$, $****p < 0.0001$; two-way ANOVA followed by Tukey's test); bar graph represents as a mean \pm SEM. **g** Percent survival of each group analysed by Mantel–Cox test ($**p < 0.0047$, $n = 5$); bar represents as a mean \pm SEM. **h** Relative lung viral load by qPCR assay and Lung haemorrhage scored on 7 dpi ($*p < 0.05$, $**p < 0.0047$, $****p < 0.0001$); bar graph represents as a mean \pm SEM ($n = 5$ mice per group); (one-way ANOVA followed by

Tukey's multiple comparison test). **i–k** Left panel: Intracellular staining of IL-9 was performed ($n = 4$) in BAL cells; middle panel (**j**) shows relative mRNA expression of *Il9* and right panel (**k**) shows the IL-9 concentration in BAL fluid by ELISA ($n = 5$), $*P < 0.05$, $***P < 0.0004$, $p < 0.0001$ (right: Kruskal–Wallis test, left and middle: two-way ANOVA). **l–n** FACS plots and their respective bar graphs represent Eosinophils, Mast cells, and Basophils percentages in BALF. $*p = 0.0471$, $**p < 0.005$, $***p = 0.0002$, $****p < 0.0001$ (one-way ANOVA followed by Tukey's multiple comparison test) $n = 5$. **o, p** relative mRNA expression of *Irf4*, *Batf*, *Smad3*, *Irf3*, *Irf7*, and *Irf9* ($*p = 0.0406$, $**p = 0.0060$, $***p = 0.0003$, $****p < 0.0001$; one-way ANOVA). **q, r** relative mRNA expression of ISGs (*Iftm*, *Irfn3*, *Irfn1*, *Irfn2*, *Irfn4*) and anti-viral factors genes (*Oas2*, *Oas3*, *Oas1g*, *RNaseL*, and *Adar*) profile by qPCR from lung samples ($n = 4$); $*p < 0.05$, $**p < 0.005$, $***p < 0.005$, $****p < 0.0001$ (one-way ANOVA followed by Tukey's, multiple comparison test); bar graph represents as a mean \pm SEM. Source data are provided as a Source data file.

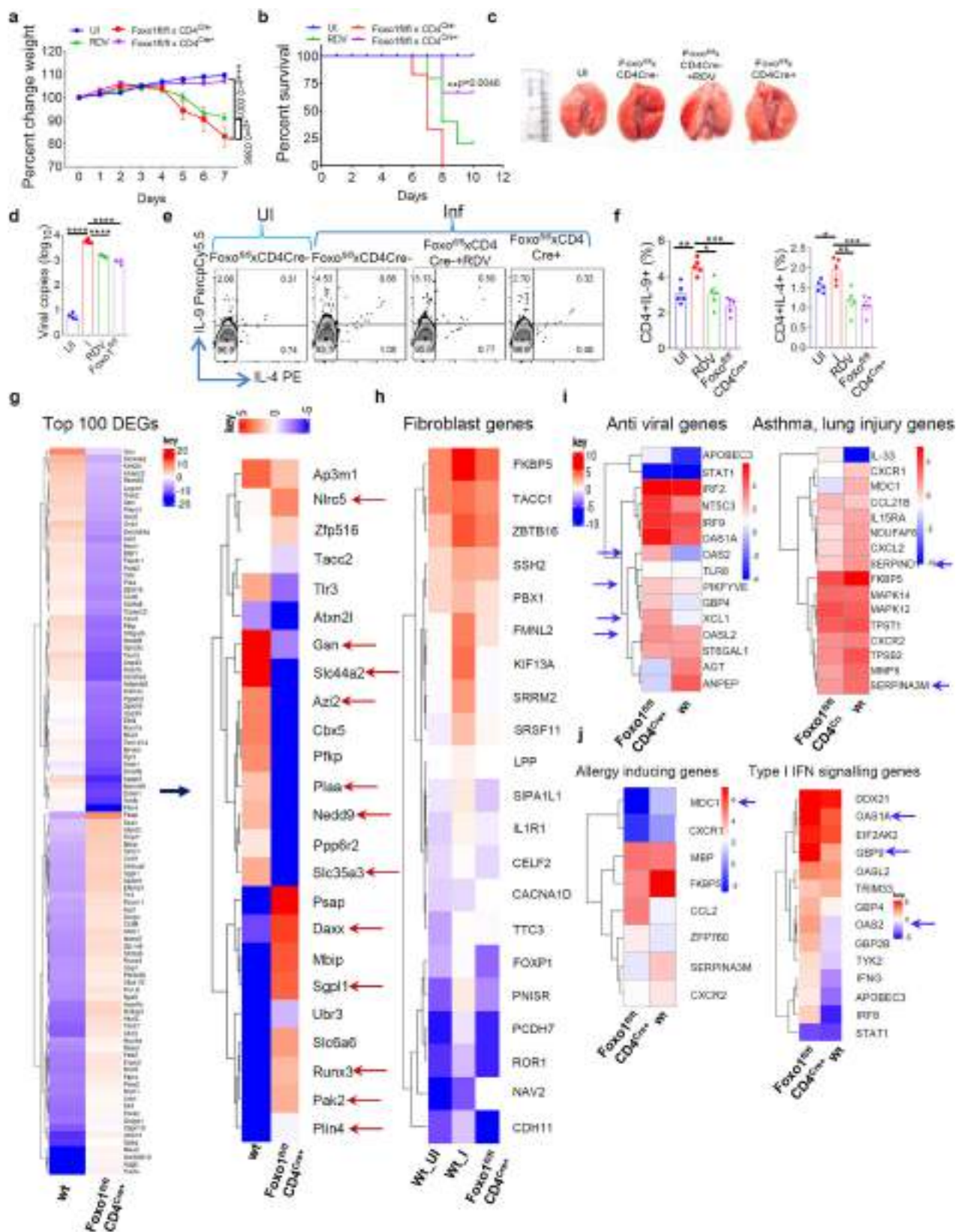
and ACE2.Tg mice. Our data demonstrated that the depletion of IL-9 enhances viral clearance while regulates SARS-CoV-2-induced airway inflammation and lung pathology. We further characterised the role of IL-9 in SARS-CoV-2 infection and associated pathologies in ACE2.Tg mice. Our data suggested that IL-9 was found to be increased in early days of SARS-CoV-2 infection in hamster, which further indicated the involvement of IL-9 in the induction of airway inflammation. In line with this, we found that the expression of IL-9 was found to be increased in the PBMCs of active COVID-19 patients.

Role of IL-9 in inducing airway inflammation and immunopathology is well characterized, as it was shown to greatly enhance infiltration of lymphocytes, eosinophils and associated with mast cells hyperplasia and mucus production⁴⁶. It was previously shown that anti-IL-9 neutralization markedly decreased allergic inflammation associated with reduced levels of total serum IgE, eosinophil frequency, mucus production and overall histopathological score^{47,48}. In line with this, our data demonstrated that anti-IL-9 neutralization in SARS-CoV-2 infection reduced overall of histopathological score associated with the reduction in mucus production, collagen deposition and mast cell accumulation in the lungs. In line with this, exogenous treatment of IL-9 enhanced overall histopathological score in SARS-CoV-2 infection with an increased in eosinophils, mast cell accumulation and mucus production in the lungs. Taken together, our data indicated a crosstalk between IL-9 and mast cell in SARS-CoV-2 infection, which is consistent with the previous findings that IL-9 promotes mastocytosis and mast cell functions by enhancing their survival^{49,50}. Although our data suggest that IL-9 enhances the severity of the SARS-CoV2 infections, mutations in the spike protein of SARS-CoV2 affect its infectivity and antigenicity. Mutation in the multi-basic cleavage site (PRRAR) at the spike protein S1/S2 interface is a major determinant of infectivity and pathogenesis of SARS-CoV2 and its variants, as it allows the efficient cleavage of S protein by the host proteases, which is a prerequisite for efficient virus entry and fusion^{51,52}. The mutation of Proline (P) to Histidine (H) P681H in the cleavage site as seen in Alpha and Omicron variants has been suggested to reduce the viral infectivity as compared to the Delta virus in which the introduction of additional basic residue P681R might be responsible for the enhancement of pathogenesis^{53,54}. However, except for the Proline mutation, the cleavage site is found to be highly conserved in SARS-CoV-2 variants, and mutation of the polybasic arginine residue might result in the development of low virulent strains and infection might restrict the localized spread as compared to systemic spread as shown in Influenza viruses^{55,56}. In addition, mutations in other than the spike protein like D614G, N501Y, and L452R were found to be associated with viral infectivity and antigenicity. However, we did not find these mutations in the viral stocks, we used in our study.

Our data suggested that IL-9-producing Th9 cells contribute to the progression of SARS-CoV2 infection and associated airway inflammation. However, IL-9 was also found to be produced by ILCs⁴²,

indicating a possibility of ILCs, in addition to Th9 cells, in contributing to SARS-CoV2 infection and associated lung inflammation. We tested the role of ILCs-mediated IL-9 production in SARS-CoV-2 infection in ACE2.Tg mice. Our data indicated that neither NK cells nor ILCs contribute to IL-9 production in the lungs of SARS-CoV2 infected mice. We previously identified that *Foxo1* is one of the key transcription factors that is essential for the induction of IL-9 in Th cells¹⁸. Hence *Foxo1* deletion may lead to the attenuation of IL-9-mediated SARS-CoV2 infection and associated lung inflammation. In line with this, our data demonstrated that *Foxo1* deficiency in CD4⁺ T cells leads to blunted IL-9 production, which makes these mice less susceptible to SARS-CoV-2 infection and associated airway inflammation. Interestingly either exogenous IL-9 or transfer of *Foxo1*-sufficient CD4⁺ T cells make *Foxo1*-deficient mice susceptible to SARS-CoV2 infection and associated inflammation further indicating the role of *Foxo1* in CD4⁺ T cell-derived IL-9 in driving airway inflammation in this model.

Although IL-9-mediated regulation of anti-viral function was shown in RSV infection⁴⁵, the mechanism by which IL-9 regulates antiviral functions was not identified. It was documented that anti-viral genes and ISGs were found to be essential for the clearance of SARS-CoV-2 infection. In line with this, our data suggest that IL-9 suppresses the expression of anti-viral genes and ISGs, which could be responsible for an increased severity of SARS-CoV-2 infection in the presence of IL-9. Although there is no clear mechanism is identified as to how IL-9-meidates suppression of type 1 IFN response. Our data indicated that while anti-IL-9 antibody neutralization suppressed SARS-CoV-2 infection and increased anti-viral type 1 IFN response, exogenous recombinant IL-9 treatment enhanced SARS-CoV-2 infection and suppressed anti-viral type 1 IFN response. Upon binding to its receptor, IL-9 activates proximal signalling events primarily driven by JAK-STAT pathways, which includes *Jak1*, *Jak3* and *Stat1*, *Stat3* and *Stat5*⁵⁷. Anti-viral response of type 1 IFNs also requires activation of STAT proteins. It was shown that *Stat3* negatively regulates type 1 IFNs response, as *Stat3* deficient cells produced enhanced type 1 IFNs, which in turn increased ISGs expression⁵⁸. Since IL-9 activates *Stat3*, it might suppress type 1 IFNs production and function and subsequently ISGs expression. This is could be one of the potential mechanisms by which IL-9 may suppress type 1 IFNs response. However, this needs to be experimentally evaluated and validated. Our data suggested that increased type 1 response together with anti-viral therapy might provide alternate therapy, as anti-IL-9 antibody with anti-viral drug, RDV, reduce both viral load and lung immunopathology. In fact, suboptimal doses of anti-IL-9 and RDV synergistically eliminate SARS-CoV-2 infection and reduce lung pathologies and inflammation. *Foxo1* is essential for the induction of IL-9 in Th9 cell, and other Th cell subsets¹⁸. *Foxo1* blockade reduces allergic inflammation in asthma due to reduction in IL-9 production in the lungs¹⁸. In line with this, our data show that *Foxo1* inhibition using pharmacological inhibitor leads to suppress SARS-CoV-2 infection and associated immunopathology. Consistently, we demonstrated that



Foxo1-conditional deficiency in CD4⁺ T cells make ACE2.Tg mice resistant to SARS-CoV-2 infection associated with the blunted IL-9 production. Mechanistically, similar to IL-9 neutralization, *Foxo1* deficiency in CD4⁺ T cells leads to the upregulation of anti-viral and ISGs. This could be due to the *Foxo1*-dependent regulation of anti-viral function by promoting *Irf3* degradation⁵⁹. Importantly, both IL-9

neutralization and *Foxo1* conditional deficiency in ACE2.Tg mice generate a similar phenotype in terms of immunopathology in SARS-CoV-2 infection associated with the accumulation of eosinophils, mast cells in the lungs and other related pathologies. Taken together, our data demonstrated that *Foxo1*-IL-9 axis regulates SARS-CoV-2 infection and associated immunopathology.

Fig. 4 | Foxo1 exacerbates SARS-CoV-2 infection by Foxo1-dependent gene expression in SARS-CoV-2 infection. hACE2.Tg (wt), Foxo^{fl/fl}.CD4^{Cre} × hACE2.Tg (RDV group as a control) was intranasally challenged with SARS-CoV-2 and euthanized at 7 dpi. **a** Percentage changes in body Weight ($n = 5$; two-way ANOVA followed by Tukey's multiple comparison test; $^*p = 0.0366$, $^{***}p = 0.0001$; bar graph represents as a mean \pm SEM. **b** Percent survival by Mantel–Cox test ($^{***}p = 0.0095$). **c** Image shows gross lung morphological changes **d** Relative viral load was measured by qPCR ($^{****}p < 0.0001$); bar graph represents as a mean \pm SEM ($n = 4$ mice per group); one-way ANOVA followed by Tukey's multiple comparison test. **e**, **f** BALF cells were stimulated with PMA/Ionomycin and IL-9, IL-4 production was determined by flow cytometry ($^*p < 0.05$, $^{**}p < 0.005$, $^{***}p < 0.0001$; $n = 5$) (one-way

ANOVA followed by Tukey's multiple comparison test); bar graph represents as a mean \pm SEM. **g–j** Heat maps of significantly up and downregulated genes during SARS-CoV-2 infection. **g** Heat map of all significantly differentially expressed top 100 genes DEGs (differentially expressed genes) and further heat-map analysis of selected top significantly differentially expressed genes. **h** Fibroblast genes **i** anti-viral & asthma, lung injury genes in SARS-CoV-2, **j** allergy, Type I IFN signalling genes identified through DEG analysis. Genes shown in each pathway are the union of the differentially expressed genes from Wt (hACE2.Tg) Vs. Foxo^{fl/fl}.CD4^{Cre} comparisons. Columns represent samples, and rows represent genes. Gene expression levels in the heat maps are z score-normalized values determined from log2 values. Source data are provided as a Source data file and RNA seq data available at NCBI.

Methods

Animals

All the experiments were performed at infectious disease research facility (IDRF) in BSL-3 and ABSL-3 as per IBSC (Institutional Biosafety Committee) guidelines. All experimental procedures involving virus challenge were approved by the Institutional Animal Ethics Committee (IAEC), IBSC and RCGM as per the guidelines of THSTI (IAEC/THSTI/191) and Department of Biotechnology, Govt. of India. Heterozygous K18-hACE2.Tg mice c57BL/6J mice (strain: 2B6.Cg-Tg(K18-ACE2)2PrImn/J), Foxo1^{fl/fl} × CD4^{Cre} (Foxo1^{fl/fl}; strain#024756; CD4Cre strain: 017336) and mTmG mice (B6.129(Cg)-Gt(Rosa)26Sortm4(ACTB-tdTomato,-EGFP)Luo/J; strain #007676) were procured from The Jackson Laboratory. Golden Syrian hamsters were procured from CDRI (Central Drug Research Institute). hACE2.Tg mice were crossed with the Foxo1^{fl/fl}.CD4^{Cre} mice to generate Foxo1^{fl/fl}.CD4^{Cre} × ACE2.Tg mice. Animals were housed and maintained at THSTI-SAF (small animal facility). All the mice were fed with a standard chow diet (Cat.no 1324p, Altromin; Germany), water and libitum. The temperature for mice rooms were maintained between -19 – 26 °C with ~ 30 – 70% humidity. Mice were housed with 14 h light/10 h dark cycles.

For the SARS-CoV-2 infection, mice were administered intranasally with 10^3 (Foxoi, Foxo1^{fl/fl}.CD4^{Cre} + IL-9 experiment), 10^5 PFU (α IL-9 and other experiments), 10^4 PFU (B.1.529 \pm IL-9) (50 μ l) of live SARS-CoV-2 under injectable anaesthesia as previously described^{4,60}.

Human ethics

The study was approved by the Institutional Ethics Committee (Human Research) of THSTI and ESIC Hospital, Faridabad (Letter Ref No: THS 1.8.1/(97) dated 07 July 2020). After obtaining an approval from the Institutional Ethics Committee of THSTI (IEC, Human Research) and ESIC Hospital, Faridabad active COVID-19 patients' blood samples were collected from symptomatic COVID-19 patients and healthy participants after the written informed consent and there was no bias to the recruitment or collection. PBMCs were isolated from collected blood samples, and stored in liquid nitrogen as previously described for further use¹⁸. Briefly, human PBMCs were isolated by Ficoll Gradient (GE Healthcare).

SARS-CoV-2 propagation

Vero E6 (CRL-1586; American Type Culture Collection) and Caco2 (A kind gift from Dr. Sweetly Samal) was cultured at 37 °C in Dulbecco's modified Eagle's medium (DMEM) 4.5 g/L D-glucose, 100,000 U/L Penicillin/471 Streptomycin, 100 mg/L sodium pyruvate, 25 mM HEPES and 2% FBS. The isolate of SARS-CoV-2; USA-WA1/2020 and B.1.1.529 (10^4 PFU) was used as a challenge strain As mentioned above^{53,60} at THSTI Infectious Disease Research Facility (Biosafety level 3 facility).

In vivo treatments of RDV, anti-IL-9, Foxoi and exogenous IL-9

All the studies were designed to study therapeutic efficacy as compared to RDV. Therapeutic studies (Neutralisation experiments) were performed to define if drug regimens could affect virus replication and disease progression. 6–8-week-old mice (Male and Female) were used

in this experiment. All treatments were initiated one day prior to infection. Post challenge, uninfected and infected mice were observed till the infected mice lost 20–30% weight and the animals were sacrificed when they became moribund for further validation. In two other experiments, treatment with a vehicle, RDV (25 mg/kg; ip), anti-IL-9 (20 μ g/mice; ip), and Foxo1 inhibitor (20 mg/Kg; i.n.) were given. On appearance of moribund features, animals were euthanized by isoflurane; lungs were scored for haemorrhage (described below). The left lobe was placed in 10% formalin and stored at room temperature until sectioning and histological analysis. Lung sectioning, haematoxylin, eosin staining, and N antigen staining as described below was performed at the Institute of Liver and Biliary Sciences (ILBS) at New Delhi.

We then performed two therapeutic studies to ascertain whether α IL-9 (suboptimal, S.O), RDV (S.O), α IL-9(S.O) + RDV (S.O), and Foxo1 inhibitor alone could affect virus replication or disease progression. In the first study, in randomly allocated groups ($n = 5$; 6–8-week-old mice (male and female)), we compared vehicle, RDV, or Foxo1 inhibitor alone. In another study, S.O of α IL-9 (10 mg/kg) and RDV (S.O) (1.5 mg/kg), α IL-9 (S.O) + RDV (S.O) (10 mg/kg + 1.5 mg/kg respectively) were administered once daily via intraperitoneal injection.

To evaluate the role of IL-9, we used Foxo1^{fl/fl}.CD4^{Cre} mice compared to hACE2.Tg mice infection with rIL-9 i.n. (i.n.; 500 ng/mice; 6–8-week-old mice (male and female) were used in this experiment.). Euthanasia and immunopathological assays were performed as described above.

Cohousing and viral transmission

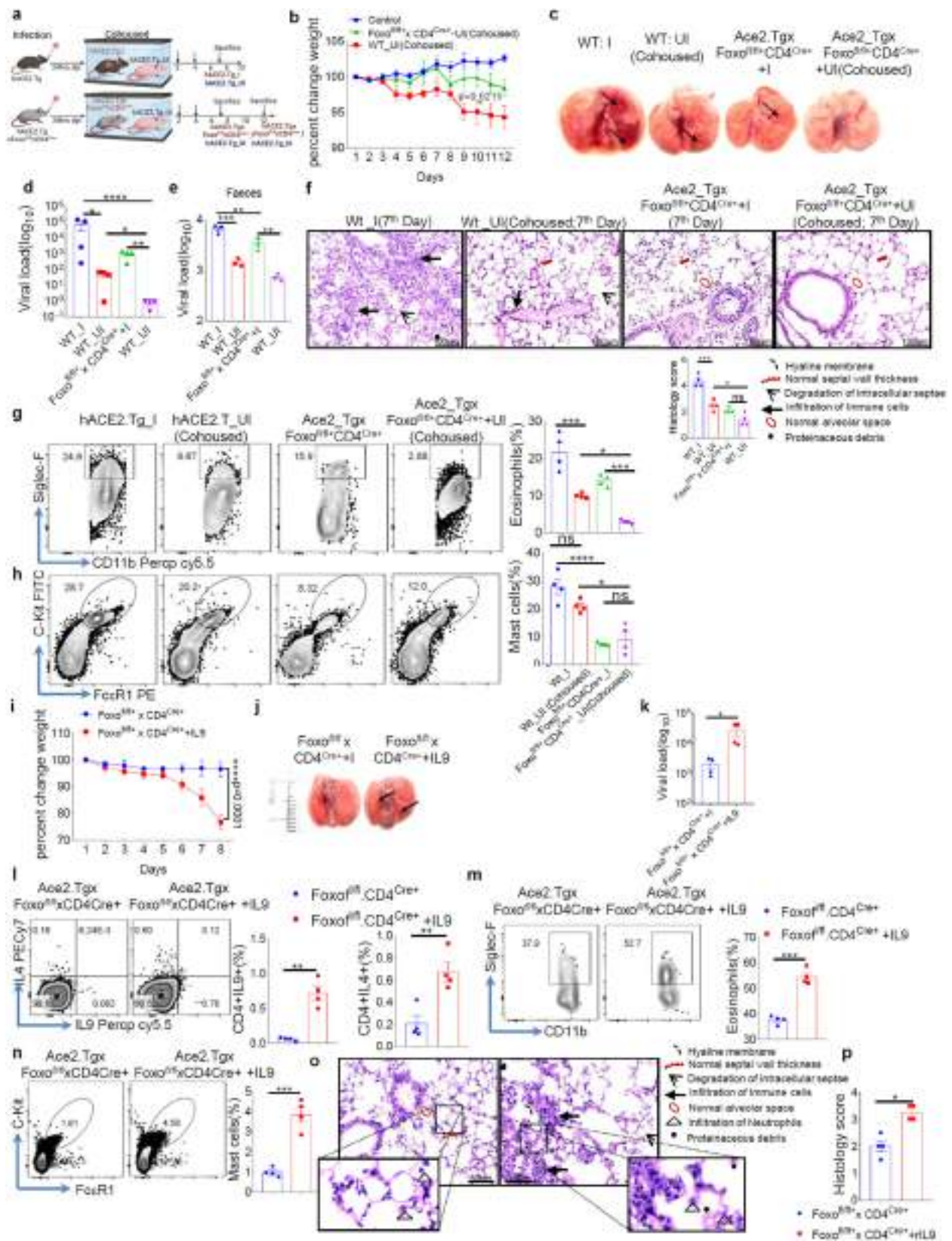
hACE2.Tg mice (6–8 weeks male and female) and Foxo1^{fl/fl}.CD4^{Cre} × ACE2.Tg (6–8 weeks male and female) mice were infected with the with SARS-CoV-2. 24 h post infection, infected mice were cohoused with the uninfected ACE2.Tg mice (1:1 ratio). Subsequently, mice were followed for the sign of infection and other parameters were measured.

Measurement of viral load

Lung tissues and faecal samples were weighed and homogenized for further processing as described earlier⁶⁰. Briefly, RNA was extracted by using Total RNA Isolation Kit (MDI) as per the manufacturer's protocol. Relative copy number of SARS-CoV-2 RNA was done using previously used formula (POWER (2, $-\Delta$ Ct)*10,000 to calculate the relative gene expression⁶⁰. cDNA was synthesized using the kit from applied biosystem. Copies of SARS-CoV-2 nucleocapsid (N) RNA were determined using the N gene primers (forward: 5'-ATGCTGCAATCGTGCTACAA-3'; reverse: 3'-GACTGCCGCTCTGCTC-5'. β -actin gene was used as an endogenous control for normalization. $\Delta\Delta$ Ct method was used for relative quantitation^{18,61}.

Peripheral blood mononuclear cells (PBMCs) isolation

PBMCs were isolated using density-gradient centrifugation as described previously¹⁸. Briefly, human PBMCs from healthy donors were isolated by Ficoll-paque (GE Healthcare) gradient, and the PBMCs were then washed once with 1X PBS, followed by isolation of total RNA using



Trizol reagent. The RNA isolated from PBMCs was used to test the expression respective genes relative to β -Actin.

Gene expression profiling of human PBMCs

Peripheral blood mononuclear cells (PBMCs) were isolated using density-gradient centrifugation as described previously⁶². Briefly,

blood samples were collected from symptomatic COVID-19 patients (~0–3 days from PCR positive report) and healthy volunteers in heparinized CPTTM (BD Biosciences, USA) tubes and were centrifuged at $1500 \times g$ for 25 min. The PBMC layer was separated and washed with 1X PBS, and total RNA from PBMCs was isolated using the Trizol reagent. The RNA isolated from PBMCs was used to test the expression

Fig. 5 | Foxo1-IL-9 axis is essential for SARS-CoV2 transmission. hACE2.Tg mice (uninfected) were cohoused with Foxo^{fl/fl}.CD4^{Cre} infected (10³PFU) mice, while hACE2-Tg healthy mice were cohoused with hACE2-Tg infected mice. **a** Pictorial diagram represents cohousing of mice (Adopted from “cohousing template” by BioRender.com 2020). **b** Percentage body weight change ($n = 5$; two-way ANOVA: $*p = 0.0215$); bar graph represents as a mean \pm SEM. **c** Gross pathology of Lungs (black arrows show focal red lung lesions). **d, e** Viral burden in the lungs and faeces was analysed by qPCR for viral RNA levels ($n = 4$; two-way ANOVA followed by Tukey's multiple comparison test ($*p < 0.05$, $**p < 0.005$, $***p < 0.0005$, $****p < 0.0001$); bar graph represents as a mean \pm SEM. **f** Haematoxylin-Eosin staining of lung sections; bar graph represents histology score (Hyaline membrane, septal wall thickness, degradation of intracellular septae, infiltration of neutrophils and protein debris); ($\times 40$ magnification; 100 μ m scale bar); $n = 5$ mice per group (two-way ANOVA followed by Tukey's multiple comparison test); $*p < 0.05$, $**p < 0.005$. FACS representative dot plot and its respective bar graph show percentage frequency mean \pm SEM indicating **g** Eosinophils (upper) ($n = 4$), **h** Mast cells (Lower) percentage frequency ($n = 4$); bar graph represents as a mean \pm SEM;

$*p < 0.05$, $**p < 0.0005$, $***p < 0.0001$, ns = non-significant. Further to check the role of IL-9 in Foxo1^{fl/fl} CD4^{Cre} mice we have given exogenously IL-9 to the mice and observed. **i** Percentage body weight change was monitored (one experiment; $n = 5$; two-way ANOVA $*p < 0.0451$; bar graph represents as a mean \pm SEM). **j** Gross lung morphological changes between Foxo^{fl/fl}.CD4^{Cre} infected and rIL-9 treated groups. **k** Viral load quantified by qPCR ($n = 4$); $*p < 0.05$ (students t test); bar graph represents as a mean \pm SEM. **l–n** Representative FACS dot plot and its corresponding bar graph showing mean \pm SEM showing IL-9, IL-4, Mast cells and Eosinophils frequency ($n = 5$ mice per group); one-way ANOVA followed by Tukey's multiple comparison test ($*p < 0.05$, $**p < 0.005$, $***p < 0.0005$). **o, p** Histopathology of lungs from SARS-CoV-2 infected Foxo1^{fl/fl}.CD4^{Cre} mice and rIL-9 treated mice at day 7 post infection. Histopathological observations were done for the H&E stained sections and histological score was given based on Hyaline membrane, septal wall thickness, degradation of intracellular septae, infiltration of neutrophils and protein debris ($\times 60$ magnification; 50 μ m scale bar). $n = 4$; bar graph represents as a mean \pm SEM; $*p < 0.05$ (student t test). Source data are provided as a Source data file.

of respective genes relative to β -Actin by RT-PCR. The relative expression levels ($2^{-\Delta\Delta C_t}$) of genes were further normalized by log2 transformation, and Z-score was calculated as described previously⁶³. The median of Z-scores of log2 transformed relative gene expression was represented as a heat map.

qPCR

RNA was isolated from lungs and spleen as described previously¹⁸. RNA from BAL cell samples was isolated by using RNeasy kit (MDI). Total RNA was subjected to cDNA synthesis using the iScript cDNA synthesis kit (Biorad; #1708891). qPCR was performed as described earlier using SYBR green dye KAPA SYBR FAST qPCR Master Mix (2X) Universal kit on standard 7500 Dx real-time PCR system (Applied Biosystems). The relative gene expression was calculated as described previously¹⁸. Following primer sets were used. Mice Primer sets: *Il-13*–5'-CTTAAG-GAGCTTATTGAGGAG-3' 3'-CATTGCAATTGGAGATGTTG-5'; *cGAS*–5'-GGATAGAGAAAACATGCTGTG-3'; 3'-CAGTTTTCACATGGTAGGAAC-5'; *Tmem173*–5'-CTCATTGTCTACCAAGAACC-3' 3'-TAACCTCCTCCTT TTCTTCC-5'; *Tbk1*–5'-GAACAACCTCAATACCGTAGG-3' 3'-AATTCTT-GATAGAGCAGCAG-5'; *Irf3*–5'-CTTGTAAGAATAACCACCAGC-3' 3'-CTTGTAGAATAACCACCAGC-5'; *Cxcl10*–5'-AAAAAGGTCTAAAAGGGCTC-3' 3'-AATTAGGACTAGCCATCCAC-5'; *Cxcl5*–5'-TCAGAAAATATTGGGCAGTG-3' 3'-CAAAGCAGGGAGTTTCAATAAG-5'; *Oas1g*–5'-CTGTGGTACCCATGTTTTATG-3' 3'-ATACATGTCCAGTTCTCCTC-5'; *Oas2*–5'-TTA-TAAATACCGGACGCTC-3' 3'-ATTACAGGCTCTTTTTCTG-5'; *Oas3*–5'-CCAAACTTAAGAGCCTGATG-3' 3'-GCCTCTCCTCTTTTATATG-5'; *RNaseL*–5'-ATACTGTAGGTGATCTGCTG-3' 3'-AAGTATCTCCTTCATTC CCC-5'; *Irfn1*–5'-AACTTCCAAAACCTGAAGACC-3' 3'-AACTCTGTTTTT CTTTGACC-5'; *Irfn2*–5'-AGCCCAAAGTGAATAATGTC-3' 3'-TGA-TAATCCTGATTCCTGGC-5'; *Irfn1*–5'-CTGAATAAGACCAGCAACTTC-3' 3'-CATGACAGAGAAGAACAAC-5'; *Il-5*–5'-CCCTACTCATAAAAAT CACCAG-3' 3'-TTGGAATAGCATTTCCACAG-5'; *Irfm3*–5'-AAGAATCAA GGAAGAATATGAGG-3' 3'-GATCCCTAGACTTCACGG-5'; *Trim24*–5'-TTCCATCTCTCATGACATC-3' 3'-CATTCTGGCTTGGTGAATATC-5'; β -*Act*–5'-TTAATTTCTGAATGGCCAG-3' 3'-GACCAAGCCTTCATACAT C-5'; *Foxo1*–5'-AAACACATATTAGCCACTG-3' 3'-TCTACTCTGTTT-GAAGGAGG-5'; *Ccl2*–5'-GAAGATGATCCCAATGAGTAG-3' 3'-TTGGTGA CAAAACTACAGC-5'; *Ccl12*–5'-TGTGATCTTCAGGACCATAC-3' 3'-CATGAAGGTTCAAGGATGAAG-5'; *Tph1*–5'-GAACCAACATGCACTT TC-3' 3'-GTTGTAATCTAGTCCAAACG-5'; *Fcer1a*–5'-TCAACTACAGTTA TGAGAGCC-3' 3'-TGGGAAAATTAGTTGTAGCC-5'; *Il-17*–5'-ACGTTTCT CAGCAAACTTAC-3' 3'-CCCTTTACACCTTCTTTTC-5'; *NI*–5'-GACCC-CAAAATCAGCGAAAT-3' 3'-TCTGGTTACTGCCAGTTGAATCTG-5'; *Il-9*–5'-GCATCAGAGACACCAATTAC-3' 3'-GTACAATCATCAGTTGGGAC-5'; *Irfn-γ*–5'-TGAGTATTGCCAAGTTTGAAG-3' 3'-CTTATTGGGACAACTCTT CC-5'; *Irf-4*–5'-GAGTAGGACTACTGGGATG-3' 3'-CTTGCAGCTCTGA

TAGAAAC-5'; *Irf9*–5'-CAACATAGCGGCTGGTGGCAAT-3' 3'-GTTGATG CTCCAGGAACACTGG-5'; *Irf-7*–5'-CCACGCTATACCATCTACCTGG-3' 3'-GCTGCTATCCAGGGAAGACACA-5'; *hACE2*–5'-TCCATTGGTCTTC TGTCACCCG-3' 3'-AGACCATCCACCTCCACTTCTC-5'; *Spil*–5'-GAGG TGTCTGATGGAGAAGCTG-3' 3'-ACCCACCAGATGCTGTCTTCA-5'.

Human primer sets: *Oas2*–5'-GCTTCGACAATCAACAGCCAAAG-3' 3'-CTTGACGATTTGTGCGCTCG-5'; *Il9r*–5'-GACCAAGTTGTCTGTGTT TGGGC-3' 3'-TTTCACCCGACTGAAAATCAGTGG-5'; *Irfn-5* TGGGCTG TGATCTGCCTCAAAC-3' 3'-CAGCCTTTTGGAACTGGTTGCC-5'; *Irf9*–5'-CCACCGAAGTTCAGGTAACAC-3' 3'-AGTCTGCTCCAGCAAGTATCG G-5'; *Oas1*–5'-AGGAAAGGTGCTTCCGAGGTAG-3' 3'-GGACTGAGGAAG ACAACCAGGT-5'; *Oas3*–5'-CCTGATTCGCTGGTGAAGCAC-3' 3'-TCC CAGGCAAAGATGGTGAGGA-5'; *Irfnβ*–5'-CTTGATTCTTACAAAGAAG CAGC-3' 3'-TCCTCCTTCTGGAAGTGTGCA-5'; *Trim22*–5'-GGATCGTC AGTAGAGATGCTGC-3' 3'-GAATCTGCAGCATCCCACTCAG-5'; *Irfm*–5'-GCGTTCTATGACATTCGCTACTC-3' 3'-AGATGTTCTAGGCATCTGGCGG T-5'; *RNaseL*–5'-AAGGCTGTTCAAGAACTACATCTTG-3' 3'-TGGATCTC CAGCCCACTGATG-5'; *Il9*–5'-GACATCAACTTCTCATC-3' 3'-GAGAC AACTGGTCTTCTGG-3'; *Irf3*–5'-TCTGCCCTCAACCGCAAAGAAG-3' 3'-TACTGCCTCCACCATTTGGTGTG-5'; *Irf7*–5'-CCACGCTATACCATCTAC CTGG-3' 3'-GCTGCTATCCAGGGAAGACACA-5'; *Il9r*–5'-ATCAGTCTT GCCTTGGAGCCAA-3' 3'-CCGACAATGTGATCCCTGTGCT-5'; *Irfn-α*–5'-T GGGCTGTGATCTGCCTCAAAC-3' 3'-CAGCCTTTTGGAACTGGTTGC C-5'; *Irfn-β*–5'-CTTGATTCTTACAAAGAAGCAGC-3' 3'-TCCTCCTTCTG GAATCTGTCGA-5'; Hamster primer sets: Foxo15'-AGGATAAGGCGCA-GACGAAC-3' 3'-GTCCCGGCTCTTAGCAAAAT-5'; *Il-9*–5'-CTCTGCCCTG CTCTTTGGTT-3' 3'-CGAGGGTGGGTCTTCTTCA-5'; *Pu.1*–5'-GCATTG GAGGTGTCTGAT-3' 3'-CATCTTCTGCGGTTGCCCT-5'.

BALF collection and lung histological analysis

Lung lavage was collected by inserting a cannula into the trachea and lavaging with 500 μ l cold PBS three times as previously described¹². Lavage sample was centrifuged, and supernatant was collected for further cytokine analysis, and cells were used for FACS analysis. Lungs were excised; left lower lobe was immersed in 10% formalin and used for histological analysis. Paraffin-embedded tissue samples were further sectioned and various histological stainings (H&E, Periodic acid Schiff's, van Gieson, and toluidine blue) were performed at ILBS (New Delhi) and the scoring was done by a trained histopathologist independently in a blinded manner.

Lung Injury Scoring System given by the three random people, in order to help quantitate histological features of ALI (Acute Lung Injury). In a blinded manner, three random diseased fields of lung tissue were chosen at high power (60 \times), which were scored for the following: (A) Immune cell infiltration (none=0, 1–5 cells=1, >5 cells=2), (B) Damage in the interstitial space/septae, (C) Proteinaceous

debris in air spaces (none = 0, one instance = 1, >1 instance = 2), (D) alveolar septal thickening (<2× mock thickness = 0, 2–4× mock thickness = 1, >4× mock thickness = 2).

Immunohistochemistry

For immunohistochemistry 2–4-µm sections were used as described earlier¹². Briefly, paraffin-embedded sections were dewaxed and rehydrated through xylene and graded alcohol, respectively, for 15 min at room temperature (RT), before epitope unmasking, slides were blocked with normal goat serum for 30 min in RT. Samples were then incubated with a primary antibody incubated overnight at 4 °C (SARS-CoV-2-N antigen (5–25 µg/ml; R&D, # Clone # 1035145)). Species-matched gamma globulin was used as an isotype control at the same concentration. Sections were washed in PBST and Species-matched secondary antibodies were applied for 60 min at RT. The finally stained sections for SARS-CoV-2-N protein were then observed and images were captured under Ti Eclipse Nikon microscope at RCB (Regional Centre for Biotechnology).

Cytokine ELISA

Quantitation of IL-4, IL-9, IL-10 and IFN-γ was measured in BALF ELISA as described earlier¹². Briefly, ELISA plates were coated overnight by anti-IL-4, anti-IL-9, anti-IL10 or anti-IFNγ antibodies overnight in bicarbonate buffer. Thereafter, wells were washed and blocked and then incubated with BAL fluid at 1:1 dilution. The wells were then washed and incubated with detection antibody conjugated with biotin. Colour was developed by incubating with Avidin-HRP enzyme and then with TMB substrate. Reaction was stopped by using 0.2 N stop solution and plate was read at 600 nm in spectrophotometer (BioLinkk).

Flow cytometry analysis

FACS analysis of BAL cells, Splenocytes, and dLN's were carried out using fluorochrome labelled antibodies. Cells were collected from the lungs after washing them with the cold PBS. Cells were activated with PMA (phorbol 12-myristate13-acetate; 50 ng ml⁻¹; Sigma-Aldrich) and Ionomycin (1.0 µg ml⁻¹; Sigma-Aldrich) in the presence of Monensin (#554724 Golgi Stop, BD Biosciences) followed by surface markers and intracellular cytokines staining. The following antibodies were used: anti-mouse CD3 BV510 (#100353, Clone-145-2C11, Biolegend INC, USA, 1:1000), anti-mouse γδTCR FITC (#118105, Clone-GL3, Biolegend INC, USA, 1:1000), anti-mouse Gr1 BV421 (#108445, Clone-RB6-8C5, Biolegend INC, USA, 1:1000), anti-mouse CD11b PerCp-Cy5.5 (#101228, Biolegend INC, USA, 1:1000), anti-mouse CD4-PerCp cy5.5 (#100538; Clone-RM4-5, Biolegend INC, USA, 1:1000), anti-mouse CD4-FITC (#100406; Clone-GK1.5, Biolegend, INC, USA, 1:1000), anti-mouse NK1.1-PE-Cy7 (#108714; Biolegend, USA, 1:1000), anti-mouse-CD8 – BV421 (#100753; Clone-53-6.7 Biolegend INC, USA, 2:2000), F4/80 – FITC (#123108; Clone-BM8, Biolegend INC, USA, 1:1000), CD206 – PE (#141705; Clone-C068C2, Biolegend, USA, 2:1000), CD80 – AF647 (#305216, Clone-2D10, Biolegend INC, USA, 1:1000), CD68 – PEcy7 (#137015; Clone-FA-11, Biolegend INC, USA, 1:1000), CD49b (#117322; Clone-N418, Biolegend INC, USA, 1:1000), C-kit (#105805; Clone-2B8, Biolegend INC, USA, 2:100), Fcεr1 (#134308; Clone-MAR1, Biolegend INC, USA, 2:100), Siglec-f (#155528; Clone-S17007L, Biolegend INC, USA, 2:100), IFNγ – AF647 (#505814; Clone-XMG1.2, Biolegend INC, USA, 1:100), IL-17 – PE-cy7 (#506922; Clone-TC11-18H10.1, Biolegend INC, USA, 1:100), IL-10 – PE (#505008; Clone-JES5-16E3, Biolegend INC, USA, 5:1000), Foxp3 – AF647 (#126408; Clone-MF14, Biolegend, USA, 2:500), IL-9 – PerCp-cy5.5 (#514112, Clone-RM9A4, Biolegend INC, USA, 5:1000), IL-4 – PE (#504104, Clone-11B11, Biolegend, USA, 2:500) IL-4 – PE-Cy7 (#504118, Clone-11B11, Biolegend, USA, 1:200).

NK, ILCs analysis of BALF cells were carried out using fluorochrome labelled antibodies. Cells were activated as mentioned above followed by surface markers and intracellular cytokines staining. The following antibodies were used: Lineage cocktail antibodies

{anti-mouse CD3 FITC (# 100204, Clone-17A2, Biolegend INC, USA, 2:2000), anti-mouse CD11b FITC (#101206, Clone-M1/70, Biolegend INC, USA, 1:1000), F4/80 – FITC (#123108; Clone-BM8, Biolegend INC, USA, 1:1000), anti-mouse B220- FITC (#103206; Clone-RA3-6B2, Biolegend INC, USA, 2:2000), anti-mouse CD4-PerCp cy5.5 (#100538; Clone-RM4-5, Biolegend INC, USA, 1:1000), anti-mouse NK1.1-PE-Cy7 (#108714; Clone-PK136, Biolegend INC, USA, 1:1000), IL-9 – APC (#514106; Clone-RM9A4, Biolegend, USA, 3:3000). Stained cells were acquired on FACS-Canto-II (Becton Dickinson, San Jose, CA) and analysed using Flowjo software (Tree Star, Ashland, OR, USA).

For sorting of mTmG CD4⁺, Foxo^{fl/fl}.CD4^{Cre+} CD4⁺ T cells, we sacrificed the ROSA mTmG wt mice and Foxo^{fl/fl}.CD4^{Cre+} mice euthanized; spleen and lymph nodes were collected aseptically and single-cell suspensions were made from 6–8-week-old mice. CD4⁺ T cells were purified using anti-mouse CD4-PerCp cy5.5 (#100538; Biolegend). CD4⁺ T cells were further sorted using fluorescence-activated cell sorting (FACS) on BD FACS Aria III (BD Biosciences) to obtain PE⁺ CD4⁺ T cells and CD4⁺ T cells using anti-CD4-PerCp Cy5.5. The purity of sorted cells was typically ~96% in post-sort analysis.

hACE2 expressing Intestinal epithelial cells isolation (IECs)

Primary IECs were isolated as described earlier⁶⁴. Briefly, the intestine from the ACE2.Tg mice was cleaned with the cold PBS containing Gentamycin. The intestine was cut longitudinally and mucus layer was removed and placed in EDTA (30 mM) solution at 4 °C for 20 min. Colon epithelial cells were gently removed and washed with PBS. Subsequently, the collected cells were plated in collagen-coated plates.

Western blot

We treated the hACE2.Tg mice with or without rIL-9 (500 ng/mice; i.n.). After 24 h, we sacrificed the mice using an overdose of Ketamine and Xylazine. Cardiac perfusion was performed, and further, we digested the lungs with Dispase to get the single-cell suspension. We collected the cells and lysed them in RIPA buffer containing PIC (Protease inhibitor cocktail). In line with this, we treated the Caco2 cells (Human epithelial cell line) with or without rIL-9 (10 ng/ml) for 24 h. We have lysed the cells in RIPA buffer, as mentioned above. The protein concentration was determined by performing a BCA protein assay (Bio-Rad). 40 µg of protein extracts were loaded on a 10% SDS-Gel for hACE2. Proteins were transferred to a membrane, blocked with 5% BSA, and then incubated in primary antibody (MA5-31395; Thermo-Scientific) overnight at 4 °C. The HRP-conjugated anti-mouse (#7076; CST) secondary antibody was incubated for 1 h. Bands were captured on Gel-doc (BIO-RAD). Band intensities were normalised with β-Actin (#4967; CST) and calculated by using ImageJ software.

Transcriptome profiling using RNA quantification sequencing

RNA sequencing of SARS-CoV-2 infected lungs of ACE2.Tg, hACE2.Tg, Foxo^{fl/fl}.CD4^{Cre+}, and Foxo^{fl/fl}.CD4^{Cre+} SARS-CoV-2 infected lung tissues were homogenised and RNA was derived and subjected to next-generation sequencing (NGS) to generate deep coverage RNASeq data. Size selection of RNA fragments was done with SPRI Beads-based Size Selection. High-quality libraries were prepared using NEB Next Ultra II Directional RNA Library Prep Kit according to manufacturer's protocols and paired-end reads of 151 bp read length were generated on the Illumina Novoseq 6000 platform.

Transcriptome analysis

Quality-based filtering and adaptor trimming of the raw sequencing reads was done using fastp (v0.20.1). A threshold of 30 was set for the phred quality score. The filtered reads were aligned against the Mus musculus (mm39) genome using the splice aware aligner Hisat (v2.2.1).

The alignments were assembled into transcripts with stringtie assembler (v2.1.5). Stringtie computes read counts for the genes and

normalized expression values with the Transcript per million (TPM) metric. The gene read counts were used for differential analysis between the conditions. Genes having a p -value of less than 0.05 were considered to have a significant differential change in the expression between the conditions. A log2Foldchange of 2 and higher of these significant genes were classified as upregulated and a log2Foldchange of -2 and lower as downregulated. Genes were functionally annotated with Gene Ontology terms and Reactome pathways using NCBI resources. David Bioinformatics resources (v6.8) was used to identify significant enrichment of significant GO terms and pathways. String database was used to determine for interaction of the protein-coding genes. A high confidence score of 0.9 was used to compute the interactions. R packages used for visualization – Complex Heat map, Enhanced Volcano, ggplot2.

Principal component analysis

High-dimensional expression data are mathematically reduced to principle components that can be used to describe variation across samples in fewer dimensions to allow human interpretation. Principle component 1 (PC1) accounts for the most amount of variation across samples, PC2 the second most, and so on. These PC1 vs PC2 plots are coloured by sample annotation to demonstrate how samples cluster together (or not) in reduced dimensional space. PCA emphasizes variation and brings out strong patterns in a dataset. It's used to make data simpler to explore and visualize.

Viral RNA isolation and qRT-PCR

Viral RNA from stock solutions was isolated using Trizol, and SARS-CoV-2 detection and quantification were performed using a SARS-CoV-2 kit (Illumina, Cat. No. 20044311) with a cycle threshold of 35.

Library preparation, sequencing

Whole genome sequencing of the SARS-CoV-2 and B.1.1.529 samples, using the capture-based Illumina Respiratory Virus Oligo Panel (RVOP), was done to capture the SARS-CoV-2 genome. The library preparation protocols for RVOP have been previously described. Briefly, double-stranded cDNA was prepared from 300 ng RNA using the COVID Seq kit (Cat. No. 20051772). The RVOP library was prepared using Illumina DNA Prep (Illumina, Cat. No. 20044311). Agilent 2100 bioanalyzer was used to check the quality of both libraries. The RVOP library was denatured and diluted to optimal loading concentration for sequencing on the MiSeq platform using a v3 reagent kit at 2×75 bp read length. The sequencing data analysis was performed as previously described^{65–67}. The sequencing data analysis was performed as previously described^{65–67}.

Minor variant analysis

The primer-free pair raw reads of SARSCoV2 were generated from the Illumina MiSeq. Raw reads of SARSCoV2 were pre-processed based on read quality and read length (phred quality ≥ 30 and minimum length ≥ 50 base pair) and merged by PEAR programme⁶⁸. The merged reads were mapped to Wuhan's SARSCoV2 sequence (Genebank ID: NC_045512.2) to generate a consensus genome⁶⁹. During the mapping of reads to reference genome sequence, a BAM file was generated by Samtools⁷⁰. This BAM file was processed by diversitools script in DiversiTools (<http://josephhughes.github.io/btctools/>) to find the frequency of all types of four bases for each position of a reference sequence. The only variants that have been covered by at least 15 times (read depth ≥ 15) by high-quality reads (average read's phred score ≥ 30) to find highly accurate single nucleotide variants (SNVs)⁷¹.

Statistical analysis

All the results were analysed and plotted using GraphPad Prism 8.0 software. Percentage change weight, relative gene expression, lung haemorrhagic scores, FACS, ELISA, and qPCR studies were compared and plotted as mean using graph pad. Dataset was analysed by using

one-way ANOVA, two-way ANOVA, Wilcoxon test or Student's t -test. Differences were considered statistically significant with a p value of less than or equal to 0.05.

Statistics and reproducibility

No statistical method was used to predetermine sample size. No data were excluded from the analyses. Mice of different genotypes were randomly assigned to treatment groups throughout the study. For experiments involving genetically modified animals, littermates were used for each experiment. In the cell and animal experiments, investigators were not blinded to group allocation because the investigators should give the drug to the mice and cell in different treatment conditions. Bio render software was used for pictorial representations.

Reporting summary

Further information on research design is available in the Nature Portfolio Reporting Summary linked to this article.

Data availability

The RNA sequence Data generated in this study has been deposited in the NCBI SRA database under the accession code no. PRJNA842504. Publicly available data with accession code, [GSE209550](https://www.ncbi.nlm.nih.gov/geo/query/acc.cgi?acc=GSE209550). The authors declare that, the necessary data required to validate the findings of the paper can be found within the article itself or in the Supplementary Materials. Source data are provided with this paper.

References

- Nalbandian, A. et al. Post-acute COVID-19 syndrome. *Nat. Med.* **27**, 601–615 (2021).
- Merad, M. & Martin, J. C. Pathological inflammation in patients with COVID-19: a key role for monocytes and macrophages. *Nat. Rev. Immunol.* **20**, 355–362 (2020).
- RECOVERY Collaborative Group et al. Dexamethasone in hospitalized patients with Covid-19. *N. Engl. J. Med.* **384**, 693–704 (2021).
- Rizvi, Z. et al. SARS-CoV-2 and its Variants, But Not Omicron, Induces Severe Thymic Atrophy and Impaired T Cell Development (2022).
- Gebremeskel, S. et al. Mast cell and eosinophil activation are associated with COVID-19 and TLR-mediated viral inflammation: implications for an anti-Siglec-8 antibody. *Front. Immunol.* **12**, 650331 (2021).
- Conti, P. et al. Mast cells activated by SARS-CoV-2 release histamine which increases IL-1 levels causing cytokine storm and inflammatory reaction in COVID-19. *J. Biol. Regul. Homeost. Agents* **34**, 1629–1632 (2020).
- Liao, M. et al. Single-cell landscape of bronchoalveolar immune cells in patients with COVID-19. *Nat. Med.* **26**, 842–844 (2020).
- Tan, J. et al. Signatures of mast cell activation are associated with severe COVID-19. Preprint at medRxiv <https://doi.org/10.1101/2021.05.31.21255594> (2021).
- Chang, H.-C. et al. The transcription factor PU.1 is required for the development of IL-9-producing T cells and allergic inflammation. *Nat. Immunol.* **11**, 527–534 (2010).
- Goswami, R. et al. STAT6-dependent regulation of Th9 development. *J. Immunol.* **188**, 968 (2012).
- George, L. & Brightling, C. E. Eosinophilic airway inflammation: role in asthma and chronic obstructive pulmonary disease. *Ther. Adv. Chronic Dis.* **7**, 34–51 (2016).
- Temann, U. A. et al. Expression of interleukin 9 in the lungs of transgenic mice causes airway inflammation, mast cell hyperplasia, and bronchial hyperresponsiveness. *J. Exp. Med.* **188**, 1307–1320 (1998).
- Végran, F. et al. The transcription factor IRF1 dictates the IL-21-dependent anticancer functions of TH9 cells. *Nat. Immunol.* **15**, 758–766 (2014).

14. Staudt, V. et al. Interferon-regulatory factor 4 is essential for the developmental program of T helper 9 cells. *Immunity* **33**, 192–202 (2010).
15. Jabeen, R. et al. Th9 cell development requires a BATF-regulated transcriptional network. *J. Clin. Investig.* **123**, 4641–4653 (2013).
16. Wang, Y. et al. Histone Deacetylase SIRT1 Negatively Regulates the Differentiation of Interleukin-9-Producing CD4⁺ T Cells. *Immunity* **44**, 1337–1349 (2016).
17. Roy, S. et al. EGFR-HIF1 α signaling positively regulates the differentiation of IL-9 producing T helper cells. *Nat. Commun.* **12**, 3182 (2021).
18. Malik, S. et al. Transcription factor Foxo1 is essential for IL-9 induction in T helper cells. *Nat. Commun.* **8**, 815 (2017).
19. Ouyang, W. et al. An essential role of the Forkhead-box transcription factor Foxo1 in control of T cell homeostasis and tolerance. *Immunity* **30**, 358–371 (2009).
20. Lainé, A. et al. Foxo1 is a T cell-intrinsic inhibitor of the ROR γ t-Th17 program. *J. Immunol.* **195**, 1791–1803 (2015).
21. Wu, C. et al. Induction of pathogenic TH17 cells by inducible salt-sensing kinase SGK1. *Nature* **496**, 513–517 (2013).
22. Dalal, R., Sadhu, S. & Awasthi, A. in *Translational Autoimmunity* (ed. Rezaei, N.) 93–121 (Academic Press, 2022).
23. Ouyang, W. et al. Novel Foxo1-dependent transcriptional programs control Treg cell function. *Nature* **491**, 554–559 (2012).
24. Bao, L. et al. The pathogenicity of SARS-CoV-2 in hACE2 transgenic mice. *Nature* **583**, 830–833 (2020).
25. Winkler, E. S. et al. SARS-CoV-2 infection of human ACE2-transgenic mice causes severe lung inflammation and impaired function. *Nat. Immunol.* **21**, 1327–1335 (2020).
26. Malik, S. & Awasthi, A. Transcriptional control of Th9 cells: role of Foxo1 in interleukin-9 induction. *Front Immunol.* **9**, 995 (2018).
27. Halfmann, P. J. et al. SARS-CoV-2 Omicron virus causes attenuated disease in mice and hamsters. *Nature* **603**, 687–692 (2022).
28. Diamond, M. S. & Kanneganti, T.-D. Innate immunity: the first line of defense against SARS-CoV-2. *Nat. Immunol.* **23**, 165–176 (2022).
29. Schneider, W. M., Chevillotte, M. D. & Rice, C. M. Interferon-stimulated genes: a complex web of host defenses. *Annu. Rev. Immunol.* **32**, 513–545 (2014).
30. Mossel, E. C. et al. Exogenous ACE2 expression allows refractory cell lines to support severe acute respiratory syndrome coronavirus replication. *J. Virol.* **79**, 3846–3850 (2005).
31. Sherman, E. J. & Emmer, B. T. ACE2 protein expression within isogenic cell lines is heterogeneous and associated with distinct transcriptomes. *Sci. Rep.* **11**, 15900 (2021).
32. Van den Broeke, C. et al. An emerging role for p21-activated kinases (Paks) in viral infections. *Trends Cell Biol.* **20**, 160–169 (2010).
33. Yoo, J.-S. et al. SARS-CoV-2 inhibits induction of the MHC class I pathway by targeting the STAT1-IRF1-NLRC5 axis. *Nat. Commun.* **12**, 6602 (2021).
34. Li, M. et al. Pharmacological activation of STING blocks SARS-CoV-2 infection. *Sci. Immunol.* **6**, eabi9007 (2021).
35. Nolin, J. D. et al. Identification of epithelial phospholipase A(2) receptor 1 as a potential target in asthma. *Am. J. Respir. Cell Mol. Biol.* **55**, 825–836 (2016).
36. Alba, G. A. et al. Pulmonary endothelial NEDD9 and the pro-thrombotic pathophenotype of acute respiratory distress syndrome due to SARS-CoV-2 infection. *Pulm. Circ.* **12**, e12071 (2022).
37. Maghsoudloo, M. et al. Identification of biomarkers in common chronic lung diseases by co-expression networks and drug-target interactions analysis. *Mol. Med.* **26**, 9 (2020).
38. Rogers, A. J. et al. Copy number variation prevalence in known asthma genes and their impact on asthma susceptibility. *Clin. Exp. Allergy* **43**, 455–462 (2013).
39. Zhang, L. et al. NLRC3, a member of the NLR family of proteins, is a negative regulator of innate immune signaling induced by the DNA sensor STING. *Immunity* **40**, 329–341 (2014).
40. Li, M. M. et al. Interferon regulatory factor 2 protects mice from lethal viral neuroinvasion. *J. Exp. Med.* **213**, 2931–2947 (2016).
41. Shan, Q. et al. The transcription factor Runx3 guards cytotoxic CD8⁺ effector T cells against deviation towards follicular helper T cell lineage. *Nat. Immunol.* **18**, 931–939 (2017).
42. Wilhelm, C. et al. An IL-9 fate reporter demonstrates the induction of an innate IL-9 response in lung inflammation. *Nat. Immunol.* **12**, 1071–1077 (2011).
43. Israelow, B. et al. Adaptive immune determinants of viral clearance and protection in mouse models of SARS-CoV-2. *Sci. Immunol.* **6**, eabl4509 (2021).
44. McNamara, P. S. et al. Interleukin 9 production in the lungs of infants with severe respiratory syncytial virus bronchiolitis. *Lancet* **363**, 1031–1037 (2004).
45. Dodd, J. S. et al. IL-9 regulates pathology during primary and memory responses to respiratory syncytial virus infection. *J. Immunol.* **183**, 7006–7013 (2009).
46. Zhou, Y., McLane, M. & Levitt, R. C. Th2 cytokines and asthma — Interleukin-9 as a therapeutic target for asthma. *Respir. Res.* **2**, 80 (2001).
47. Sugimoto, N. et al. IL-9 blockade suppresses silica-induced lung inflammation and fibrosis in mice. *Am. J. Respir. Cell Mol. Biol.* **60**, 232–243 (2019).
48. Cheng, G. et al. Anti-interleukin-9 antibody treatment inhibits airway inflammation and hyperreactivity in mouse asthma model. *Am. J. Respir. Crit. Care Med.* **166**, 409–416 (2002).
49. Hültner, L. et al. Mast cell growth-enhancing activity (MEA) is structurally related and functionally identical to the novel mouse T cell growth factor P40/TCGFII (interleukin 9). *Eur. J. Immunol.* **20**, 1413–1416 (1990).
50. Townsend, M. J. et al. IL-9-deficient mice establish fundamental roles for IL-9 in pulmonary mastocytosis and goblet cell hyperplasia but not T cell development. *Immunity* **13**, 573–583 (2000).
51. Peacock, T. P. et al. The furin cleavage site in the SARS-CoV-2 spike protein is required for transmission in ferrets. *Nat. Microbiol.* **6**, 899–909 (2021).
52. Li, W. Delving deep into the structural aspects of a furin cleavage site inserted into the spike protein of SARS-CoV-2: a structural biophysical perspective. *Biophys. Chem.* **264**, 106420 (2020).
53. Khatri, R. et al. Intrinsic D614G and P681R/H mutations in SARS-CoV-2 VoCs Alpha, Delta, Omicron and viruses with D614G plus key signature mutations in spike protein alters fusogenicity and infectivity. *Med. Microbiol. Immunol.* **212**, 1–20 (2022).
54. Saito, A. et al. Enhanced fusogenicity and pathogenicity of SARS-CoV-2 Delta P681R mutation. *Nature* **602**, 300–306 (2022).
55. Steinhauer, D. A. Role of hemagglutinin cleavage for the pathogenicity of influenza virus. *Virology* **258**, 1–20 (1999).
56. Whittaker, G. R. SARS-CoV-2 spike and its adaptable furin cleavage site. *Lancet Microbe* **2**, e488–e489 (2021).
57. Goswami, R. & Kaplan, M. H. A brief history of IL-9. *J. Immunol.* **186**, 3283–3288 (2011).
58. Wang, W. B., Levy, D. E. & Lee, C. K. STAT3 negatively regulates type I IFN-mediated antiviral response. *J. Immunol.* **187**, 2578–2585 (2011).
59. Lei, C. Q. et al. FoxO1 negatively regulates cellular antiviral response by promoting degradation of IRF3. *J. Biol. Chem.* **288**, 12596–12604 (2013).
60. Rizvi, Z. A. et al. Golden Syrian hamster as a model to study cardiovascular complications associated with SARS-CoV-2 infection. *Elife* **11**, e73522 (2022).

61. Sadhu, S. et al. Gefitinib results in robust host-directed immunity against salmonella infection through proteo-metabolomic reprogramming. *Front. Immunol.* **12**, 648710 (2021).
62. Thiruvengadam, R. et al. Effectiveness of ChAdOx1 nCoV-19 vaccine against SARS-CoV-2 infection during the delta (B.1.617.2) variant surge in India: a test-negative, case-control study and a mechanistic study of post-vaccination immune responses. *Lancet Infect. Dis.* **22**, 473–482 (2022).
63. Cheadle, C. et al. Analysis of microarray data using Z score transformation. *J. Mol. Diagnostics* **5**, 73–81 (2003).
64. Mustafa, S. A. et al. SUMOylation pathway alteration coupled with downregulation of SUMO E2 enzyme at mucosal epithelium modulates inflammation in inflammatory bowel disease. *Open Biol.* **7**, 170024 (2017).
65. Mehta, P. et al. Respiratory co-infections: modulators of SARS-CoV-2 patients' clinical sub-phenotype. *Front. Microbiol.* **12**, 653399 (2021).
66. Li, H. & Durbin, R. Fast and accurate short read alignment with Burrows-Wheeler transform. *Bioinformatics* **25**, 1754–1760 (2009).
67. Danecek, P. et al. Twelve years of SAMtools and BCFtools. *Giga-science* **10**, giab008 (2021).
68. Zhang, J. et al. PEAR: a fast and accurate Illumina Paired-End read mergeR. *Bioinformatics* **30**, 614–620 (2014).
69. Poojary, M. et al. *Computational Protocol for Assembly and Analysis of SARS-nCoV-2 Genomes* 1–14 (2020).
70. Li, H. et al. The sequence alignment/Map format and SAMtools. *Bioinformatics* **25**, 2078–2079 (2009).
71. Song, K., Li, L. & Zhang, G. Coverage recommendation for genotyping analysis of highly heterologous species using next-generation sequencing technology. *Sci. Rep.* **6**, 35736 (2016).

Acknowledgements

Funding support was provided to the AA laboratory from THSTI core grant, Translational Research Programme (TRP). We thank Dr. Bhabatosh Das, Dr. Pradipta, Dr. Shikha Saxena and Dr. Sweetly Samal for helping with the sequencing and analysis of SARS-CoV-2 and B.1.1.529 in Next Generation Sequencing Lab at THSTI (New Delhi). We thank Dr. Sweetly Samal, and Ritika Khatri for providing the virus. We thank FACS facility Incharge, Dr. Deepak Rathore for providing support. We acknowledge SAF and infectious disease research facility (IDRF) for its support. ILBS bio bank: for support in histological analysis and assessment. RCB microscopy facility: for microscopic examination of the histology slide. The following reagent was deposited by the Centers for Disease Control and Prevention and obtained through BEI Resources, NIAID, NIH: SARS Related Coronavirus 2, Isolate USA-WA1/2020, NR-52281, Isolate hCoV-19/USA/MD-HP20874/2021 (Lineage B.1.1.529, Omicron Variant), NR-56461, contributed by Andrew S. Pekosz, We acknowledge the BIRAC

funding (BT/CS0054/21 and BT/CTH/0004/21) and the intramural funding from THSTI to support this study.

Author contributions

Conceived, designed and supervised the study: A.A.; designed and performed the experiments: S.S.; ABSL3 experiment: S.S., R.D., J.D. and Z.A.R.; FACS: S.S., R.D. and V.D.; qPCR: S.S., R.D. and A.B.; ELISA: Z.A.R.; bright field microscopy imaging: S.S. and V.S.; genotyping: M.R.T. and S.G.; minor variant analysis: S.K.; analysed the Data: S.S.; contributed reagents/materials/analysis tools: A.A.; wrote the manuscript: S.S. and A.A.

Competing interests

The authors declare no competing interests.

Additional information

Supplementary information The online version contains supplementary material available at <https://doi.org/10.1038/s41467-023-39815-5>.

Correspondence and requests for materials should be addressed to Amit Awasthi.

Peer review information *Nature Communications* thanks Tobias Bopp and the other, anonymous, reviewer(s) for their contribution to the peer review of this work. Peer reviewer reports are available.

Reprints and permissions information is available at <http://www.nature.com/reprints>

Publisher's note Springer Nature remains neutral with regard to jurisdictional claims in published maps and institutional affiliations.

Open Access This article is licensed under a Creative Commons Attribution 4.0 International License, which permits use, sharing, adaptation, distribution and reproduction in any medium or format, as long as you give appropriate credit to the original author(s) and the source, provide a link to the Creative Commons license, and indicate if changes were made. The images or other third party material in this article are included in the article's Creative Commons license, unless indicated otherwise in a credit line to the material. If material is not included in the article's Creative Commons license and your intended use is not permitted by statutory regulation or exceeds the permitted use, you will need to obtain permission directly from the copyright holder. To view a copy of this license, visit <http://creativecommons.org/licenses/by/4.0/>.

© The Author(s) 2023